

## ABSTRACT

Title of Document: EXTREME VERTICAL DISPLACEMENT,  
HIGH FORCE, SILICON MICROSTAGE  
ZIPPER ACTUATORS

Jason D. Felder, Master of Science, 2013

Directed By: Dr. Don L. DeVoe, Department of Mechanical  
Engineering

Large vertical deflection, high force microactuators are desired in MEMS for a variety of applications. This thesis details a novel large-displacement electrostatic “zipper” microactuator capable of achieving hundreds of microns of out-of-plane deflection and delivering high forces, fabricated entirely from SOI (silicon-on-insulator). This technology is novel in its use of SiO<sub>2</sub> as both a high quality dielectric and the stressed layer of the bimorph. Geometries are explored analytically, numerically and experimentally to provide the greatest electromechanical output while constraining the device footprint to 1mm<sup>2</sup>. Device performance was benchmarked against previously established out-of-plane microactuators. We report the first instance of zipper-inspired electrostatic “microstage” actuators whose flat center stage and vertical actuation mode is ideal for carrying and moving a load. Fabricated microstages are capable of achieving out-of-plane deflections up to 1.2 mm, force outputs up to 1 mN, pull-in voltage as low as 20 V, and switching times of 1 ms.

EXTREME VERTICAL DISPLACEMENT, HIGH FORCE, SILICON  
MICROSTAGE ZIPPER ACTUATORS

By

Jason D. Felder

Thesis submitted to the Faculty of the Graduate School of the  
University of Maryland, College Park, in partial fulfillment  
of the requirements for the degree of  
Master of Science  
2013

Advisory Committee:  
Professor Don L. DeVoe, Chair  
Professor Sarah Bergbreiter  
Professor Santiago Solares

© Copyright by  
Jason D. Felder  
2013

## Dedication

This work is dedicated to Mom, Dad, Zach, Jeremy, Alissa and Jen, whose tireless support, encouragement and guidance has made this work a success, and to Leah, for her constant reminders that wafers come in many varieties (chocolate, vanilla, etc.)

other than silicon.

I love you all very much.

## Acknowledgements

The entirety of this work would not have been possible without the collective support of many special individuals and groups, whose guidance, criticism, optimism and expertise were instrumental in my achievement. You have lent me your time, energy and immense knowledge, and for that I owe tremendous thanks to you all:

To Prakruthi, who took me under her wing when I knew less than nothing of MEMS and microactuators, and taught me how to spread my own wings.

To the members of Maryland MEMS and Microfluidics Laboratory (MML), my labmates, for smiling and commiserating together, for sharing knowledge, ideas and milestones, and for your forgiveness for always “forgetting” weekly lab cleaning.

To the staff at University of Maryland’s FabLAB – Jon, John and Tom. Your individual senses of humor and century of collective knowledge always ensured that working in the FabLAB was a productive and enjoyable experience.

To Syntonics LLC, for granting me (and funding) this opportunity. To Steve, for being a great boss, always encouraging me and pushing me to think outside the box. To everyone at Syntonics, Ohio State University – Eugene, Eric, and others – for gallantly enduring my weekly teleconference research updates, and for your continued advice and suggestions.

To my parents, friends and family, for demonstrating how responsible adults can balance work and play, and for teaching me not to lose sight of what life is all about. For listening to me rave and rant about the ups and downs of research, and for nodding your head in understanding even though I know that the most you can tell friends about my research is that it involves “tiny robots”. You are the most important people in my life, and your support throughout this project has meant more to me than you know.

To Leah, for accepting with grace the late night lab sessions, the great distance between Maryland and Manhattan, and my waxing poetic about MEMS and science in general.

To Dr. DeVoe for epitomizing a mentor and adviser: guiding this project just enough for it to succeed without taking control. I have learned more about myself, my skills and abilities, mental toughness and fortitude in working on this project than I have in any other endeavor to date. As a model of academic integrity, determination, and intellectual passion, you have prepared me for a life-long career in the sciences.

# Table of Contents

Dedication .....	ii
Acknowledgements .....	iii
Table of Contents .....	iv
List of Tables .....	vi
List of Figures .....	vii
List of Abbreviations .....	x
Nomenclature .....	x
Chapter 1: Introduction.....	1
1.1. Background.....	1
1.1.1. Out-of-Plane Large Deflection Microactuators: An Overview .....	3
1.1.2. Out-of-Plane Large Deflection Electrostatic Zipper Actuators .....	9
1.2. Thesis Goal and Scope.....	11
1.3. Organization.....	13
Chapter 2: Electrostatic Zipper Actuators: Cantilever Beams.....	16
2.1. Introduction.....	16
2.2. Theory and Modeling.....	16
2.2.1. Analytic Model – MATLAB .....	16
2.2.2. Numeric Model – COMSOL .....	25
2.3. Fabrication of Cantilever Zipper Actuators .....	27
2.4. Results and Characterization of Cantilever Zipper Actuators .....	31
2.4.1. Deflection Characterization .....	31
2.4.2. Voltage Characterization .....	33
2.5. Design Capabilities of Cantilever Zipper Actuators.....	34
2.5.1. Benchmarking .....	36
2.6. Summary .....	40
Chapter 3: Electrostatic Zipper Actuators: Microstage Actuators.....	42
3.1. Introduction.....	42
3.1.1. Spiral Design – Geometric Challenge: “Birds Nest Phenomenon” ....	43
3.1.2. Solution to the “Birds Nest” – Microstage Actuators.....	44
3.2. Theory and Modeling.....	46
3.2.1. Analytic Model – MATLAB .....	47
3.2.2. Numeric Model – COMSOL .....	50
3.3. Fabrication of Microstage Zipper Actuators.....	52
3.3.1. Microstage Actuator Fabrication .....	52
3.3.2. Other Topologies Enabled Through Selective Oxide Patterning.....	55
3.3.3. Electrode Fabrication .....	57
3.3.4. Packaging and Bonding of Microstage Actuator to Electrode.....	62
3.3.5. Integrated Circuit Board and Die Packages for Testing .....	62
3.4. Results and Characterization of Microstage Zipper Actuators .....	63
3.4.1. Deflection Characterization .....	63
3.4.2. Voltage Characterization .....	65
3.4.3. Dynamic Characterization .....	68

3.4.4.	Mechanical Durability and Reliability Testing.....	69
3.5.	Design Capabilities of Microstage Zipper Actuators.....	70
3.5.1.	Benchmarking.....	72
3.6.	Summary.....	74
Chapter 4:	Conclusion.....	76
4.1.	Contributions.....	77
4.2.	Future Work.....	78
4.2.1.	Design and Model Improvement.....	78
4.2.2.	Large and Individually Addressable Arrays.....	81
4.2.3.	Load Bearing Modeling and Testing.....	82
4.2.4.	Stable Stepwise Displacement.....	83
Appendix A:	Recipes and SOPs.....	86
Appendix B:	EPPA Calculations and Notes.....	93
Appendix C:	Gallery of Spiral Geometries and other Images.....	97
References.....		100

## List of Tables

Table 1: Material properties of Si and SiO <sub>2</sub> used in modeling.....	26
Table 2: Design capabilities of Si/SiO <sub>2</sub> zipper actuators. Cells highlighted green show favorable performance, while cells highlighted yellow show the design tradeoff. .....	36
Table 3: Normalized EPPA's for Si/SiO <sub>2</sub> zipper actuators and established zipper actuators .....	38
Table 4: Microstage actuators of various footprints and geometries. Measured deflections are compared to analytically and numerically modeled deflections. .....	65
Table 5: Mode shapes and resonant frequencies for fabricated 1mm actuator. ....	69
Table 6: Possible design inputs demonstrating the extreme capabilities of the microstage actuator. Cells highlighted in green represent the extreme value, while those in yellow represent the tradeoff in other areas needed to achieve the extreme result.....	71
Table 7: EPPA scores for Si/SiO <sub>2</sub> actuators compared to established out-of-plane actuators. ....	73



## List of Figures

Figure 1: Scanning Electron Microscope (SEM) image of an electrothermal transduction microactuator [7]. .....	4
Figure 2: SEM of lateral comb-finger microactuator [8]. Asymmetric comb fingers (top left) are attached to a flexure (spring) through the shuttle, the honeycomb structure. ....	5
Figure 3: Curved electrode electrostatic zipper actuator [20]. ....	6
Figure 4: Zipping sequence of electrostatic zipper actuator. (a) A bimorph beam at rest in its naturally deflected position, (b-d) begins to zip when voltage is applied, and (e) actuates completely down to the lower electrode. Notice that as the beam actuates, the contact point propagates along the length of the beam towards the free end. ....	7
Figure 5: Schematic and nomenclature of the zipper actuator. ....	17
Figure 6: Beam transformation .....	19
Figure 7: First four modes of vibration of a zipper beam using COMSOL. ....	27
Figure 8: Fabrication of Si\SiO <sub>2</sub> cantilever beams. Begin with (a) an SOI wafer and grow thermal oxide (b). (c) Pattern beams through DRIE. (d) Pattern backside "windows" using DRIE, and (e) Affix to electrode. ....	28
Figure 9: SEM cross section of SOI before device fabrication. The SEM can be used, to a degree, to measure film thicknesses. ....	28
Figure 10: Cross section SEM of a trench etched with the "negative" DRIE recipe. The bottom of the trench measures 60 μm wider than the top. ....	29
Figure 11: Si\SiO <sub>2</sub> zipper actuators after fabrication. (a) Negative etch was not used in DRIE, and there is an abundance of silicon micrograss visible. (b) Negative etch was used, no grass is visible on backside of zipper beams. ....	30
Figure 12: Cantilever zipper actuators of various shapes and sizes. ....	30
Figure 13: Fully released 1750 μm cantilever zipper actuator. An optical defocusing measurement of beam deflection is shown inset. ....	32
Figure 14: Agreement between analytic model for beam deflection, and actual deflection using optical defocusing. ....	32
Figure 15: COMSOL model of 2000 μm beam with total deflection of 315 μm, in correlation with analytic and measured values for 2000 μm beam. ....	32
Figure 16: (a) Round spiral (b) square spiral and (c-d) COMSOL spirals, all exhibiting "bird-nest" phenomena. (d) COMSOL model illustrating the theory behind the bird-nest phenomenon. ....	44
Figure 17: Profile of the microstage actuator, exhibiting the patterned oxide segments that enable large deflections. ....	45
Figure 18: a) Model of a microstage actuator. Careful examination shows that each beam has a curved segment and then a linear segment. (b) Side view and (c) top view. ....	46
Figure 19: Microstage geometry in 2D drawn in COMSOL .....	51
Figure 20: After the geometry is drawn, it is extruded into the 3rd dimension by the thickness of the beams, and materials are assigned. ....	51
Figure 21: Microstage fabrication process. ....	53

Figure 22: Frontside of the SOI, after frontside patterning has been completed. The dark color is the silicon of the beams where the oxide has been selectively removed. Photoresist will be spun over this pattern and then bonded face down onto a carrier wafer to begin backside processing. Underneath the patterned beams lie the BOX and the backside of the wafer. (a) A single actuator, and (b) an array of actuators. ....	54
Figure 23: (a) A 1 mm actuator after fabrication and release from the carrier wafer. (b) The same 1mm actuator turned upside down. The selective patterning of the oxide is visible. (c-d) Close up view of selective oxide patterning.....	55
Figure 24: A damaged quad-flexure microstage.....	56
Figure 25: A precursor to the microstage, tip deflection is 300 $\mu\text{m}$ . ....	56
Figure 26: An odd design, total deflection is greater than 1mm.....	56
Figure 27: "Inverted" microstage, anchored at the center.....	56
Figure 28: A 4x4 array of 1.2 mm microstages. ....	56
Figure 29: Close-up of 1mm microstage array. ....	56
Figure 30: Patterned silicon electrode wafer. The oxide covered segments of an array of actuators would be aligned to the protruding silicon segments shown here.	58
Figure 31: A microscope image of four cantilever beams almost aligned to the underlying patterned electrode. The white of the underlying electrode can just be seen protruding from the upper edge of the beams. ....	59
Figure 32: Pull-in voltage measurements for 1 mm microstages on patterned electrode. ....	60
Figure 33: (a) IC board with DIP port for actuator package, TTL switch, and manual switch. (b) A 4x4 array of 1.2mm microstages packaged in a DIP. (c) A 5x5 array of 1mm microstages packaged in a different DIP. ....	63
Figure 34: (a) Uniformity of deflection over an array of eighty four 1 mm microstages. An array of twenty four 1 mm actuators is shown inset. (b) Agreement between optical defocusing deflection measurements and the COMSOL model for the microstage. ....	64
Figure 35: Voltage-Deflection curves for two different 1 mm actuators. Voltage was ramped from 0 V and deflection of the center stage was measured until pull-in occurred. Voltage was ramped down until the actuators released. ....	66
Figure 36: (a) An array of 24 1mm microstages in their naturally deflected position at 0 V. Light can be seen reflecting off the curvature of the beams. (b) The entire array pulled-in at $V = 120\text{ V}$ . ....	67
Figure 37: A single 1mm actuator from the array above at (a) 0 V and (b) 120 (V)..	67
Figure 38: (a) A 2mm microstage modeled in COMSOL with deflection of 1228 $\mu\text{m}$ , and (b) a fabricated 2 mm microstage with measured deflection of 1243 $\mu\text{m}$ . For reference, the wafer thickness shown framing the microstage is 525 $\mu\text{m}$ .	71
Figure 39: Electric field created by a voltage applied to actuator beam on unshielded electrode. ....	79
Figure 40: Electric field created by voltage applied to actuator beam on shielded electrode. ....	79
Figure 41: A 5 x 5 pixel array supported by 1 mm microstages underneath. ....	81
Figure 42: Individually addressed actuators raise pixels in a defined pattern. The microactuators can be seen underneath the raise pixels. ....	82

Figure 43: Antenna-like structure defined by raised pixels.....	82
Figure 44: Stable stepping motion achieved with microstage by individually addressed electrodes for each serpentine beam.....	85
Figure 45: The "Humped Spiral" .....	97
Figure 46: The "Quarter Zig-Zag" .....	97
Figure 47: The "Horseshoe" .....	97
Figure 48: The "Serpentine" .....	97
Figure 49: The "Stepper" geometry .....	98
Figure 50: The "Stepper" .....	98
Figure 51: Attempt to warp the beams by patterning the oxide on a an angle. ....	99
Figure 52: Narrower silicon than oxide resulted in greater deflections.....	99
Figure 53: Narrower silicon than oxide coupled with constrained center tips yielded almost 200 $\mu\text{m}$ of deflection.....	99

## List of Abbreviations

BOX:	Buried Oxide	NMP:	N-Methyl-2-pyrrolidone
C <sub>4</sub> F <sub>8</sub> :	Octafluorocyclobutane	OD:	Optical Defocusing
DI:	Deionized water	PR:	Photoresist
DIP:	Dual in-line package	RIE:	Reactive Ion Etching
DRIE:	Deep Reactive Ion Etching	SEM:	Scanning Electron Microscope
EBR:	Edge Bead Removal	SF:	Safety Factor
EPPA:	Electromechanical productivity per area	Si:	Silicon
FEM:	Finite Element Modeling	SiO <sub>2</sub> :	Silicon dioxide
HAR:	High aspect ratio	SOI:	Silicon-on-Insulator
IC:	Integrated Circuit	SR:	Stroke Ratio
ICP:	Inductively Coupled Plasma	TFMG:	Thin Film Metallic Glass
MEMS:	Microelectromechanical Systems	TTL:	Transistor to transistor logic
		UV:	Ultra violet

## Nomenclature

$\Delta$ .	<i>Gain in deflection per serpentine beam of microstage</i>	$SF$ .	<i>Safety factor</i>
$A$ .	<i>Cross-sectional area of beam</i>	$SR$	<i>Stroke ratio</i>
$F_{in}$ .	<i>Force variable in COMSOL</i>	$U_e$ .	<i>Electrostatic potential energy</i>
$F_b$ .	<i>Blocking force of actuator</i>	$U_m$ .	<i>Mechanical potential energy</i>
$g$ .	<i>Dielectric gap</i>	$V_{BD}$ .	<i>Dielectric breakdown voltage</i>
$h$ .	<i>Thickness of a layer</i>	$V_{PI}$ .	<i>Pull-in voltage</i>
$h_{o2}$ .	<i>Thickness of secondary oxide</i>	$w_t$ .	<i>Transformed beam width</i>
$I$ .	<i>Area moment of inertia</i>	$\bar{y}$ .	<i>Neutral axis location</i>
$\bar{I}$ .	<i>Total area moment of inertia</i>	$\beta$ .	<i>Beam transform coefficient</i>
$k$ .	<i>Spring constant of cantilever beam</i>	$\delta$ .	<i>Tip deflection of cantilever</i>
$k_{beam}$ .	<i>Spring constant of single beam in the microstage</i>	$\delta_{one}$ .	<i>Tip deflection of first beam in microstage serpentine flexure</i>
$k_{eff}$ .	<i>Effective spring constant of the microstage</i>	$\delta_{stage}$ .	<i>Total deflection at center of microstage platform</i>
$L$ .	<i>Length of cantilever beam</i>	$\delta_{two}$ .	<i>Total deflection at tip of second beam in microstage flexure</i>
$L_c$ .	<i>Length of curved segment in microstage beams</i>	$\epsilon$ .	<i>Dielectric permittivity</i>
$m$ .	<i>Tip slope of microstage beams</i>	$\nu$ .	<i>Poisson's ratio</i>
$n$ .	<i>Number of beams in series in microstage</i>	$\rho$ .	<i>Density</i>
		$\sigma_o$ .	<i>Intrinsic stress</i>
		$\tau$ .	<i>Mechanical switching time</i>



# Chapter 1: Introduction

## 1.1. Background

An effort to study the performance of MEMS actuators and sensors has been attempted by dividing the *kingdom* of MEMS into *families*, *classes*, and *members* [1]. Within the *kingdom* of MEMS actuators (as opposed to MEMS sensors, whose design goals are markedly different than actuators, though their mechanics might be similar) is the *family* of electrostatic actuators, whose *classes* consist of actuators such as the electrostatic comb-drive, parallel plate, scratch, repulsive, and curved electrode, among others.

Yet there is a larger genre that envelopes all of these actuator types, even before the *kingdom* level – a classification based on the plane in which actuation occurs. Namely, whether the device actuates within the plane in which it lies (lateral actuation) or in the plane perpendicular to which it lies (vertical actuation). The authors in [1] do not distinguish between these but for the purpose of framing the place of the topic of this thesis amongst its peers, the distinction is highly relevant. Although many methods for lateral actuation have been developed, conventional MEMS fabrication techniques do not generally accommodate out-of-plane motions. Though a handful of methods for achieving out-of-plane deflection have been demonstrated, it has been a challenge to conceive of techniques that can realize substantial out-of-plane motion.

Actuators with large out-of-plane displacement could be used in many different applications. Recent advances in biomedical imaging techniques, requiring

the ability to focus microlenses, have potential to impact the detection of cancers and other malignancies at the cellular and sub-cellular levels [2]. Smaller endoscopic tubes are less invasive, and therefore a microactuator capable of vertical motion would be ideal for adjusting the position of a lens to capture images, or focus laser light. In other applications, vertical actuators can be used to manipulate reprogrammable arrays of pixels or dots. These pixels could be used to build an antenna capable of changing its shape, and thus its signal send/receive properties, a technology being developed by Syntonics LLC [3].

Along the same lines, vertically mobile pixels could be used to construct refreshable Braille readers, or e-books for the visibly impaired. Another possible application is the realm of haptics, or tactile feedback technology, in which virtual objects can be computer programmed to simulate real world objects with different shapes, textures and feels [4]. Imagine an online shopper searching for a new winter coat touching the computer screen to “feel” the coats material texture. Microactuators that can provide large vertical motion in small footprints can be used to morph a 2D pixilated computer screen, into a 3D haptic interface that can digitally communicate with users through a new dimension – the sense of touch. Haptic technology is already in use today in the form of computer game controllers which vibrate or impart some other touch-based sensation in parallel with what the user views on the screen – vibrations during a collision, recoil from a gun being fired, etc. But there are many other applications of haptic technology that have not yet been put to thought, and some of these may become reality through the use of microscale out-of-plane actuators. Lastly, the world of robotics is filled with actuators on all scales that serve

to meet the robot's end function. Currently, many types of actuators – piezoelectric, magnetostrictive, electromagnetic – are used to make the robot mobile and to achieve locomotion. However, there is room for improvement in terms of actuator performance and efficiency. The force output of magnetostrictive and electromagnetic actuators is governed by magnetic fields, which decrease as they scale down to the micro world [1].

Indeed, as will be discussed later, there are a handful of methodologies that have achieved out-of-plane actuation, though each with some limitation – unrealistic power draw for use in some applications, or forces so low as to make the actuator impractical in certain situations. Metrics such as power consumption, applied voltage and response time are directly linked to the electromechanical productivity<sup>1</sup> of the actuator. An out-of-plane microactuator with high electromechanical productivity – large deflection relative to the space it occupies, high output force, quick response time, minimal power consumption and/or low voltage operation – and that can be fabricated simply and repeatably is needed to realize new advances in many different scientific realms.

### *1.1.1. Out-of-Plane Large Deflection Microactuators: An Overview*

A number of out-of-plane microactuators have been developed based on electrothermal transduction [5–7] that are capable of large deflections, but the electromechanical productivity of these devices is poor. Power must be continually supplied to hold the actuator in a given state, which results in high average power

---

<sup>1</sup> Not to be confused with electromechanical conversion efficiency, which is the ratio of mechanical work to electrical work over one cycle of operation. Electromechanical productivity is a figure of merit defined in more detail later in this work (§2.5.1).



requirements. Moreover, while electrothermal transduction can generate high output forces, response times are limited by slow rates of heat transfer, leading to slow actuator response times. [7] report an electrothermal bimorph used to manipulate a micromirror (Figure 1). The bimorph consists of metallic layers whose coefficients of thermal expansions do not match. When power is applied to the bimorph, the generated heat causes the bimorph layers to expand at different rates resulting in beam curvature capable of actuating a micromirror. They report 200  $\mu\text{m}$  deflections at an actuation voltage of only 6 V in a relatively small area of 0.7 mm x 0.32 mm. They make no mention of the current draw required to maintain actuation. In a similar concept, [6] employ electrothermal bimorphs in attaining large vertical deflections greater than 0.9 mm. However, the device draws almost 200 mW of power, reaches operating temperatures of over 250  $^{\circ}\text{C}$ , and has a slow transient response time of almost 25 ms, a fundamental limitation due to the heat transfer mechanics of thermal transduction.

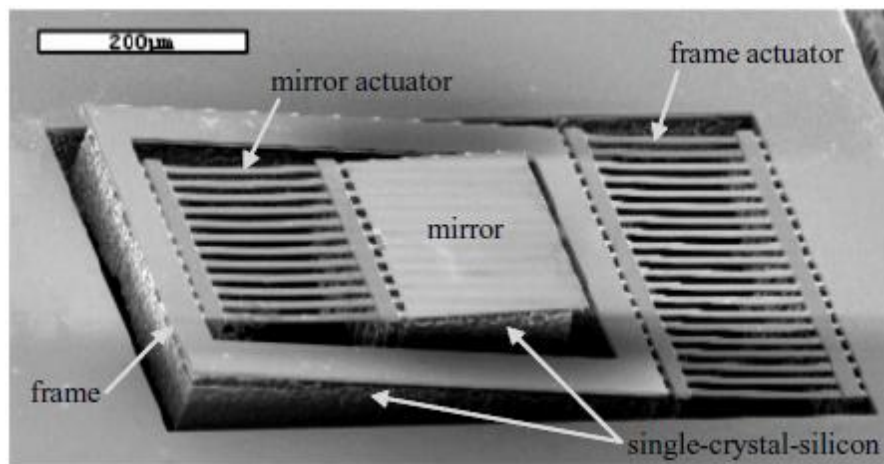


**Figure 1: Scanning Electron Microscope (SEM) image of an electrothermal transduction microactuator [7].**

Developed originally for actuation in the lateral direction [8], asymmetric comb drive actuators have also been developed for out-of-plane actuation as well [9–12]. In vertical comb-drive actuators, comb-like fingers protrude from the ground and movable electrode, asymmetrically aligned with each other and separated by a defined gap (Figure 2). Electrostatic force is generated due to fringing fields when a voltage bias is applied to one electrode, and is proportional to the number of fingers in the design and inversely proportional to the gap between the fingers. Used for manipulating micromirrors in microoptics, deflections on the order of tens of microns are considered large. However, maximum deflection is constrained by the thickness of the active silicon layer used for comb drive fabrication, placing an upper limit on this key actuator metric. Furthermore, output force is limited by the relatively low coupling strength associated with comb drive fringing fields. Since the electrostatic force is proportional to the number of fingers, comb-drives often occupy large areas in order to accommodate the large number of fingers needed to generate the required electrostatic force.

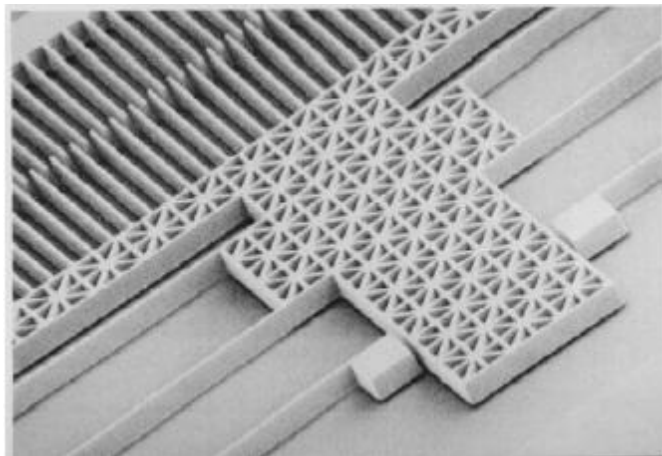


**Figure 2: SEM of lateral comb-finger microactuator [8]. Asymmetric comb fingers (top left) are attached to a flexure (spring) through the shuttle, the honeycomb structure.**

An alternative electrostatic actuator design that overcomes the limitations inherent to asymmetric comb drives is based on parallel-plate actuation using a “zipper” topology [13–19]. Pioneered by [20] for lateral actuation, and adapted later for vertical actuation, the beam is switched between states by application of a voltage across a dielectric film separating the beam and a parallel curved electrode (Figure 3). By selecting a dielectric layer with high permittivity, large electrostatic forces are generated at the anchor point, where the gap between the free beam and fixed curved electrode is at its minimum. As the beam is pulled to the electrode, the contact point propagates along the beam until the entire structure is pulled to the dielectric-covered electrode surface (Figure 4). Because zipper actuators employ a form of parallel-plate electrostatic transduction, they are capable of significantly higher forces than their comb drive counterparts, while providing rapid switching limited by inertia rather than heat transport as in the case of electrothermal actuation.

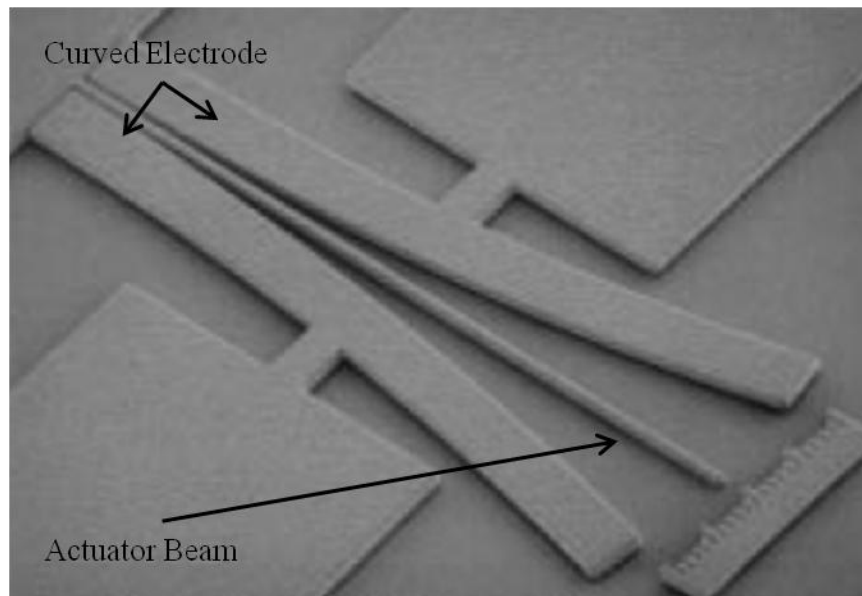


**Figure 3: Curved electrode electrostatic zipper actuator [20].**

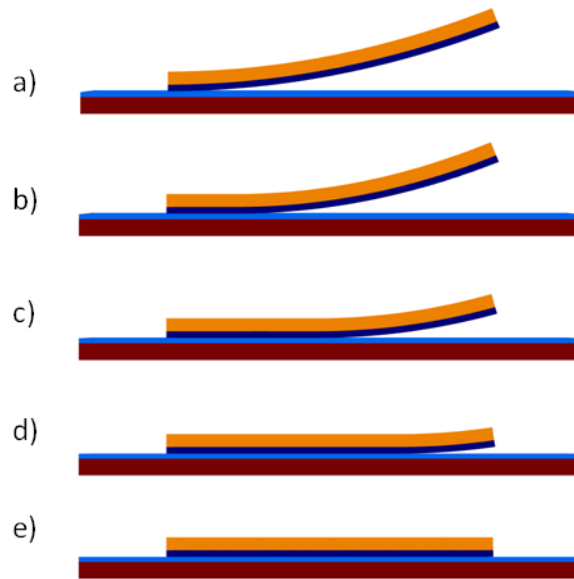


**Figure 4: Zipping sequence of electrostatic zipper actuator. (a) A bimorph beam at rest in its naturally deflected position, (b-d) begins to zip when voltage is applied, and (e) actuates completely down to the lower electrode. Notice that as the beam actuates, the contact point propagates along the length of the beam towards the free end.**

A clever use of the curved electrode is demonstrated in [21], in which the authors fix a large mass to the tip of the free beam, call it a “tulip” actuator, and use it to manipulate a haptic display. Upon actuation, the tulip head moves as the beam actuates, comes in contact with an inverted cone lifting the cone vertically. The ability to lift the cone is due to the high force output of electrostatic zipper actuators.

Out-of-plane zipper actuators operate using the same principles as curved electrode lateral zipper actuators, and typically consist of thin film cantilever bimorph beams fabricated with an engineered stress gradient causing the beam to curve away from the substrate (Figure 4(a)). Established out-of-plane zipper microactuators are most commonly fabricated from thin film metallic bimorphs, with film properties selected to achieve the desired stress gradient and resulting curvature in the overall bimorph. For example, zipper microactuators based on chromium/aluminum [13],

thin film multilayer gold [15], and polysilicon/gold [22] have been described. However, because thickness of the actuators is typically on the order of a few micrometers, total output force for these designs is quite low. In addition, because the devices are based of cantilever beam configurations, tip trajectories follow a curved path with variable beam slope over the course of a single stroke, constraining their use to applications where purely vertical output displacements are not required.

One particularly interesting class of zipper actuator employs a homogeneous layer of thin film metallic glass (TFMG) as the actuator beam material [23–25]. Rather than relying on a stress gradient within a bimorph structure to achieve the desired beam curvature, an initial strain field is instead engineered into the TFMG structure during fabrication by heating the material while applying a mechanical force at the tip to deform the released beam, then cooling the conductive amorphous alloy to fix the beam in its deformed state. This approach has enabled the realization of unique zipper designs such as out-of-plane spiral actuators capable of achieving tremendous out-of-plane deflections. The use of TFMG films on the order of 10  $\mu\text{m}$  thick can provide higher output forces (close to 1 mN) than related thin film devices, and the conical design allows for high stroke ratios (the ratio of deflection to the largest dimension of the actuators footprint). However, TFMG actuators are limited in a number of aspects. The fabrication process is relatively complex and is sensitive to the heating and cooling temperatures and the rates at which they are changed - temperatures can be as high as 600  $^{\circ}\text{K}$ . Moreover, the deflection is defined mechanically, which can be cause for non-uniformity and lack of repeatability.

Indeed, the authors attribute differences in total deflections amongst an array of 100 actuators to the method of mechanically inducing deflection.

Though there are other out-of-plane actuators capable of achieving measurable deflections, such as piezoelectric actuators [26], each has its own limitations in terms of electromechanical productivity that affect the performance of the actuator. Electrothermal transduction requires continuous power input and results in slow response times. Electrostatic comb drives could theoretically offer large deflections but at low forces and large device footprints. Thin film metallic glass actuators show promise in terms of output performance, but have inherent fabrication challenges that make them complex and incapable of consistent fabrication and performance. On the other hand, electrostatic zipper actuators show promise with regard to output performance, particularly in terms of deflection, forces and electromechanical productivity. Currently, though, because zipper actuators are based on cantilever beam configurations, tip trajectories follow a curved path with variable beam slope during actuation, making them unsuitable to applications where purely vertical displacements are necessitated.

### *1.1.2. Out-of-Plane Large Deflection Electrostatic Zipper Actuators*

This work presents a novel electrostatic zipper microactuator technology, inspired by the geometry of the electrothermal actuator in [5], capable of providing exceptionally large deflections and high output forces using a simple silicon-on-insulator / deep reactive-ion etching (SOI/DRIE) fabrication method [20]. Moreover, the unique fabrication process and optimized geometry culminate in a flat center stage, or “microstage”, whose deflection is vertical with negligible lateral translation. The

actuators employ a patterned thermal SiO<sub>2</sub> film grown from the surface of the active layer of an SOI wafer. Compressive stress in the SiO<sub>2</sub> results in well-defined initial beam curvature, while also serving as a high quality and pinhole-free dielectric for efficient electrostatic actuation. In comparison to thin film metals, thermal oxide can be grown from silicon in a highly controlled process that allows for precise and repeatable residual stress gradients within the Si/SiO<sub>2</sub> bimorph. According to the MEMS Materials and Processes Handbook, “Of all the thin-film growth processes used in MEMS, oxidation of silicon is one of the most straightforward owing to the simplicity of the process...” [27]. The use of SiO<sub>2</sub> for both curvature control and dielectric isolation provides significantly larger deflections and forces than traditional zipper actuators while reducing pull-in voltages needed for actuation.

Multiple actuators connected in parallel to a central stage are further demonstrated for realizing large-displacement vertical stage positioning without any appreciable lateral translation (hereafter called the “microstage”). By selectively patterning the oxide layer, sequential segments consisting of curved and straight beam elements are generated, allowing the formation of serpentine beams capable of providing high output deflection within a small actuator footprint.

Using two serpentine beams with optimized oxide elements connected in parallel to a silicon microstage, vertical stage deflections as high as 1.2 mm have been achieved within a 1 mm<sup>2</sup> die area (stroke ratio of 1.2), and modeling results suggest that even greater deflections can be achieved within the same footprint. Additionally, the use of thicker Si and SiO<sub>2</sub> to constitute the bimorph provides greater forces than previously reported metallic bimorphs, and are therefore responsible for mechanical

response times (switching time) under 1 ms. In comparison to TFMG actuators, the fabrication process, performed entirely with established MEMS micromachining techniques, is simple, straightforward and repeatable, and the electrode scheme presented here eliminates any release lag due to stiction or dielectric charging. Unlike actuators based on thermal transduction, electrostatic actuators consume minimal power, if any, and produce negligible heat output. Finally, the square actuator geometry and signal routing methodology provide for a packing density that is limited by the footprint of the actuator itself, allowing for maximal utility of area.

## 1.2. Thesis Goal and Scope

The goal of this thesis is to present a novel out-of-plane electrostatic microactuator that provides improvement in terms of actuator output metrics in comparison to out-of-plane microactuators already established.

The scope of the document is bounded by the realm of large-deflection out-of-plane microactuators manufactured using MEMS microfabrication techniques. A brief outline of existing out-of-plane microactuators has already been presented, as well as the need to push the performance envelope of out-of-plane microactuation. A new microactuator concept is presented and analytic and numeric models are constructed to both predict and validate actual performance. The fabrication process is detailed and finished devices are tested and their performance reported. The performance results are used to validate the models, and the extreme capabilities of the microactuator are presented through model optimization. Microactuators are presented and their performance measured by the following metrics:



1. **Large out-of-plane deflections:** This metric will be studied by means of the stroke ratio (SR): the ratio of total deflection of the microactuator per largest dimension of the area occupied by the microactuator. This metric normalizes the deflection to the actuator real estate required to achieve that deflection, and is a measure of efficiency in terms of deflection output. In this sense, deflections of different Si/SiO<sub>2</sub> microstages can be compared, but even more so, deflections between the microstage and other out-of-plane actuators can be compared. Stroke ratios of 0.18 [23] and 0.24 [15] have been demonstrated for electrostatic zipper actuators.
2. **High output forces:** The average output force of electrostatic actuators (both lateral and vertical) falls between 10<sup>-6</sup> N and 10<sup>-3</sup> N [1], while forces greater than 1 mN have yet to be reported by out-of-plane microactuators with at least 100 μm of deflection.
3. **Low actuation voltage:** Many of the previously fabricated electrostatic actuators require actuation voltages between 100 V and 200 V [13], [15], [23].
4. **Fast Switching Time:** A switching time of 1 ms or less is desired. This places the resonant frequency of the device at or above 1 kHz.
5. **Electromechanical Productivity per Area (EPPA):** This metric will be developed in depth in §2.5.1 and §3.5.1. Essentially it is a figure of merit that quantifies the mechanical output (deflection, force, switching time) achieved per electrical input (voltage), per area. By normalizing the

productivity to the area, it is possible to compare actuators of different shapes and sizes and discuss their productivity.

Given these metrics and the achievements of previous microactuators, the devices presented in this thesis will be benchmarked. It will be shown that the novel Si/SiO<sub>2</sub> electrostatic microstage developed here can outperform the established technologies, with regard to the above metrics, but also with regard to other intangibles, such as ease and reliability of fabrication, mitigation of charging issues, and reliability and mechanical longevity.

### 1.3. Organization

Microfabrication and micromachining can be an expensive endeavor when all processes and designs have been thoroughly tested and perform as they should, but is exceedingly costly in a research environment when the processes themselves are experimental. Therefore, it is worthwhile to develop a method for exploring many different designs, configurations, and geometries, without having to fabricate them to see the results. Models allow for exactly this type of exploration and investigation, at a fraction of the cost and time. Hence, a simple analytic model was developed in MATLAB, and a numeric model was developed in COMSOL, initially in order to determine that the new electrostatic zipper concept did indeed have potential to offer improvements on established zipper technologies, and to later guide the fabrication of the actuators.

Initially, a simple mathematical model is developed to roughly represent the range of performance expected from the zipper actuators, rather than exact performance values. After initial exploration with the model, a round of device

fabrication results in zipper actuators whose performance can be measured and compared with the expected values provided by the model. The model can then be expanded and fine tuned to better parallel observed results. Another round of devices, perhaps more complex, is fabricated and performance measurements are compared to the expected results from the more advanced model. This iterative process cycles until the model performance output is congruent with observed performance, at which point the model is validated. It is at this stage where the second purpose of the model becomes apparent.

Given the fabrication results that support the model theory, the capabilities of the new zipper technology can be examined through the model with a high degree of certainty that the model indeed represents the performance of the devices should they be fabricated and characterized. The time and cost savings of this methodology are immense, without sacrificing much in the way of accuracy and reality.

Therefore, the rest of this thesis will parallel the methodology outlined above as follows:

**Chapter 2** begins the discussion of simple cantilever beam electrostatic zipper actuators. First, the mathematical theory behind their operation is presented and simple analytic and numerical models are developed. The fabrication process is detailed, and actuator performance is characterized, and used to validate the models. Finally, a discussion of the capabilities of the cantilever beam Si/SiO<sub>2</sub> zipper actuators is presented, and the actuators are benchmarked using the criteria outlined above against established out-of-plane cantilever actuators.

**Chapter 3** expands the discussion of electrostatic zipper actuators to the concept of the microstage, a geometry based on zipper actuators that allows for vertical motion with negligible lateral shift. The analytic model from Chapter 2 will be developed further to accommodate the microstage actuators add complexity. A new fabrication process will be outlined, and microstage performance characterization is reported, and used again to validate the model. Finally, a discussion of the microstage capabilities is presented, and the microstage actuators are benchmarked using the criteria above against established out-of-plane vertical motion actuators.

**Chapter 4** concludes this thesis with a summary of the contributions this work makes to science and the field of MEMS, particularly out-of-plane microactuators. A short discussion of future work is presented, outlining some of the research being carried out at the time of publication of this thesis, and that which will be conducted in the future.

**Appendices** can be found at the end of the thesis that can aid the reader in digesting some of the more technical aspects of the document, while also expanding upon some of the peripheral results of this research. **Appendix A** details the processing parameters, etch recipes and standard operating procedures used in fabricating the microactuators. **Appendix B** contains expanded information on the benchmarking methodology and calculations. **Appendix C** is a gallery of images of actuator designs that did not prove successful.

## Chapter 2: Electrostatic Zipper Actuators: Cantilever Beams

### 2.1. Introduction

This chapter begins the investigation of simple cantilever Si/SiO<sub>2</sub> electrostatic zipper actuators. As outlined above, a model is developed and presented, devices are fabricated, and their results are compared to the model. Once the model has been validated a discussion of the extreme capabilities of the new electrostatic zipper actuators is presented. In terms of progression of research, it is the performance of the simple zipper actuators that allowed the research to graduate to the more complex microstages.

### 2.2. Theory and Modeling

The basic mathematics and theory behind electrostatic zipper actuation is well understood. Though many authors have done a thorough and admirable job of describing the mechanics [13], [15], [18–22], they will be presented here as well, along with a few changes, to enhance the understanding of what is put forth in this paper.

#### 2.2.1. *Analytic Model – MATLAB*

##### 2.2.1.1. Beam Deflection Due to Residual Stress

The basic operation of electrostatic zipper actuators was presented in §1.1.1, but a more in depth treatment is presented below in conjunction with the development of the model.

Wet thermal growth of silicon dioxide from silicon creates a residual stress in the oxide that causes the Si/SiO<sub>2</sub> bimorph to bend. A schematic of the zipper actuator

is shown in (Figure 5). At equilibrium, the bimorph's internal moments and axial forces must sum to zero, with the result that the strain in each layer at the interface must be equivalent.

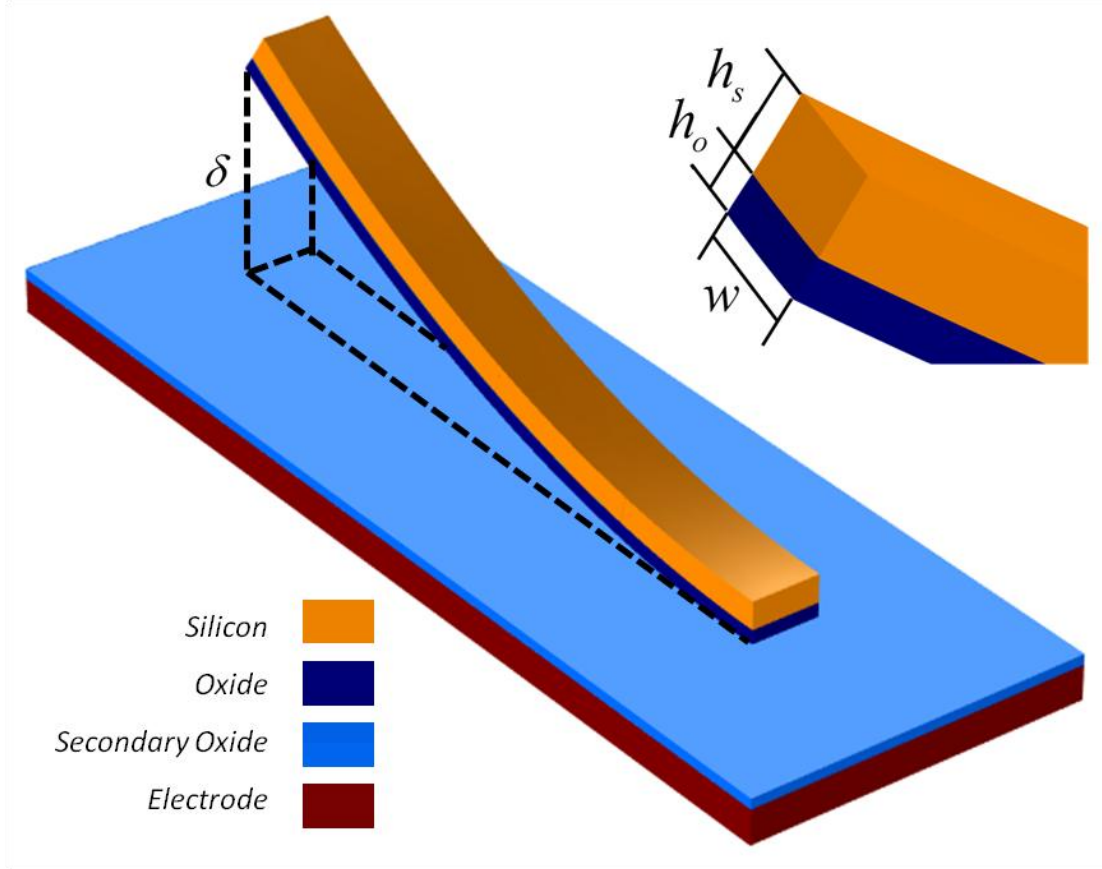


**Figure 5: Schematic and nomenclature of the zipper actuator.**

Anchoring one end of the beam to the ground plane, the stress in the oxide causes the tip to deflect through the following relationship [28]:

$$\delta(L) = \frac{\epsilon L^2 (h_o + h_s)(A_o E_o A_s E_s)}{(h_o + h_s)^2 A_o E_o A_s E_s + 4(A_o E_o + A_s E_s)(E_o I_o + E_s I_s)} \quad (1)$$

where the subscripts “o” and “s” refer to the oxide layer and silicon layer respectively,  $L$  is the beam length,  $h$  is the thickness of the subscripted layer,  $A$  is the

cross-sectional area of the subscripted layer,  $I$  is the area moment of inertia, and  $\epsilon$  is the strain, given by

$$\epsilon = \frac{\sigma_o}{E_o}. \quad (2)$$

$E$  is the Young's Modulus for thermal silicon dioxide,  $\sigma_o$  is the residual stress of the oxide, and both assume an isotropic Poisson's ratio ( $\nu$ ) so that

$$E_s \rightarrow \frac{E_s}{(1-\nu_s^2)} \quad (3)$$

$$E_o \rightarrow \frac{E_o}{(1-\nu_o^2)} \quad (4)$$

$$\sigma_o \rightarrow \sigma_o(1+\nu_o). \quad (5)$$

#### 2.2.1.2. Mechanical Force and Beam Stiffness

The model continues with the calculation of the spring constant,  $k$ , of the bimorph. First the bimorph is transformed into a unimorph by converting the oxide layer, of width  $w$ , into an equivalent silicon layer of different width,  $w_t$  (Figure 6) [29]. The width  $w_t$  of the newly transformed silicon layer can be defined as

$$w_t = \beta w \quad (6)$$

where  $\beta$  is the conversion factor defined by

$$\beta = \left( \frac{E_o}{E_s} \right). \quad (7)$$

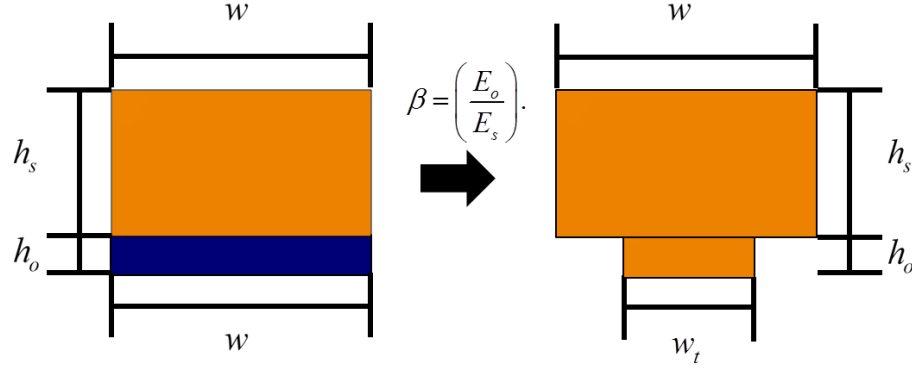


**Figure 6: Beam transformation**

Defining the oxide as the bottom layer, the position of the neutral axis ( $\bar{y}$ ) of the newly shaped cross-section of the beam can be found as follows

$$\bar{y} = \frac{(wh_s \left( \frac{h_s}{2} + h_o \right) + w_t h_o^2)}{wh_s + w_t h_o}, \quad (8)$$

and the total area moment of inertia,  $\bar{I}$ , is defined by

$$\bar{I} = \frac{1}{12} wh_s^3 + wh_s \left( \frac{h_s}{2} + h_o - \bar{y} \right)^2 + \frac{1}{12} w_t h_o^3 + w_t h_o \left( \bar{y} - \frac{h_o}{2} \right)^2. \quad (9)$$

Once the above calculations are carried out the effective bending stiffness of the beam can be determined. The effective bending stiffness,  $EI$ , is expressed as

$$EI = E_s \bar{I}, \quad (10)$$

and allows us to calculate the spring constant of the beam. For a cantilever beam, whose boundary conditions are defined as “fixed-free” [30], the spring constant, or stiffness of the beam, is written as

$$k = \frac{3EI}{L^3}. \quad (11)$$



As always, it is wise to verify the results and a logical check informs us that what we have presented thus far is indeed valid. For a given material, the bending stiffness defined in (10) is governed entirely by the widths and thicknesses of the various layers. Intuition tells us that if the beam were to grow thicker, it would be more difficult to bend, and indeed,  $EI$  would increase with greater thickness. Similarly, the stiffness,  $k$ , should increase as well, and it would, since it varies proportionally with  $EI$ . Finally, intuition and experience tell us that the longer a beam is, the easier it is to bend. Hence equation (11) is valid since a longer beam would decrease the spring constant, which represents the beams resistance to an applied force.

This concept has been formalized as Hooke's Law, which expresses the relationship between the force applied to an elastic object and the distance it travels as

$$F = kx, \quad (12)$$

where  $F$  is applied force and  $x$  is the distance the elastic object moved due to the force. Relating the two is the stiffness,  $k$ , of that elastic object, and the bimorph cantilever beam employed in zipper actuation is a classic example of an elastic object. This derives from the mechanical potential energy,  $U_m$  stored in a deformed elastic object, expressed as

$$U_m = \frac{1}{2}kx^2, \quad (13)$$

where the subscript “ $m$ ” denotes mechanical. With this understanding of the mechanics of the zipper actuator, we can begin to discuss the electrostatic aspect.

### 2.2.1.3. Electrostatic Force and Pull-in Voltage

When a voltage is applied across the dielectric separating the two electrodes, an electrostatic potential is generated that pulls the beam down towards the ground electrode. As the beam moves away from its equilibrium position, an elastic restoring potential based on equation (13) is generated that opposes the electrostatic potential. The electrostatic potential between two electrodes,  $U_e$ , is defined as [20]

$$U_e = \frac{\epsilon AV^2}{2g}, \quad (14)$$

where  $\epsilon$  is the permittivity of the space between the electrodes,  $A$  is the surface area of the beam that comes into contact with the electrode,  $V$  is the applied voltage, and  $g$  is the fixed gap between the electrodes defined by the thickness of the dielectric. Therefore the total potential energy is

$$U_t = U_m + U_e. \quad (15)$$

The system is at equilibrium when the first derivative of (15) is zero, that is, when the electrostatic force and the elastic restoring force are equal. Moreover, for this equilibrium to be stable, the second derivative of (15) must be less than zero, but in generally used electrostatic actuation it is positive, leading to an instability commonly referred to as the “pull-in” phenomena. Essentially, the voltage bias increases to a point where the electrostatic force it generates is greater than the mechanical restoring force the beam can output, and the beam collapses, or “pulls-in” to the lower electrode. In the classic case of parallel plate actuators, the pull-in phenomenon dictates that the maximum deflection the free electrode can achieve is 1/3 the initial gap between the electrode plates [15], [31]. However, in this zipper actuator scheme,

the gap at the anchor between the electrode plates is fixed by the thickness of the dielectric layer. Using (13) and (14) and the Rayleigh-Ritz method developed in [20] we arrive at the expression for  $V_{PI}$ :

$$V_{PI} = \sqrt{\frac{EIg}{w\epsilon\mathfrak{R}^2}}, \quad (16)$$

where  $\epsilon$  is the effective dielectric permittivity and  $\mathfrak{R}$  is the radius of curvature of the beam:

$$\mathfrak{R} = \frac{L^2}{2\delta}. \quad (17)$$

To the first order,  $V_{PI}$  does not change with the width or length of the beam, but rather varies as function of the beam properties, dielectric gap thickness and radius of curvature. Upon closer inspection, it can be uncovered that  $\mathfrak{R}$  is determined by fixing the respective thicknesses of each bimorph layer, and is independent of  $L$ . Therefore, the pull-in voltage is the same for all beams of same layer thicknesses regardless of the length or width of the beam.

It is important to note that the model does not account for fringing field effects. When a voltage is applied across the dielectric, an electric field is established by the charges accumulating in the electrodes. It can be seen from equation (14) that only in the case of a fixed gap,  $g$ , and area,  $A$ , is the voltage responsible for driving a stronger electric field and therefore a stronger electrostatic force. However, this model is an approximation for two infinite plates between which the electric field is uniform and linear from one plate towards the other. In reality, the two electrodes are of finite dimensions causing the field to become much more complex and non-linear near the edges, or “fringes”, of the electrodes. Much effort has been devoted to

modeling the effect that fringing fields have on capacitance, the overall electric field, and the resulting electrostatic force, and to developing mathematical representations to model those effects [32]. Nonetheless, the presence of electrostatic fringing fields will cause an increase in electrostatic force resulting in lower pull-in voltages. However, the presence of a ground plane results in unbalanced field distribution, which serves to increase electrostatic forces, growing stronger with larger gaps [20].

Additionally, the use of two dielectric layers creates undefined boundary conditions within the dielectric stack which can result in residual charge buildup, better known as dielectric charging. The presence of accumulated charge creates a parasitic electric field that decreases the strength of the electric field created by the actuation voltage. As such, the actuation voltage must be increased to compensate and provide the necessary electrostatic force to achieve pull-in. The voltage model here does not account for the effects of dielectric charging either.

Moreover, the model also assumes that the two facing electrode surfaces are planar. In the case of micromachined silicon wafers, this is easily achievable since “polished” wafers can be purchased that are nearly atomically smooth. However, as will be discussed later in §3.3.3.2, the lower electrode here has a deliberate surface roughness, which also results in unknown and unmodeled changes to the electrostatic force.

Ultimately, it is clear that there are many complex variables that are unaccounted for in this model influencing the value of the pull-in voltage. As such, it can be expected that experimental results will differ from the model output. This is satisfactory provided that observed values differ consistently and predictably, since

the ultimate goal of this work is *not* to develop a model for electrostatic zipper actuation (See [14-16],[18-21],[33], for many different already established models), but rather to develop out-of-plane microactuators that can be consistently and predictably fabricated leading to repeatable and reliable performance.

As an aside, a novelty of the electrostatic actuator presented here is the fact that the SiO<sub>2</sub> serves the dual purpose of inducing deflection *and* acting as a high quality dielectric. In reality the cantilever beams can be actuated on an unshielded exposed electrode, since the oxide that is part of the beams will serve as the dielectric. In this study, though, the lower fixed electrode is also coated in a secondary layer of SiO<sub>2</sub>. This is for the purpose of being able to compare the performance of simple cantilever beams to the more complex microstages presented later, which necessitate a secondary dielectric layer. Given the variables unaccounted for by the voltage model, this allows for direct comparison between the zipper beams and microstages.

#### 2.2.1.4. Tip Force and Switching Time

Finally, we can model the switching time ( $\tau$ ) and blocking force ( $F_b$ ) of the zipper actuator. We model the bimorph as a clamped-free beam, whose mass is the mass of the beam itself, so that

$$\tau = 2\pi\sqrt{\frac{m_{beam}}{k}} = 2\pi\sqrt{\frac{m_{beam}L^3}{3EI}}, \quad (18)$$

and the blocking force is

$$F_b = k\delta. \quad (19)$$

The blocking force is defined as the force required to deflect the tip of the beam down to the ground plane.

The switching time and blocking force are valuable performance metrics because they determine the actuators capability to perform in certain scenarios, such as moving a load attached to the tip, or for acting as a switch. Indeed, the goal of this thesis is to develop a microactuator with large out-of-plane deflections and high electromechanical productivity. That means, simply, that we are searching for an actuator scheme that produces large deflections, high forces, and responds quickly at low power consumption and/or low voltage. Though they are relatively simple to compute, they are essential in benchmarking the improvement of the zipper actuators developed here.

### *2.2.2. Numeric Model – COMSOL*

A numeric model was developed in COMSOL in parallel to the analytic model to provide a second method through which to study the zipper actuators. Moreover, the lack of access to a tool that could test the blocking force of fabricated actuators necessitated the development of Finite Element Model (FEM) that could simulate the physical response of the actuator to an applied force at the tip. Pull-in voltage was not modeled numerically. Finally, the capabilities of FEM are used to model the resonant frequencies and corresponding mode shapes of the beams, and to determine the time constant numerically as well.

#### *2.2.2.1. Beam Deflection Due to Residual Stress*

The model was developed using COMSOL 4.1-4.3 using the structural mechanics physics module. The beam was drawn with two layers, and the materials were specified as single-crystal-silicon and silicon dioxide from COMSOLs internal material library. The material properties for each, as provided by COMSOL, are

outlined in Table 1. The structural mechanics module also allows for the specification of initial stress to the oxide layer, and for the application of fixed motion constraints to anchor the beam at one end.

**Table 1: Material properties of Si and SiO<sub>2</sub> used in modeling.**

<b>Material</b>	<b><math>E</math> [GPa]</b>	<b><math>\nu</math></b>	<b><math>\rho</math> [kg/m<sup>3</sup>]</b>
Silicon	166	0.27	2330
SiO <sub>2</sub>	70	0.17	2200

Upon solving, the model outputs the deflection profile of the beam based on the given input parameters, and serves as a FEM based method for modeling the deflection of the zipper actuators in parallel to the analytic method.

#### 2.2.2.2. Tip Force and Spring Constant

Additionally, the module supports the ability to apply forces to the beam, which allows for investigation of the stiffness,  $k$ , and consequently the blocking force,  $F_b$ . A force variable,  $F_{in}$ , was created, and applied to the tip of the beam acting towards the ground plane. Using the solvers parametric sweep function, the force variable was swept from 0  $\mu\text{N}$  to 10  $\mu\text{N}$  in 1  $\mu\text{N}$  increments, and the force – deflection curve was plotted where the slope of the line is the stiffness of the beam.

#### 2.2.2.3. Dynamic Modeling

Similarly, FEM allows us to model the dynamic response of the beam, particularly its resonant frequencies and corresponding mode shapes. Using the *Eigenfrequency* study node in COMSOL, we can specify the number of frequencies to find, and output the mode shapes of the actuators. From these values, we can determine the time constant of the devices numerically in addition to the analytic values above.

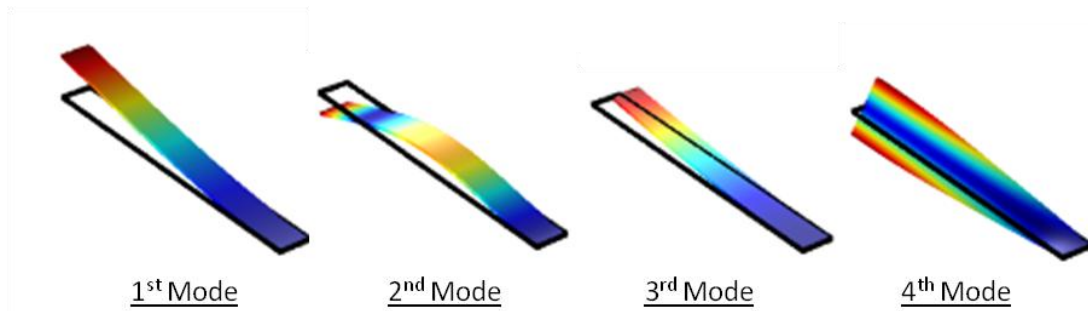


**Figure 7: First four modes of vibration of a zipper beam using COMSOL.**

### 2.3. Fabrication of Cantilever Zipper Actuators

For a more in depth explanation of the fabrication tools and processes used here, please see Appendix A: Recipes and SOPs at the end of this work.

The fabrication of the cantilever microactuators is illustrated in Figure 8. A p-type (100) SOI serves as the base for the actuator fabrication, as shown in Figure 8(a). Thermal silicon dioxide is grown to serve as the dielectric and the stressor to induce beam bending (Figure 8(b)). Figure 9 shows the cross section of an SOI after oxide growth. Photoresist (AZ4620) is spin-coated on top of the oxide, and photolithographically patterned to serve as a mask for the beam patterning. Next, the frontside  $\text{SiO}_2$  is patterned using reactive ion etching (RIE) and then the Si is patterned using deep reactive ion etching (DRIE) to define the actuator beams, as shown in Figure 8(c). DRIE employs the Bosch process, a timed multiplexed etch process that can achieve high aspect ratio (HAR) etches with nearly vertical side walls. It achieves this by alternating deposition of an inert passivation layer ( $\text{C}_4\text{F}_8$ ) with plasma directed ions ( $\text{SF}_6$ ) that attack the wafer from the vertical direction.



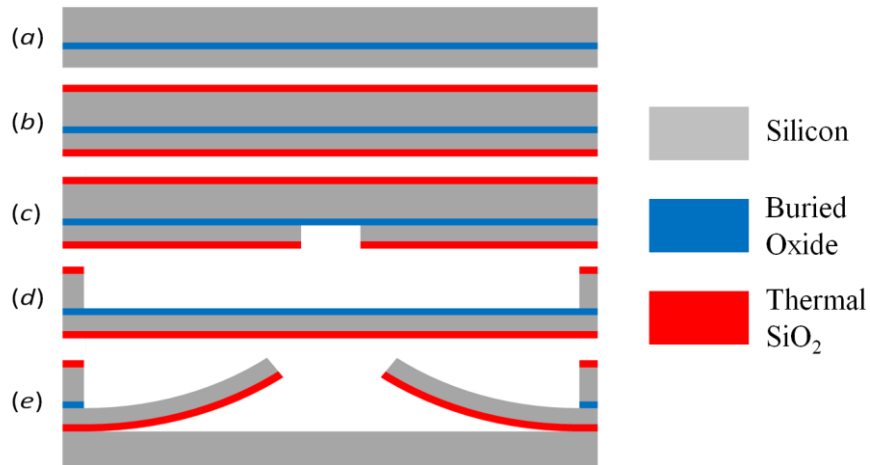


**Figure 8: Fabrication of Si/SiO<sub>2</sub> cantilever beams. Begin with (a) an SOI wafer and grow thermal oxide (b). (c) Pattern beams through DRIE. (d) Pattern backside "windows" using DRIE, and (e) Affix to electrode.**

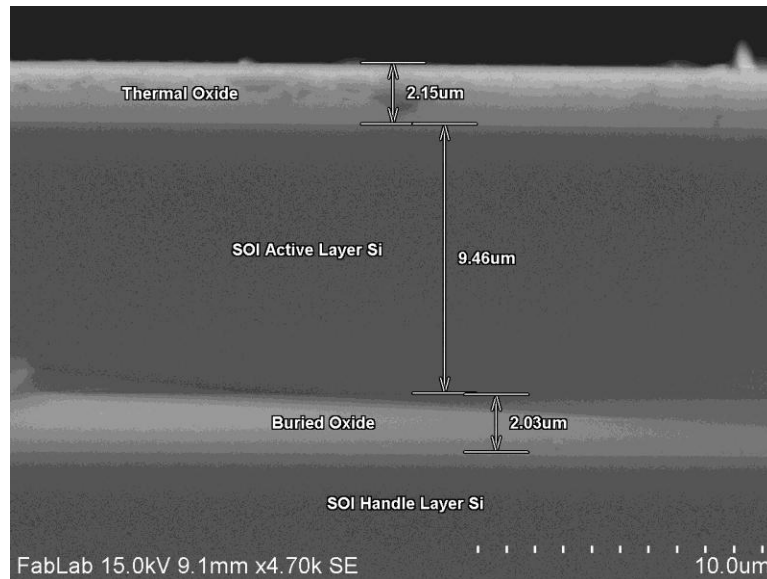


**Figure 9: SEM cross section of SOI before device fabrication. The SEM can be used, to a degree, to measure film thicknesses.**

In this etch process, the 2 μm buried oxide layer (BOX) layer serves as an etch stop for the frontside DRIE. Since the etch rate ratio of Si:SiO<sub>2</sub> in DRIE etching for this particular process was characterized as 50:1 (2.5 μm/min Si and 0.05 μm/min SiO<sub>2</sub>), and the active Si is less than 10 μm thick, the Si can be safely etched, with a 25% over etch without worry of damaging the BOX. The photoresist mask is stripped

from the patterned frontside, and the SOI wafer is mounted to a carrier wafer, frontside down, to begin backside patterning.

A thick layer of photoresist (AZ4620) is spin-coated to the backside, and is photolithographically patterned to serve as a mask for the backside etch. The backside  $\text{SiO}_2$  is removed using the same RIE process as above and the backside Si is then etched using the DRIE process to open backside access down to the BOX, as shown in Figure 8(d). For the backside etch, the multiplexing is tweaked to produce an etch profile whose width at the depth of the etch is slightly wider than that at the etch opening (Figure 10). This creates a negative sidewall profile, which is immaterial with regard to the backside window, but critical for eliminating silicon grass formation, a common problem with DRIE etching. Silicon grass forms when residual material (from the chamber, passivation layer, redeposition of etched material) masks the bottom of etch trench, causing tall grass-like pillars to form as the process continues Figure 11(a). Tweaking the etch process so that a negative etch profile develops will cause any silicon micrograss to be undercut throughout the duration of the etch, leaving the etch trench smooth.

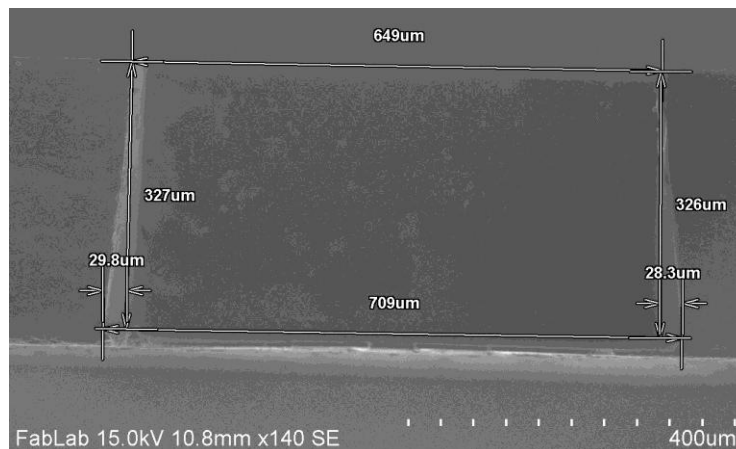


**Figure 10: Cross section SEM of a trench etched with the "negative" DRIE recipe. The bottom of the trench measures 60 μm wider than the top.**

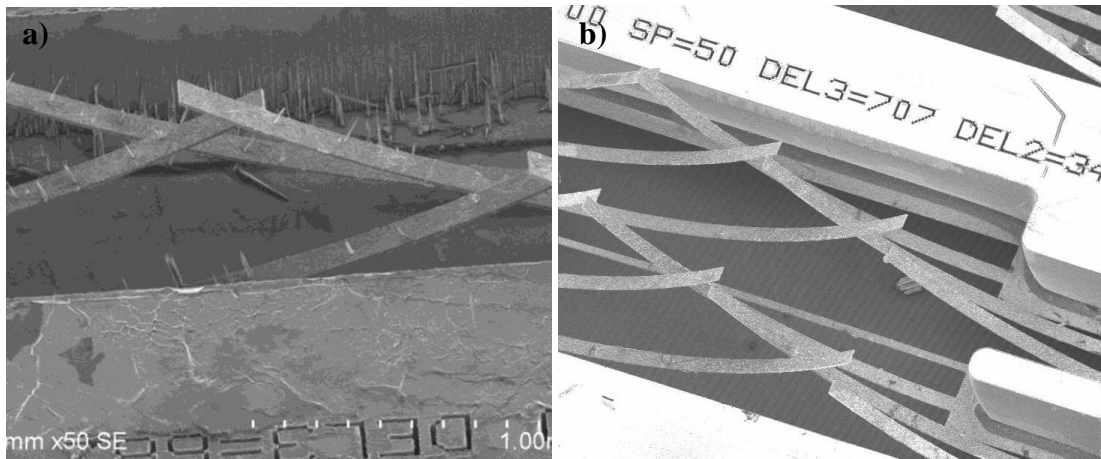


**Figure 11: Si/SiO<sub>2</sub> zipper actuators after fabrication. (a) Negative etch was not used in DRIE, and there is an abundance of silicon micrograss visible. (b) Negative etch was used, no grass is visible on backside of zipper beams.**

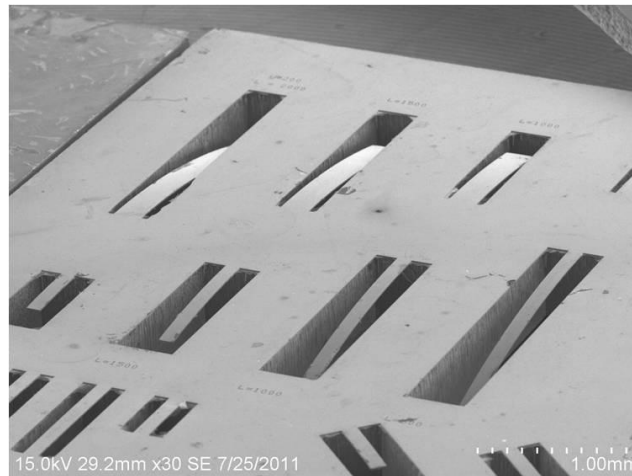


**Figure 12: Cantilever zipper actuators of various shapes and sizes.**

In the fourth and final step, the beams are released in Figure 8(e) using RIE to remove the BOX and an overnight soak in acetone to detach the carrier wafer. The stress induced by the SiO<sub>2</sub> causes the beam to curve upon release. The actuators were diced into 1 cm x 1 cm dies, mechanically clamped to a 1 cm x 1 cm oxide coated electrode, and bonded together by application of fast-setting epoxy to the vertical side walls of the die stack. The fast setting epoxy shrinks as it dries pulling the actuator and electrode dies close together. Moreover, the polymer based epoxy serves as a

high quality insulator to prevent electrical shorting at the edges of the dies. Figure 12 shows a fabricated set of cantilever beams immediately after fabrication before cleaning.

Appendix A: Recipes and SOPs contains process details and standard operating procedures for many of the fabrication steps in this thesis.

## 2.4. Results and Characterization of Cantilever Zipper Actuators

Both the beam tip deflection ( $\delta$ ) and the voltage necessary to “pull-in” the beam ( $V_{PI}$ ), were characterized in this study. Using the process outline above, a set of cantilevers was fabricated from an SOI with an active layer thickness of  $5.5 \mu\text{m} \pm 0.5 \mu\text{m}$ .  $\text{SiO}_2$  was grown through a wet thermal process ( $1050^\circ\text{C}$ , 1 hour) to a thickness of  $0.52 \mu\text{m}$  resulting in a Si active layer  $5.72 \mu\text{m}$  thick. Layer thicknesses were determined using a profilometer, and measured through imaging in a scanning electron microscope (SEM). Deflection and voltage characterizations were carried out using the bonded die packages described above in which the secondary oxide coating the ground plane electrode was  $1.34 \mu\text{m}$  thick.

### 2.4.1. *Deflection Characterization*

Figure 12 shows a set of cantilevers (upside down) used for characterization and Figure 13 shows a  $1750 \mu\text{m}$  fully released double cantilever beam. Optical defocusing (OD), shown in the inset in Figure 13, was used to characterize beam tip deflection. Deflection measurements taken for beams measuring 500, 1000, 1500, and 2000  $\mu\text{m}$  correlate well with the analytic model (Figure 14), and a COMSOL model used to corroborate results (Figure 15). As described in the model in equation (1), deflection

scales with the square of the length of the beam ( $\delta \propto L^2$ ), and this is supported by the measured data in Figure 14. As the length of the beam doubles from 1000  $\mu\text{m}$  to 2000  $\mu\text{m}$ , the average tip deflection nearly quadruples from 72.5  $\mu\text{m}$  to 293.0  $\mu\text{m}$ . The measured deflections validate both the analytic and COMSOL models.

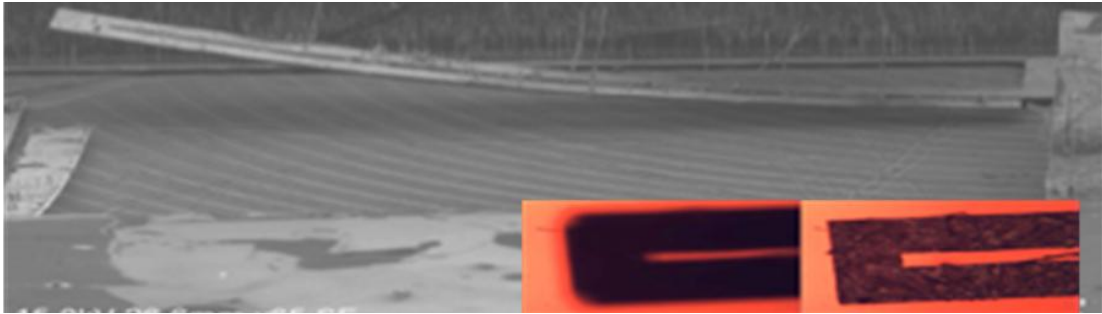


Figure 13: Fully released 1750  $\mu\text{m}$  cantilever zipper actuator. An optical defocusing measurement of beam deflection is shown inset.

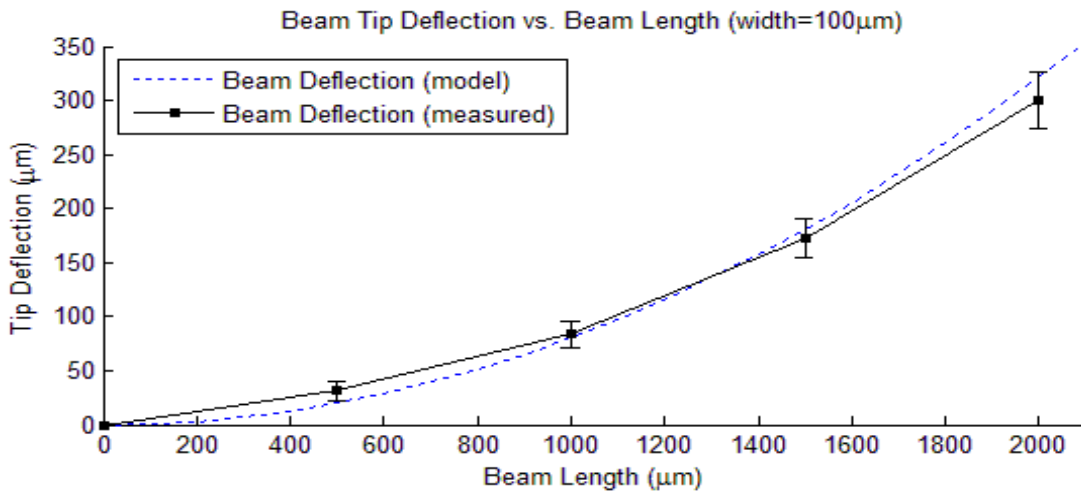


Figure 14: Agreement between analytic model for beam deflection, and actual deflection using optical defocusing.

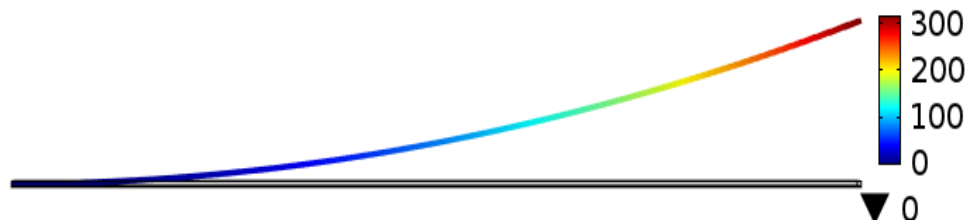


Figure 15: COMSOL model of 2000  $\mu\text{m}$  beam with total deflection of 315  $\mu\text{m}$ , in correlation with analytic and measured values for 2000  $\mu\text{m}$  beam.

#### 2.4.1.1. Stoney's Equation and Residual Stress

Before measuring the film thicknesses and the deflection of the beams, the compressive stress in the SiO<sub>2</sub> was unknown, and preliminary modeling was carried out using an assumed value. Given these pieces of measured data, the oxide film stress can be calculated using what is known as Stoney's equation, which relates the cantilever tip deflection to the internal stress through material and geometric properties of the beam. It is defined as follows:

$$\sigma = \frac{E_s h_s^2}{6\mathfrak{R}(1-\nu_s)h_o} = \frac{\delta E_s h_s^2}{3L^2(1-\nu_s)h_o}. \quad (20)$$

Having found the film thicknesses, we can determine that  $\sigma = 275$  MPa, and can substitute this into the model in place of any assumed values until this point.

#### 2.4.2. Voltage Characterization

A micro-stage with a digital microscope was used in conjunction with a power supply (Agilent E3612A) to ground the lower electrode and apply voltage to the actuator electrode. Two sets of the cantilevers above were tested for pull-in voltage by ramping the voltage from 0 V until pull-in was observed. The average value of  $V_{PI}$  was 135 V with a standard deviation of 4.9 V. This is quite different than the expected value of  $V_{PI}$  from the analytic model of 65.3 V. The variance in  $V_{PI}$  between beams and between the analytic and measured values stems from the fact that the oxide coated electrode die was bonded to the actuator die on the rough unpolished side, and from the other effects outlined in 2.2.1.3. This was done to mitigate the effects of stiction, and to make the actuator more robust in uncontrolled ambient

environments. This will be discussed in more detail later, but the result is a non-periodic average surface roughness (RA measurement using Tencor Proflimeter over 1 cm scan) of 240 nm at the point of intimate contact between the ground electrode and actuator. As discussed above in §2.2.1.3, the model for  $V_{PI}$  presented here does not account for the effects induced by the roughness and the gaps it creates between the mating surfaces. Even so, the standard deviation between beams of 4.9 V is approximately 4% variance and demonstrates that the pull-in voltage is consistent across multiple zipper actuators, and that the discrepancy between the measured voltage and analytically modeled voltage is consistently approximately double. As such, we can determine that the correction factor stemming from the nature of the electrode configuration is approximately 2. As was mentioned earlier, the goal of this work is not to develop a comprehensive model, but rather an innovative electrostatic actuator.

Additionally,  $V_{PI}$  as defined in equation (16) is independent of the length of the beam, and rather is determined by the electrode gap and the cross-sectional dimensions of the beam, which, in the case of the test zipper cantilevers, are the same in each beam. We consider the model for pull-in voltage validated by the experimental results, with an expected variance of a factor of 2 due to the variables unaccounted for by the model.

## 2.5. Design Capabilities of Cantilever Zipper Actuators

Given that the measured deflection for the zipper cantilevers above matched the analytic and numeric models well, and the measured  $V_{PI}$  behaved predictably with respect to the model, we can begin to examine the extreme capabilities of this novel

zipper concept. For the particular 1000  $\mu\text{m}$  zipper cantilever described above (0.52  $\mu\text{m}$  thick  $\text{SiO}_2$ , 5.72  $\mu\text{m}$  thick Si, 30  $\mu\text{m}$  wide) the tip deflection is 72.5  $\mu\text{m}$  on average,  $V_{PI}$  is 135 V on average, the calculated blocking force at the tip is 0.075 mN, and the calculated switching time is 0.23 ms. If we fix the length of the beam at 1000  $\mu\text{m}$ , and vary input parameters such as the thicknesses of the Si and  $\text{SiO}_2$  beam layers, the beam width, and the thickness of the secondary electrode oxide we can begin to see the wide range of deflections, voltages and tip forces that can be achieved, and hence the wide range of applications for this novel technology.

The analytic model works under the assumption that the beam's length is much greater than its width. Hence, in addition to constraining the beam length to 1000  $\mu\text{m}$  we will also constrain the beam width to 100  $\mu\text{m}$  or less. As noted earlier, varying the width of the beam has no effect (to the first order at least) on the deflection and pull-in voltage, but has a linear effect on the tip force: beams twice as wide, have twice the tip force. Moreover, for a fixed beam length,  $V_{PI}$  varies linearly with  $\delta$ . A smaller radius of curvature is necessary for larger deflections, and since  $V_{PI}$  varies with the inverse of  $\mathfrak{R}$ , as the radius of curvature decreases the pull-in voltage increases.

We will introduce an additional metric for determining performance – Safety Factor ( $SF$ ). The two dielectric layers are modeled as two capacitors in series, each dissipating a quantity of  $V_{PI}$  proportional to their individual thicknesses. Given the breakdown voltage of  $\text{SiO}_2$  and the thickness of each oxide layer, the maximum voltage each layer can dissipate before breakdown occurs ( $V_{BD}$ ) can be found, and the



smaller value of the two becomes the limiting factor. We can then define safety factor as follows:

$$SF = \frac{V_{BD}}{V_{PI}}. \quad (21)$$

Demanding a  $SF$  of at least 2, we can begin to model the extreme capabilities of the novel zipper actuators. Varying the four input beam characteristics, we can optimize the zipper actuators to meet a wide range of requirements. Table 2 lists a few designs that demonstrate the extreme capabilities of the zipper actuator. Devices 1 mm long could be fabricated that can achieve greater than 600  $\mu\text{m}$  deflections, pull-in voltages less than 30 V, tip forces greater than 1 mN, and switching times approaching 0.1 ms. Device #3 represents a zipper actuator with moderate performance across all metrics.

**Table 2: Design capabilities of Si/SiO<sub>2</sub> zipper actuators. Cells highlighted green show favorable performance, while cells highlighted yellow show the design tradeoff.**

	Actuator Design Inputs				Model Mechanics Output					Model Voltage Output		
	$L$ ( $\mu\text{m}$ )	$w$ ( $\mu\text{m}$ )	$h_s$ ( $\mu\text{m}$ )	$h_o$ ( $\mu\text{m}$ )	$\delta$ ( $\mu\text{m}$ )	$SR$	$F_b$ ( $\text{mN}$ )	$k$ ( $\text{N/m}$ )	$\tau$ ( $\text{ms}$ )	$h_{o2}$ ( $\mu\text{m}$ )	$V_{PI}$ ( $\text{V}$ )	$SF$
#1	1000	100	2.0	0.25	305.1	0.305	0.013	0.042	0.139	0.30	28.9	2.77
#2	1000	100	2.0	0.60	602.3	0.602	0.034	0.056	0.143	0.57	95.6	2.03
#3	1000	100	5.0	1.23	210.9	0.211	0.168	0.798	0.224	1.09	178.3	2.01
#4	1000	100	10.3	2.50	101.4	0.101	0.703	6.937	0.322	2.20	359.9	2.01
#5	1000	100	20.0	2.14	26.5	0.027	1.096	41.26	0.43	1.39	199.3	2.01

### 2.5.1. Benchmarking

We can now benchmark the performance of the Si/SiO<sub>2</sub> electrostatic zipper actuator against the metallic zipper actuators previously reported by developing an expression for the “electromechanical performance per area” or EPPA. Essentially, it is a figure of merit that will measure the mechanical output achieved for every volt required to

actuate the zipper, normalized to the area it occupies. In this way, performance of actuators of different shapes and sizes can be compared.

We can define the EPPA as follows:

$$\frac{\delta}{L^2} \times \frac{F_b L}{w} \times \frac{1}{V_{PI}} = \frac{\delta F_b}{L w V_{PI}} = \frac{\delta F_b}{A_s V_{PI}}. \quad (22)$$

The first term on the left of (22) is the normalized deflection. Since a longer beam has a greater deflection, and deflection scales with the inverse of length squared, this tells us the deflection per unit length a beam can achieve. The second term on the left is the normalized force. As defined in equation (19), the force is dependent on the beam stiffness, which decreases with length and varies linearly with beam width. Therefore, this term expresses the force efficiency of the beam for a given beam area. Simplifying, the result is the term on the right, which expresses the voltage required to actuate a beam with a given deflection and force, and which occupies a specific area. This can be called the EPPA. While this formula is by no means comprehensive, it eliminates some of the variables that exist between the various electrostatic zipper actuators, and it does provide insight into the overall performance of an actuator. Moreover, since there is no absolute scale the values will be reported normalized to one device. In this way, the EPPA scores will be comparable relative to each other, much the way vibrational mode shapes are related.

**Table 3: Normalized EPPA's for Si\SiO<sub>2</sub> zipper actuators and established zipper actuators**

	<i>Input</i>		<i>Output</i>				<i>Score</i>	
	<i>L</i> ( $\mu\text{m}$ )	<i>w</i> ( $\mu\text{m}$ )	$\delta$ ( $\mu\text{m}$ )	<i>SR</i>	<i>F<sub>b</sub></i> ( <i>mN</i> )	<i>V<sub>PI</sub></i> ( <i>V</i> )	<i>EPPA</i>	<i>Normalized</i>
#1	1000	100	305.14	0.305	0.013	28.9	1.37E-06	4.09
#2	1000	100	602.32	0.602	0.034	95.6	2.14E-06	6.38
#3	1000	100	210.91	0.211	0.168	178.3	1.99E-06	5.92
#4	1000	100	101.41	0.101	0.703	359.9	1.98E-06	5.89
#5	1000	100	26.56	0.027	1.096	199.3	1.46E-06	4.35
#6 [20]	500	5	30	0.060	0.025	200.0	1.5E-06	4.46
#7 [16]	475	90	30.4	0.064	0.009	7.8	8.21E-07	2.44
#8 [15]	1100	471	175	0.159	0.012	70.0	5.79E-08	0.17
#9 [15]	654	645	136	0.207	0.107	110.0	3.14E-07	0.93
#10 [33]	1500	250	306	0.204	0.007	17.0	3.36E-07	1

Compared to established out-of-plane electrostatic zipper actuators, the Si\SiO<sub>2</sub> zipper actuator is nearly twice as productive. Using data reported in earlier publications, the EPPA of established electrostatic zipper actuators was found and tabulated in Table 3 along with the five Si\SiO<sub>2</sub> zipper actuators presented above. Once normalized, the curved electrode presented in [20] weighs in with a relative EPPA score of 4.46, while the thin film metallic zipper actuator in [16] scores a relative EPPA of 2.44. On the other hand, all five Si\SiO<sub>2</sub> zipper actuators presented above scored an EPPA of at least 4, and one as high as 6. Simply, this means that if two devices were fabricated with the same area (i.e. same beam length and width), one a Si\SiO<sub>2</sub> zipper actuator and the other a metallic bimorph zipper actuator, the Si\SiO<sub>2</sub> actuator would outperform the metallic one overall by as much as 6 times. Perhaps its deflection would be 6 times as great, though it would have the same force and actuation voltage. Ultimately, it cannot be determined from EPPA in which metrics the Si\SiO<sub>2</sub> is superior, but on an overall basis, it outperforms its metallic

counterparts. Their closest competitor in terms of efficiency is the curved electrode, which actuates laterally. With respect to out-of-plane actuation, the Si/SiO<sub>2</sub> zipper actuator is at least twice as efficient as its thin film metallic counterparts. This is due in large part to the capability of fabricating actuators that substantially thicker, an aspect made possible through the use of Si/SiO<sub>2</sub> and standard MEMS micromachining processes. For details on the calculations, see Appendix B: EPPA Calculations and Notes.

Though the above benchmarking was insightful and highlighted the major overall improvement offered by Si/SiO<sub>2</sub> zipper actuators, a more traditional benchmarking is presented below as well, evaluating performance for each metric.

The blocking forces capable of the Si/SiO<sub>2</sub> zipper actuator fall between 10<sup>-5</sup> N and slightly greater than 10<sup>-3</sup> while still producing meaningful output in the other metrics. This compares favorably with general electrostatic actuators (zipper or other) whose group average falls at the center between 10<sup>-6</sup> N and 10<sup>-3</sup> N [1]. More specifically, the curved electrode presented in [20] produces a maximum force of 0.025 mN with a stroke ratio of only 0.06 (30 μm deflection from a 500 μm long beam). Si/SiO<sub>2</sub> zipper actuators such as Devices #1 and #2 in Table 3 can output comparable forces with stroke ratios 5 and 10 times that of the curved electrode. The general class of electrostatic metallic bimorph zipper actuators has total beam thicknesses that are much thinner than what can be achieved in this Si/SiO<sub>2</sub> zipper actuator, limiting their force output. The electrostatic zipper actuators in [13] [15] [16] have total beam thicknesses of 1 μm, 2 μm and 2.5 μm respectively, limited by the fact that they are fabricated from metal. These electrostatic zipper devices would

not be applicable in cases where high tip force is necessary by virtue of the simple fact that they cannot be fabricated to attain high force. Si/SiO<sub>2</sub> zipper actuators, such as Devices #4 and #5 can achieve relatively high forces, and could be of use in applications like manipulating a haptic or tactile display such as a Braille reader, or other reprogrammable arrays.

In terms of deflection, comparison will be made by means of the stroke ratio of each actuator. As noted above, the curved electrode achieves a stroke ratio of 0.06, while the out-of-plane metallic zipper actuators in [15], [16], [33] achieve stroke ratios of 0.16, 0.06 [15] and 0.20 respectively with actuation voltages of 7.8 V, 70 V and 17 V respectively. On the other hand, Si/SiO<sub>2</sub> zipper actuators can achieve stroke ratios over 0.30 with actuation voltages as low as 28.9 V, or stroke ratios over 0.60 with actuation voltages under 100 V.

Finally, the ability to fabricate thicker actuators from Si/SiO<sub>2</sub> result in stiffer beams (as evidenced by greater forces) that can achieve sub-millisecond switching times. This makes them extremely appropriate for use in optical switching and relays.

## 2.6. Summary

An in depth analytic model was developed to explore the performance of electrostatic zipper actuators fabricated from silicon and silicon dioxide. Expressions for beam deflection, tip force, switching time and actuation voltage were presented. Additionally, a numeric model was introduced in parallel to the analytic model, providing a second method of determining deflection and tip force. More importantly though, it provided a numeric and visual expression of the resonant frequencies and mode shapes, from which the switching time could also be calculated.

Next the fabrication process was detailed, and fabricated devices were characterized. Optical deflection was used to determine tip deflection, and the pull-in voltage was found as well. The results validated both the analytic and numeric models, to the extent that the models were used to investigate the extreme capabilities of the Si/SiO<sub>2</sub> zipper actuators.

The results were benchmarked against established thin film metallic zipper actuators, through a novel benchmarking criterion, electromechanical productivity per area, EPPA. Si/SiO<sub>2</sub> zipper actuators were at least twice as efficient as already established out-of-plane electrostatic zipper technology. In terms of force output, they fall within the upper range of all electrostatic actuators (zipper type or other), and provide higher tip forces than other out-of-plane electrostatic zipper actuators. Similarly, Si/SiO<sub>2</sub> zipper actuators achieve greater deflection per area occupied (stroke ratio) than other zipper actuators, but at comparable actuation voltages.

## Chapter 3: Electrostatic Zipper Actuators: Microstage Actuators

### 3.1. Introduction

In Chapter 2: a cantilever beam electrostatic zipper actuator was developed. However, a natural manifestation of out-of-plane actuation would be to raise and lower a load through the actuators motion. Since cantilever beams end in a tip, and in the case of zipper actuators, a sloped tip whose actuation trajectory is an arch, they are ill-suited for this purpose. Vertical motion on the microscale with negligible lateral shift is valuable currently in the realm of medical microoptics, particularly endoscopic microscopes that can image cells and live tissue [2]. However, other uses yet to be developed would undoubtedly benefit from this capability. As outlined in §1.1.2, electrothermal transduction and electrostatic comb finger actuators have been developed that meet this need to an extent. However, electrothermal transduction requires continuous power input, reaches high operating temperatures and, due to its nature, possesses a slow response time. Similarly, electrostatic comb drive actuators are limited by low forces, large footprints and their deflection is constrained by the thickness of the actuator itself. An actuation scheme that could achieve high deflection through a vertical path, output high forces, possess a fast switching time, consume low power or require a low actuation voltage, all in a small footprint, would overcome many of the limitations facing out-of-plane actuation currently.

In this vein, a geometry was sought that could make use of the capabilities of the Si/SiO<sub>2</sub> zipper actuator in realizing out-of-plane vertical motion. The immediate design goal was to achieve large deflections while minimizing the actuator footprint.

From that point, parameters could be optimized to increase force and decrease pull-in voltage.

### *3.1.1. Spiral Design – Geometric Challenge: “Birds Nest Phenomenon”*

Since actuator tip deflection scales with the square of the length, the natural progression was to fabricate spiral designs capable of packing a long total length into a small footprint. After fabrication of various spiral geometries, it became immediately clear that there was a fundamental issue with the spiral concept. Unlike the actuators in [23] where spiral actuators achieve a continuously rising slope, the actuators fabricated here achieved a maximum deflection exactly  $180^\circ$  from the anchor point, no matter the shape (smooth spiral or square spiral) or configuration of the actuator beam. This “bird-nest” phenomenon is shown below in Figure 16(a) and (b), in SEM images of various spiral actuators, and validated by a COMSOL model of a similar spiral actuator in Figure 16(c). The cause behind the “bird-nest” is best illustrated by Figure 16(d). Each successive “leg” of the continuous beam has initial conditions that match the tip conditions of the end of the leg to which it is attached. Hence, the third leg, positioned  $180^\circ$  from the anchor of the beam has an initial slope *down* towards the base that is the result of the initial conditions of the previous two legs. This idea can be applied to a spiral, which is essentially an infinite number of short “legs”, and can be used to explain why the spiral’s maximum deflection occurs  $180^\circ$  from the base, no matter the configuration of the beams. In [23], the spiral actuators are given a deflection by mechanically deforming the spiral beam at high heat, a process that induces a natural torque in the spiral, so that as it rises continuously, its torque warps the beam, correcting its otherwise natural downward



slope that would occur after  $180^\circ$ . The fabrication of Si/SiO<sub>2</sub> actuators uses the natural stress of the SiO<sub>2</sub> to provide beam deflection. Hence, no beam torque exists to counteract the natural downward slope as the spiral progresses.

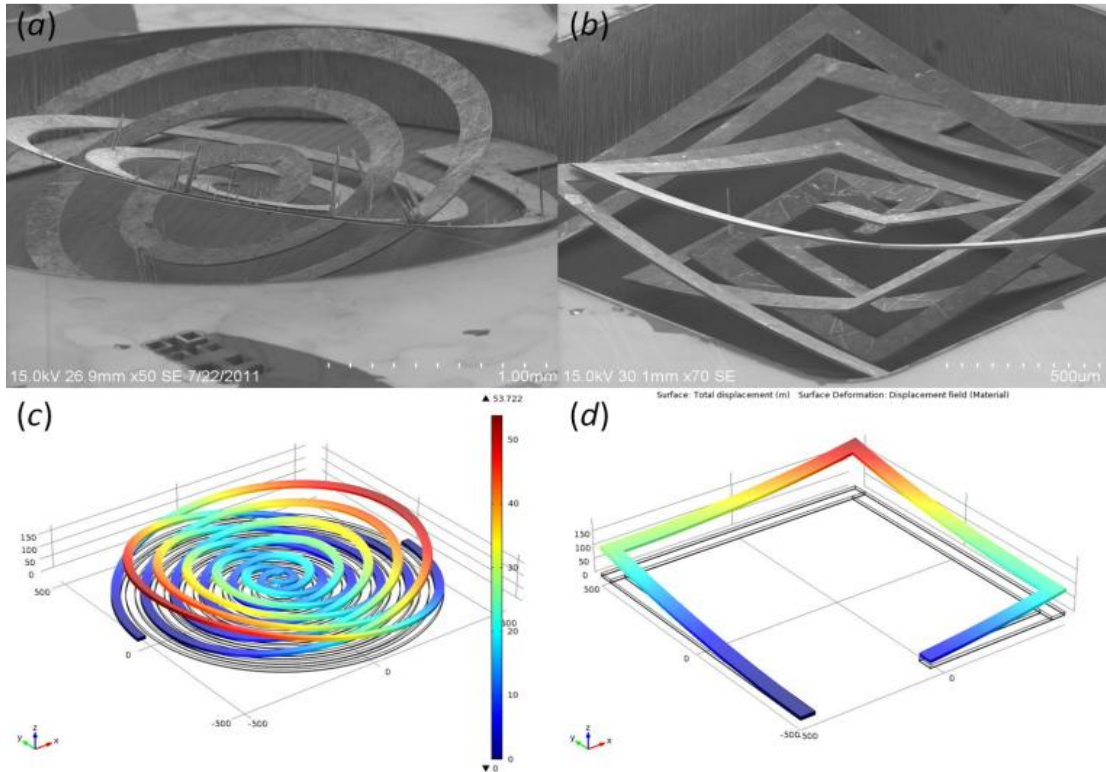


**Figure 16: (a) Round spiral (b) square spiral and (c-d) COMSOL spirals, all exhibiting "bird-nest" phenomena. (d) COMSOL model illustrating the theory behind the bird-nest phenomenon.**

See Appendix C: Gallery of Spiral Geometries and other Images for a gallery of COMSOL geometries that attempted to solve the birds nest issue.

### 3.1.2. Solution to the "Birds Nest" – Microstage Actuators

In order to achieve large deflections in a constrained footprint, serpentine actuators are fabricated in a modified process involving selective removal of oxide from portions of the beam. While a more complex fabrication process is required the resulting designs are capable of achieving exceptionally large deflections within a compact space. Moreover, the geometry lends itself to a symmetric design creating

stability and culminating in a flat center area ideal for affixing a load. Finally, due to the symmetry of the design, the flat center stage traverses a vertical trajectory during actuation.

A segment of the profile of the “microstage” actuator can be seen in Figure 17. The first leg consists of an actuated segment of length  $L_c$  and a linear segment of length  $L_{max} - L_c$ , where  $L_{max}$  is the total length of the beam. The actuated segment (red) is a Si/SiO<sub>2</sub> zipper actuator of the type presented above, followed by a linear segment (blue) of only Si whose slope and deflection amplification are defined by the slope at the end of the actuated segment. The second leg consists of an actuated segment of length  $2L_c$  followed by a linear segment of length  $L_{max} - 2L_c$ . By doubling the length of the actuated segment in the second leg, the actuator continues to grow in total deflection for each new segment added.

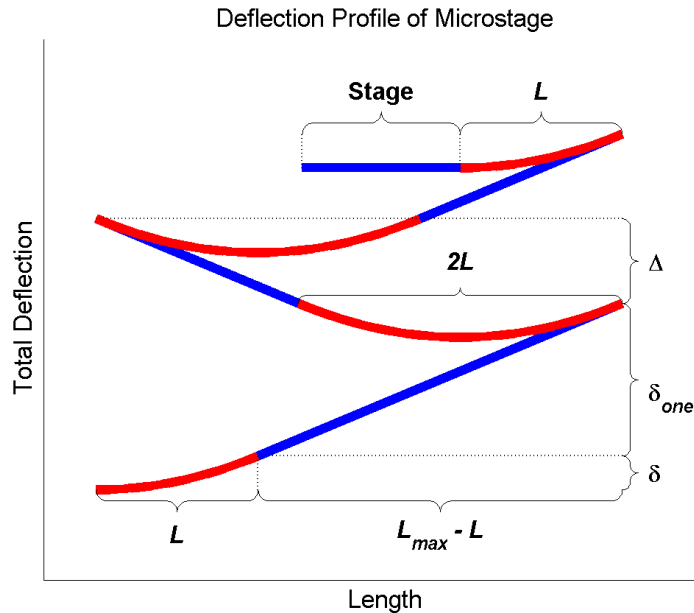


**Figure 17: Profile of the microstage actuator, exhibiting the patterned oxide segments that enable large deflections.**

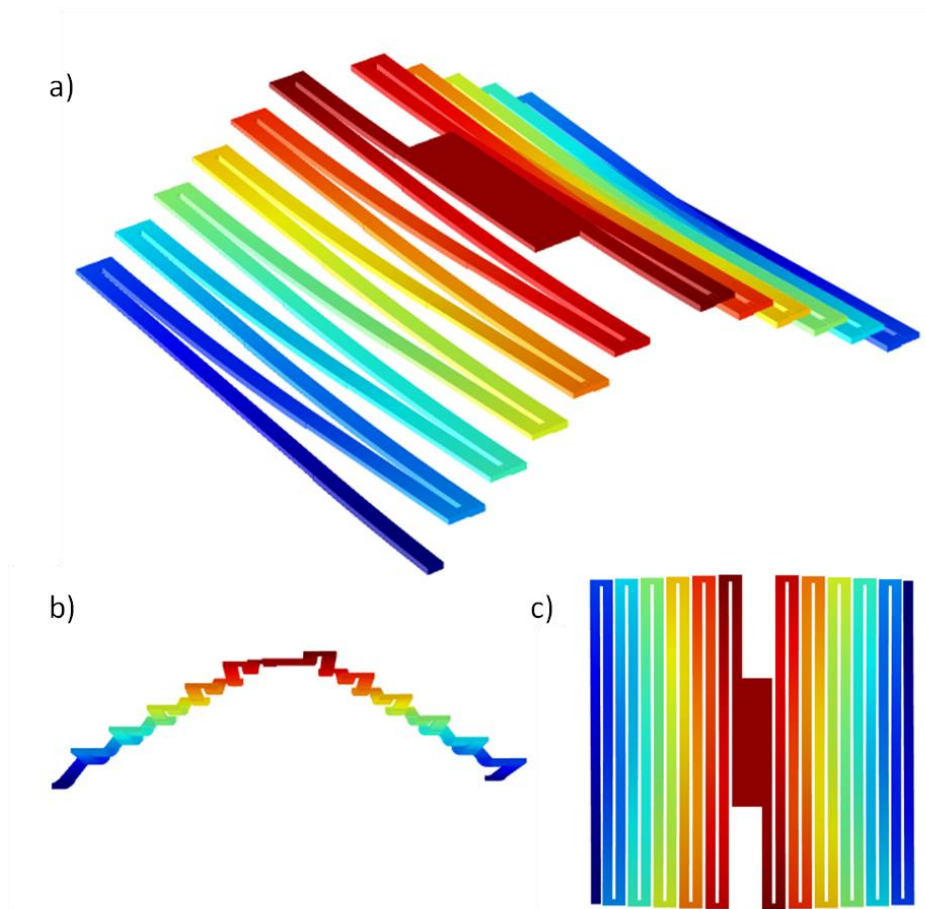


**Figure 18: a) Model of a microstage actuator. Careful examination shows that each beam has a curved segment and then a linear segment. (b) Side view and (c) top view.**

### 3.2. Theory and Modeling

In its most elementary sense, the microstage can be modeled as two parallel springs which meet in the center, each of which is a set of individual cantilever beams connected in series (Figure 18). However, whereas the simple zipper described above was modeled as a fixed-free beam, the individual beams in the microstage are fixed-guided beams. In terms of modeling the total displacement at the center stage, this plays no role, but with regards to modeling  $k$ ,  $V_{PI}$ , and other metrics, the distinction is highly relevant.

### 3.2.1. Analytic Model – MATLAB

#### 3.2.1.1. Adaptation of Cantilever Beam Deflection Model for Stage Deflection

We begin the deflection model of the microstage using the same method as was employed for a single cantilever. Noting that  $L_c$  is the length of the oxide covered segment of the beam, we define  $L_{max}$  as the total length of one beam in the microstage. Using equation (1) above we model the tip deflection of a beam of length  $L_c$ , determine its radius of curvature using equation (17), calculate the slope ( $m$ ) of the beam at length  $L_c$ , and project that slope through the remaining length up to  $L_{max}$ , as follows:

$$m = -(\mathfrak{R}^2 - L^2)^{\left(-\frac{1}{2}\right)} \quad (23)$$

which is derived from the equation of the circle defined by  $\mathfrak{R}$ . We can now define  $\delta_{one}$ , the tip deflection of one beam of the microstage as

$$\delta_{one} = m(L_{max} - L_c) + \delta. \quad (24)$$

At this point, the path of the microstage beam takes a  $180^\circ$  turn beginning its serpentine path. The second beam can be modeled in a similar fashion defining the tip deflection at the end of the second beam as  $\delta_{two}$ . This allows us to define the gain ( $\Delta$ ) in deflection between the tips of the first and second beam as

$$\Delta = \delta_{two} - \delta_{one}. \quad (25)$$

Choosing the number of serpentine segments ( $n$ ) in each half of the microstage we can model the final deflection of the center stage,  $\delta_{stage}$ , as follows:

$$\delta_{stage} = \delta_{one} + (n-1)\Delta - \delta. \quad (26)$$

Recall that  $\delta$  is the tip deflection of the curved segment of the first beam. The initial deflection,  $\delta$ , is subtracted from equation (26), because it ultimately doesn't contribute to the total deflection. In order to return the slope of the last serpentine beam to zero, the final beam segment, beam  $n+1$ , is required to have an equal and opposite slope and deflection as the initial curved segment. Hence, whatever gain in deflection is achieved by the initial curved segment is lost by the final curved segment. Rather, the initial deflection serves to define the slope of all successive segments, thus defining the total deflection in conjunction with the number of segments,  $n$ . The profile of the model is presented in Figure 17. The axes are not to scale so as to be able to visualize the individual components. Blue lines represent beam segments where the oxide has been removed from the bimorph, while red lines represent beam segments containing both oxide and silicon. Hence, all red segments are curved, and all blue segments are linear.

### 3.2.1.2. Mechanical Force and Effective Spring Constant

As noted in §3.2, each individual beam of the microstage can be modeled as a clamped-guided beam, with a spring constant  $k_{beam}$ , where

$$k_{beam} = \frac{12EI}{L_{max}^3}. \quad (27)$$

The serpentine beams are connected in series forming one set of  $n$  beams, and each set is connected in parallel through the stage in the center. Hence, the effective spring constant for the entire microstage,  $k_{eff}$ , can be found as follows:

$$\frac{1}{k_{eff}} = \frac{1}{k_1} + \frac{1}{k_2} + \dots + \frac{1}{k_n}, \quad (28)$$

but since each beam segment of the serpentine is identical, the spring constant for each segment is the same ( $k_1=k_2$ ), so that

$$k_{eff} = \frac{2k_{beam}}{n} = \frac{24EI}{nL_{max}^3}. \quad (29)$$

A logical check validates this expression. As  $n$  grows, the effective spring constant of the microstage will decrease, which is congruent with intuition that a longer beam is more flexible and less stiff. Moreover, as the number of beams in the serpentine decreases, the effective spring constant increases as the microstage becomes more rigid.

#### 3.2.1.3. Electrostatic Force and Pull-In Voltage

The pull-in voltage ( $V_{PI}$ ) for the microstage is modeled using the same method employed for simple beams. However, since the spring constant for the microstage is different the resultant equation for  $V_{PI}$  changes slightly.

Given  $k_{eff}$ , we can now model  $V_{PI}$ , using the same method as before, with the result that

$$V_{PI} = \sqrt{\frac{6EIg}{n\epsilon w \mathfrak{R}^2}}. \quad (30)$$

Again, a quick logical check validates this expression. As  $n$  decreases, the compliance of the microstage decreases, necessitating a higher pull-in voltage to achieve actuation than a simple beam requires.

#### 3.2.1.4. Stage Force and Switching Time

Finally we can define the mechanical switching time ( $\tau$ ) and the blocking force ( $F_b$ ).

We model the microstage as a fixed-fixed beam, whose beams have a non-negligible

mass, with a concentrated mass in the center. This is both accurate and useful for future calculations that might involve fixing a load to the center stage. Therefore  $\tau$  can be found as follows [34]:

$$\tau = 2\pi \sqrt{\frac{m_{stage} + 0.375m_{beam}}{k_{eff}}}. \quad (31)$$

Similarly, we define the blocking force as above for a simple beam and find,

$$F_b = k_{eff} \delta_{stage}. \quad (32)$$

### 3.2.2. Numeric Model – COMSOL

COMSOL was used to numerically model the performance of the microstage using the same methodology outlined in §2.2.2. The practical difference was the step in which the geometry of the actuator was created, since the microstage clearly has a more complex geometry than a simple beam.

#### 3.2.2.1. Microstage Deflection

The geometry is drawn in the  $xy$ -plane and then extruded in the positive  $z$ -direction a distance of  $h_s$  and in the negative  $z$ -direction a distance of  $h_o$ , in order to provide the appropriate thickness to the beams. An image of the geometry before extrusion is shown in Figure 19 and after extrusion and material designation in Figure 20. Note the blue corresponding to oxide coated segments and red corresponding to silicon beams only. Modeling proceeds with the structural mechanics module in a fashion similar to that outlined for cantilever beams, except that the fixed constraint is now applied to the anchor points on each side of the actuator, anchoring those points in space.

Upon solving, the model outputs the deflected microstage based on the input parameters, and serves as a FEM based method for modeling the deflection of the zipper inspired microstage in parallel to the analytic method.

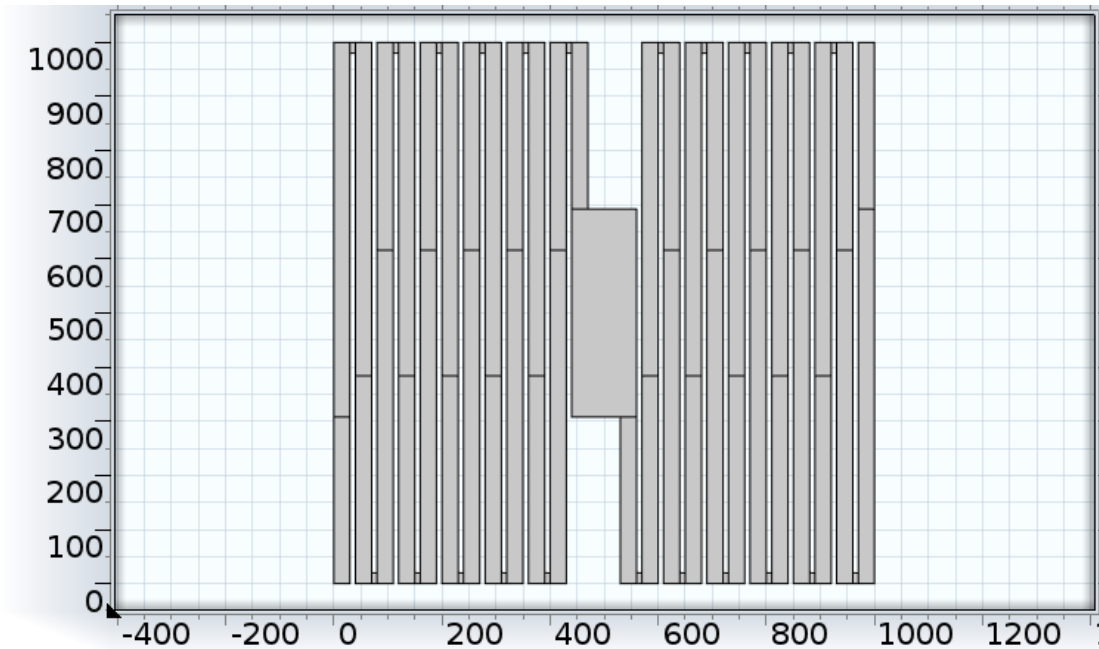


**Figure 19: Microstage geometry in 2D drawn in COMSOL**

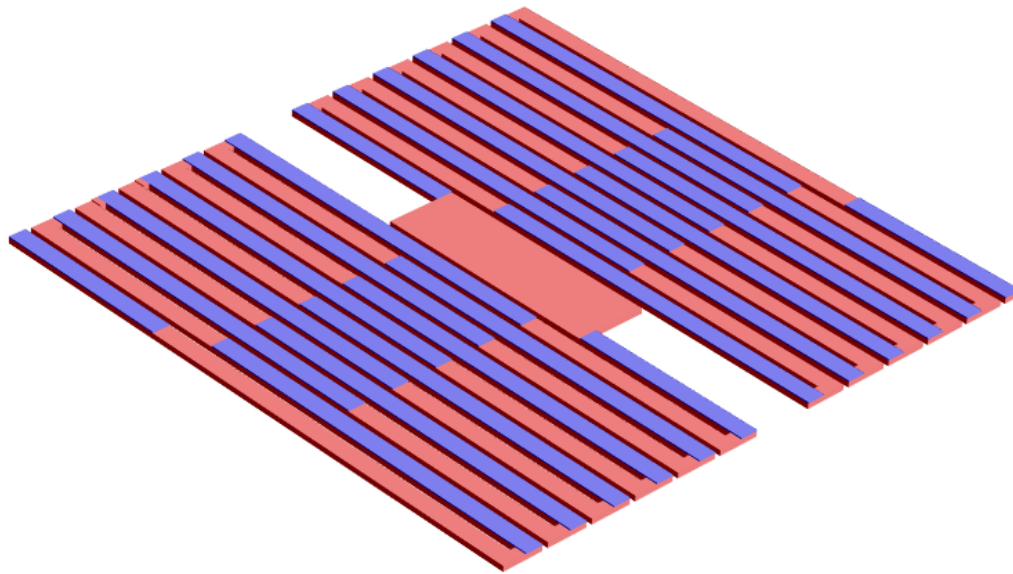


**Figure 20: After the geometry is drawn, it is extruded into the 3rd dimension by the thickness of the beams, and materials are assigned.**



#### 3.2.2.2. Stage Force and Effective Spring Constant

In a manner analogous to that presented in §2.2.2.2, a variable,  $F_{in}$ , is created to represent force, and is applied to the center of the stage, acting towards the ground plane. Using the solvers parametric sweep function, the force variable was ramped from 0  $\mu\text{N}$  to 10  $\mu\text{N}$  in 1  $\mu\text{N}$  increments, and the force – deflection curve was plotted where the slope of the line is the stiffness of the beam.

#### 3.2.2.3. Dynamic Modeling

Similarly, FEM allows us to model the dynamic response of the microstage, particularly its resonant frequencies and corresponding mode shapes. Using the *Eigenfrequency* study node in COMSOL, we can specify the number of frequencies to find, and output the mode shapes of the microstage actuators. From these values, we can determine the time constant of the devices numerically in addition to the analytic values above.

### 3.3. Fabrication of Microstage Zipper Actuators

Fabrication of the microstage actuators is more complex than the simple cantilever beams outlined above, though still a relatively straightforward process employing classic MEMS processing. A general overview of the process is presented here, while the complete details, etch recipes and procedures can be found in the Appendix A: Recipes and SOPs.

#### 3.3.1. *Microstage Actuator Fabrication*

Illustrated in Figure 21 the process begins by oxidizing a p-type (100) SOI. In this process, thermal oxide is grown from the Si active layer (1050C, wet growth). Similar

to the simple cantilever beam above, this oxide layer will serve as the stress inducer for the bimorph and the dielectric to enable electrostatic actuation. Photoresist (AZ4620) is spin-coated atop the oxide, and is photolithographically patterned to serve as a mask for beam patterning. Next the oxide is etched using RIE (Figure 21(b)) to begin definition of the selectively oxidized Si/SiO<sub>2</sub> bimorph, and completely defined by DRIE of the Si active layer in the next step (Figure 21(c) and Figure 22).

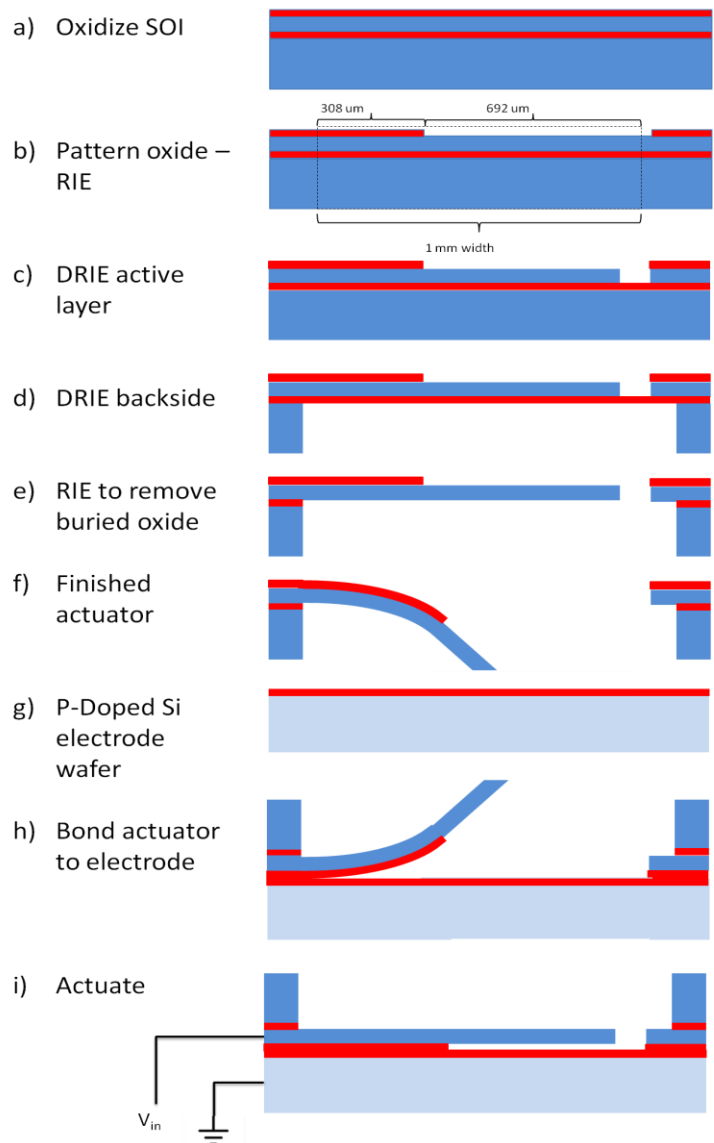


**Figure 21: Microstage fabrication process.**

Photoresist is spun on a carrier wafer, and is used to loosely bond the frontside of the SOI to the carrier wafer. The carrier wafer serves to ensure that as the backside etch approaches the BOX, the thinned wafer does not break apart in the DRIE. Additionally, as the backside of the SOI thins, the patterned actuators on the frontside will naturally deflect upwards due stress and break through the thin backside layer. If this occurs before the backside layer can be fully removed in the DRIE, or before the BOX is removed in the next step, the result will be actuators that have large chunks of backside material clinging to them. Therefore, the photoresist is used to bond the carrier wafer, but also to hold the frontside actuators in place throughout the backside etch process.

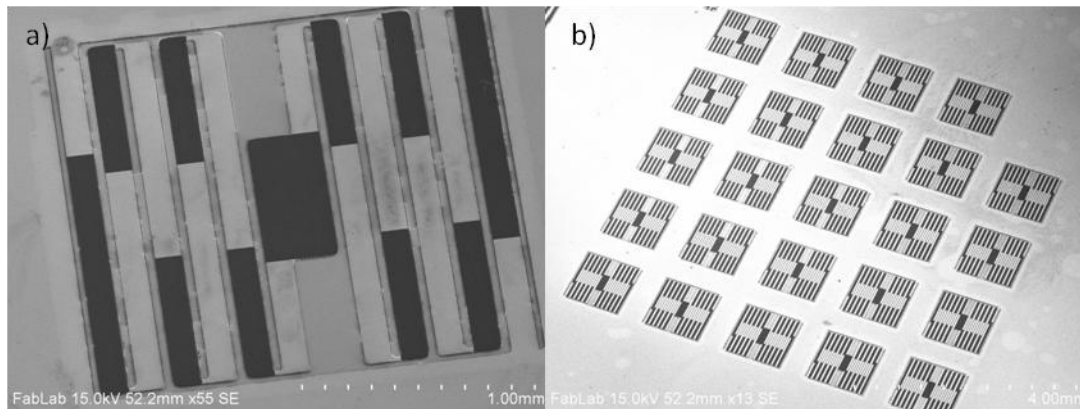


**Figure 22: Frontside of the SOI, after frontside patterning has been completed. The dark color is the silicon of the beams where the oxide has been selectively removed. Photoresist will be spun over this pattern and then bonded face down onto a carrier wafer to begin backside processing. Underneath the patterned beams lie the BOX and the backside of the wafer. (a) A single actuator, and (b) an array of actuators.**

The backside of the SOI is DRIE etched, using the same negative etch recipe that was used for cantilever fabrication, stopping on the  $2\mu\text{m}$  buried oxide layer (BOX) (Figure 21(d)) and the BOX is etched using RIE (Figure 21(e)). The wafer is diced using a Microautomation Dicing Saw into  $1\text{ cm}^2$  dies, each containing an array of actuators. After dicing the carrier wafer is soaked overnight in an acetone bath to

dissolve the photoresist between the actuators and the carrier wafer, and to fully release the actuator beams. An SEM image of a fully release 1 mm actuator can be seen in Figure 23(a). Figure 23 (b-c) show the selective patterning of the oxide on the silicon beams. Figure 23 (b) is the frontside of the 1 mm actuator in Figure 23 (a). It can be seen that each beam in the serpentine is composed of two differently shaded segments. The darker portion of the beam is the selectively patterned  $\text{SiO}_2$ , and the lighter segment of each beam is the Si portion that underlies the oxide. Figure 23 (c-d) show a close up view of the section of the beam where the oxide was removed.

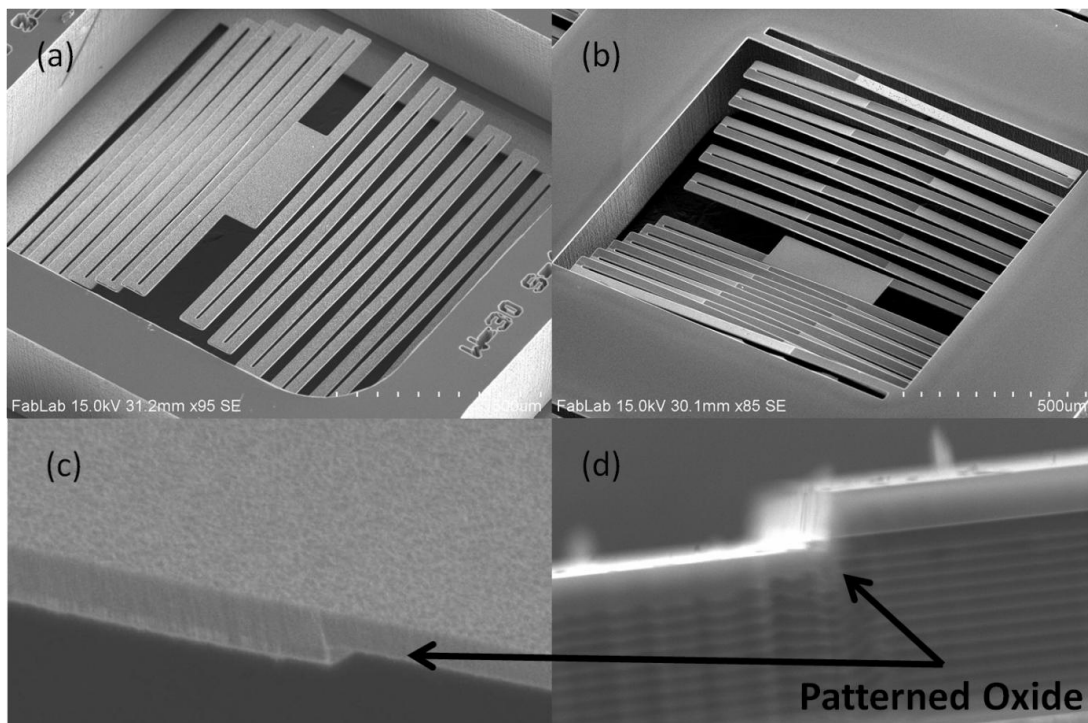


**Figure 23: (a) A 1 mm actuator after fabrication and release from the carrier wafer. (b) The same 1mm actuator turned upside down. The selective patterning of the oxide is visible. (c-d) Close up view of selective oxide patterning.**

### 3.3.2. Other Topologies Enabled Through Selective Oxide Patterning

Though the microstage provided the best method for achieving large vertical deflections, the concept of patterned oxide provided a novel concept from which

other topologies could be investigated. Moreover, though the design here was constrained to a 1 mm x 1 mm footprint, earlier fabrication runs included geometries with footprints both smaller and larger than that, simply for the sake of investigation.

Figure 24 - Figure 29 show a small sample of some of the designs.

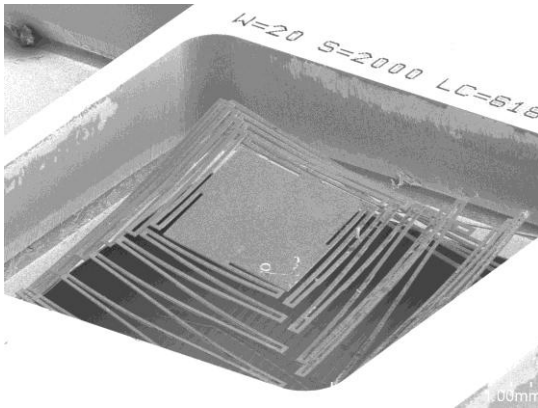


**Figure 24: A damaged quad-flexure microstage.**

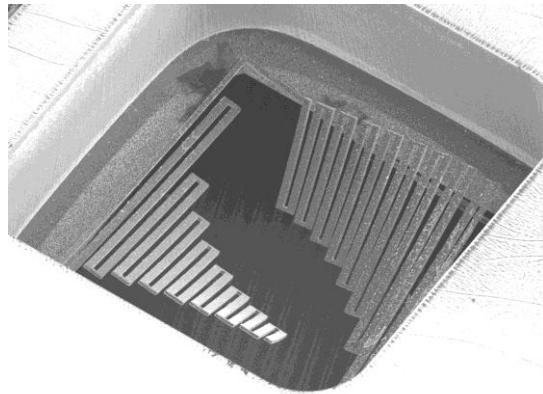


**Figure 25: A precursor to the microstage, tip deflection is 300  $\mu\text{m}$ .**

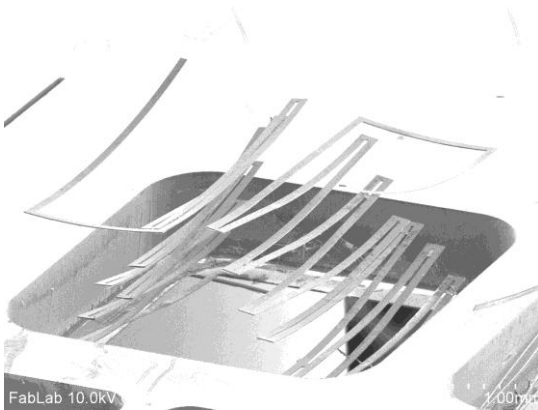


**Figure 26: An odd design, total deflection is greater than 1mm.**

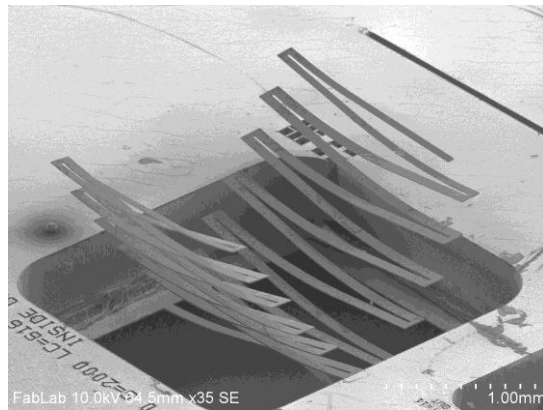


**Figure 27: "Inverted" microstage, anchored at the center.**

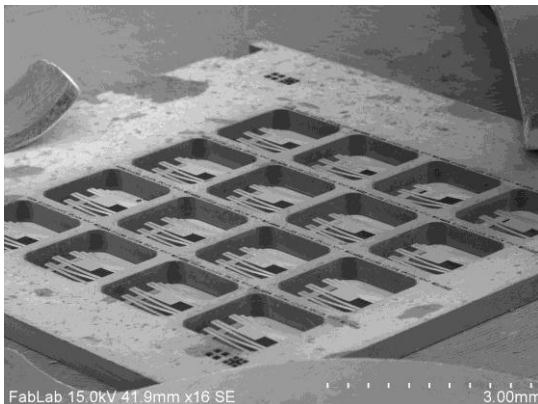


**Figure 28: A 4x4 array of 1.2 mm microstages.**

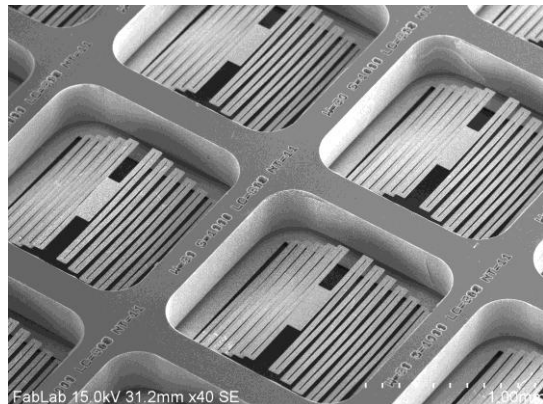


**Figure 29: Close-up of 1mm microstage array.**

### 3.3.3. *Electrode Fabrication*

Unlike the cantilever zipper beams which could, in theory, be actuated on an unshielded electrode (see end of §2.2.1.3), the microstage features beams whose oxide layer has been selectively patterned, leaving silicon exposed in segments of the underside of the beam. Therefore, a shielded electrode is required to actuate the microstage, to prevent electrical shorting between the two silicon electrodes. However, there are two concerns when dealing with electrostatic actuators with large surface areas, such as the microstage, that were less of a concern with simple cantilever beams. The first, known as stiction, occurs when some force (surface tension, possibly due to humidity and moisture between surfaces, Van der Waals, etc.) greater than the restoring force of the actuator, causes the actuator to remain “stuck” to the ground plane, even after the voltage bias and electrostatic force has been removed. Given that the microstage has a much larger surface area that comes in contact with the ground plane electrode surface, the potential for stiction is much greater. The second, known as charging, is the result of residual charge in the dielectric interface as explained at the end of §2.2.1.3.

Developing an electrode scheme that mitigated these two concerns was the primary driving force behind what is outlined in the next two sub-sections.

#### 3.3.3.1. *Patterned Silicon Electrode*

One method of achieving this was to use a patterned unshielded electrode, aligned to the actuator beams. Since the microstages feature discontinuous oxide, the electrode is patterned to match the locations of oxide on the underside of the Si beams (Figure 30). Fabrication begins with a P-doped Si wafer (.001-.005  $\Omega$ -cm), which is etched

via DRIE to a depth of  $\sim 50\mu\text{m}$ . Air has a breakdown voltage of  $3\text{ V}/\mu\text{m}$ . Hence, in order for it to prevent shorting between the exposed Si of the actuator beams, and the Si of the electrode, an air gap of at least  $100\mu\text{m}$  was desired. Figure 30 shows an SEM of an electrode patterned as described above. In order to actuate a device, the actuator must be aligned to the electrode, matching the selectively patterned oxide segments of the actuator to the protruding Si electrode.

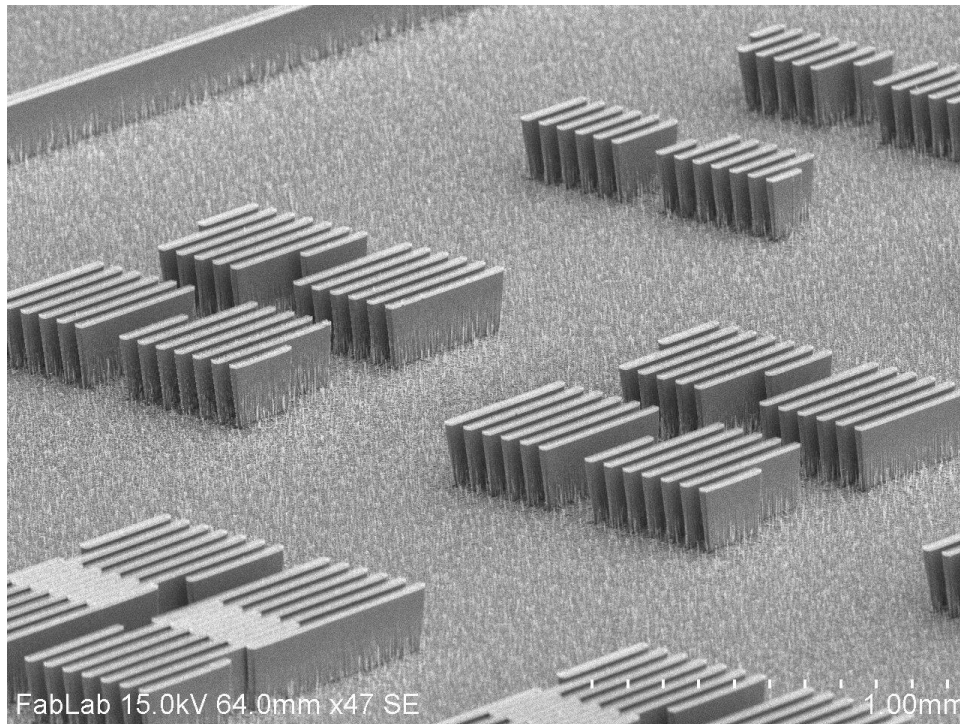


**Figure 30: Patterned silicon electrode wafer. The oxide covered segments of an array of actuators would be aligned to the protruding silicon segments shown here.**

This was achieved using a vacuum chuck and micropositioner in conjunction with a digital microscope and microstage. The electrode wafer was positioned on the lower, movable chuck of the microstage, while the actuator wafer was held in place by the vacuum of the micropositioner chuck. The upper chuck was fabricated in-house from 1 cm thick polycarbonate sheets, so as to provide a flat rigid surface and clear medium through which the microscope could be used to align the actuator to the

electrode. The micropositioner was used to move the actuator die into position, and then lower the die until it came into contact with the underlying electrode layer. In Figure 31, the patterned electrodes are visible underneath the zipper beams.

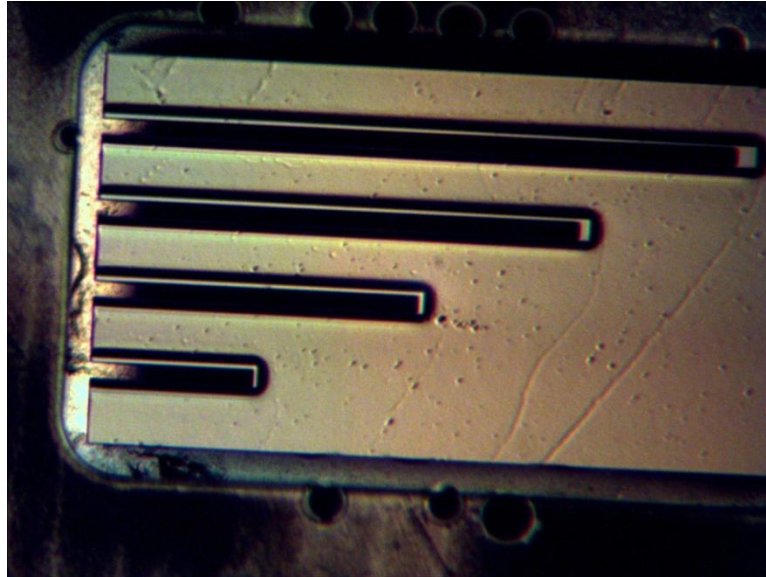


**Figure 31: A microscope image of four cantilever beams almost aligned to the underlying patterned electrode. The white of the underlying electrode can just be seen protruding from the upper edge of the beams.**

This electrode scheme would reduce the effects of charging, since only one dielectric layer is present, and would minimize the likelihood of stiction, since only small portions of the total microstage actuator area come into contact with the electrode surface. Ultimately, this scheme was unsuccessful. Though the electrodes were patterned to allow for some misalignment with the actuators, 5  $\mu\text{m}$  tolerance was required in order to achieve pull-in, a challenging feat using only a microstage and microscope. Additionally, each actuator die contained an array of actuators, and in many cases, the angular misalignment between the electrode and the actuators resulted in complete or partial misalignment for some or all of the actuators in the array. As such, it was not uncommon to achieve pull-in for one or two actuators in an array or for  $V_{PI}$  to rise to the point included in the safety factor (SF) and for the entire



array to short before actuation could be achieved. Moreover, the mechanical pressure used to bring the actuators and underlying electrode into contact also led to variations in the air gap between the actuator and electrode, resulting in scattered  $V_{PI}$  measurements in the cases when alignment was sufficient to achieve actuation. Figure 32 shows eight different  $V_{PI}$  measurements for 1 mm microstage actuators taken over the course of a few days. For each test, the mechanism and conditions for alignment and actuation were the same.

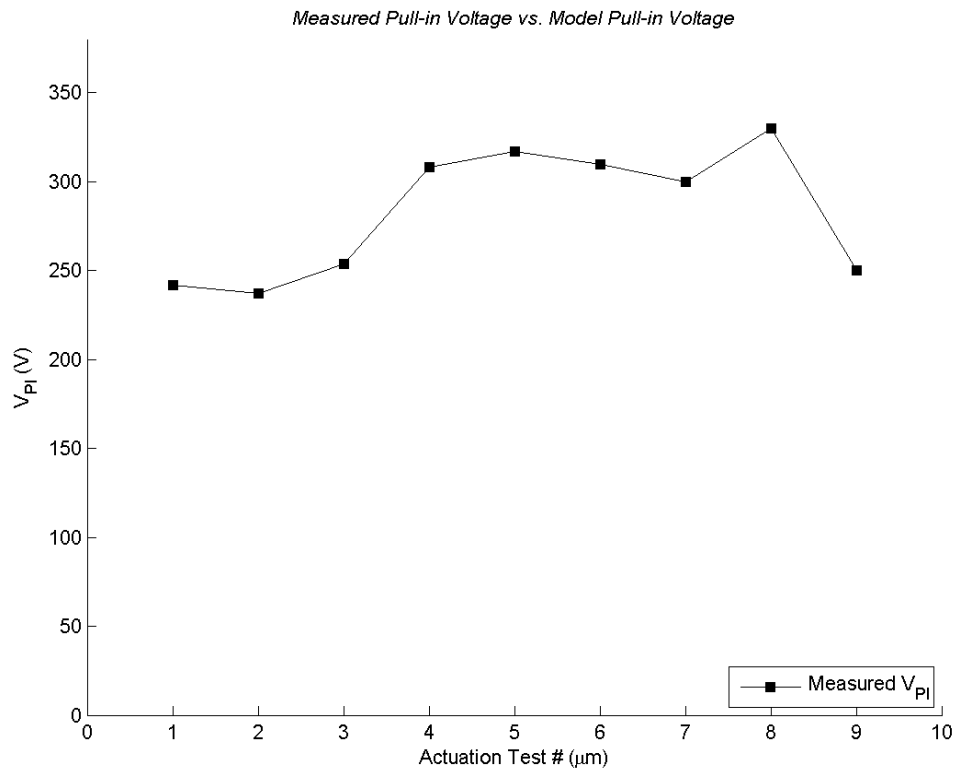


**Figure 32: Pull-in voltage measurements for 1 mm microstages on patterned electrode.**

Though actuation was achieved, the lack of flexibility in alignment and inconsistent  $V_{PI}$  results between actuators necessitated an actuation scheme that eliminated the need for alignment between the actuator and electrode. The ideal would be an integrated fabrication process in which the electrode and actuator were

patterned together to ensure perfect alignment, but the time and cost required to develop such a process were beyond the scope of this work.

#### 3.3.3.2. Rough Silicon Dioxide Coated Electrode

A continuous electrode scheme was sought to eliminate the need for alignment. Initially, the atomically smooth frontside of the oxide coated wafer was used as the electrode surface, and indeed, a release delay was observed as some actuators within an array lagged in their release upon the removal of the voltage. It was hypothesized that the stiction was due to either the undefined charge state between the dielectrics, or to true stiction (humidity, surface forces) between the large surface area of the actuator and electrode. Careful observation showed that when the voltage bias was removed and the actuator was expected to release, the large flat center stage remained stuck to the electrode, while all the serpentine beams released. This observation supported the theory that the lag in release was due to stiction rather than undefined charge between the dielectrics.

Therefore, rather than using the atomically smooth polished side of the wafer as the electrode, the rough unpolished side was used. As discussed in §2.4.1.1, the result is an electrode with a non-periodic average surface roughness (RA measurement using Tencor Proflimeter over 1 cm scan) of 240 nm at the point of intimate contact between the ground electrode and actuator. And, as discussed in §2.2.1.3, this had an unknown and adverse, though consistent effect on the voltage required for actuation.

#### *3.3.4. Packaging and Bonding of Microstage Actuator to Electrode*

Finally, the oxide coated electrode wafer was diced into 1 cm x 1 cm squares, and were manually clamped to a 1 cm x 1 cm actuator die. Quick setting epoxy was coated along the vertical edges of the die stack to create a single die package. The epoxy shrinks as it hardens, thereby enhancing the intimate contact between the actuator and electrode die. Additionally, the epoxy serves as an insulator, ensuring that there is no fringing or shorting between the two electrode layers at the edges of the die package.

#### *3.3.5. Integrated Circuit Board and Die Packages for Testing*

An IC board, shown in Figure 33(a) was fabricated with a simple manual “kill-switch” and a transistor-to-transistor logic (TTL) switch, to which a function generator could be connected to control actuation. The 1 cm<sup>2</sup> die packages (containing the array of 24 1mm actuators characterized above) were packaged in a dual inline package (DIP) as shown in Figure 33(b-c). Silver paste was used to bond the die package to the ground plane of the DIP. This scheme allows for the creation of numerous robust actuator array packages that can be easily inserted into the circuit board, tested and swapped for another package.

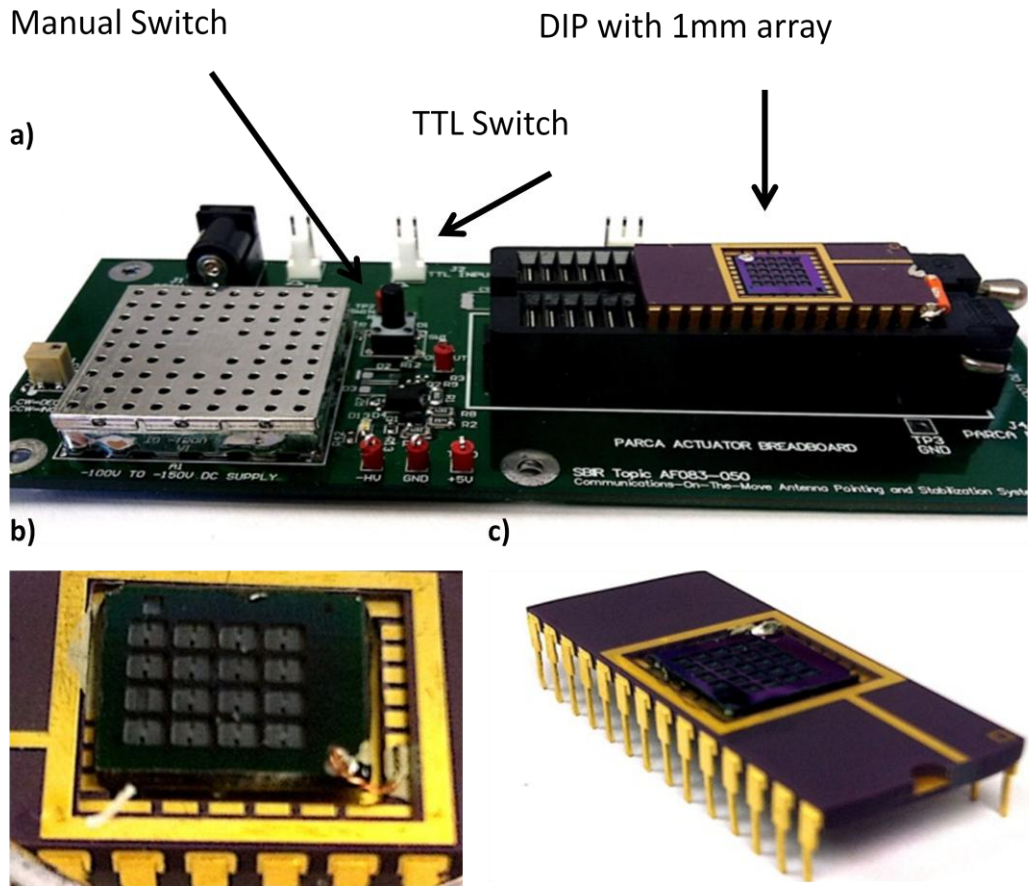


Figure 33: (a) IC board with DIP port for actuator package, TTL switch, and manual switch. (b) A 4x4 array of 1.2mm microstages packaged in a DIP. (c) A 5x5 array of 1mm microstages packaged in a different DIP.

### 3.4. Results and Characterization of Microstage Zipper Actuators

Fabrication of these microstage actuators followed the procedure outlined above in §3.3, and were fabricated alongside the simple cantilevers characterized above. As was the case by cantilever beams, film thickness characterizations reveal that the resultant Si and SiO<sub>2</sub> layer thicknesses were 5.72 μm and 0.52 μm respectively.

#### 3.4.1. *Deflection Characterization*

Based on these values the analytic model predicted a deflection of 211 μm, the FEM model a deflection of 212.1 μm and the average measured deflection of 84 1mm

actuators was  $212\ \mu\text{m}$  with a standard deviation of  $7.2\ \mu\text{m}$ , shown in Figure 34(a). An array of 24  $1\ \text{mm}$  actuators is shown inset in Figure 34(a). Optical defocusing was used to measure the deflection of the fabricated actuators. Measurements were taken at each turn of the serpentine and plotted together with deflection values from a COMSOL model in Figure 34(b). The results validate the fact that oxide can be grown uniformly and repeatably to produce identically performing actuators even over a large array.

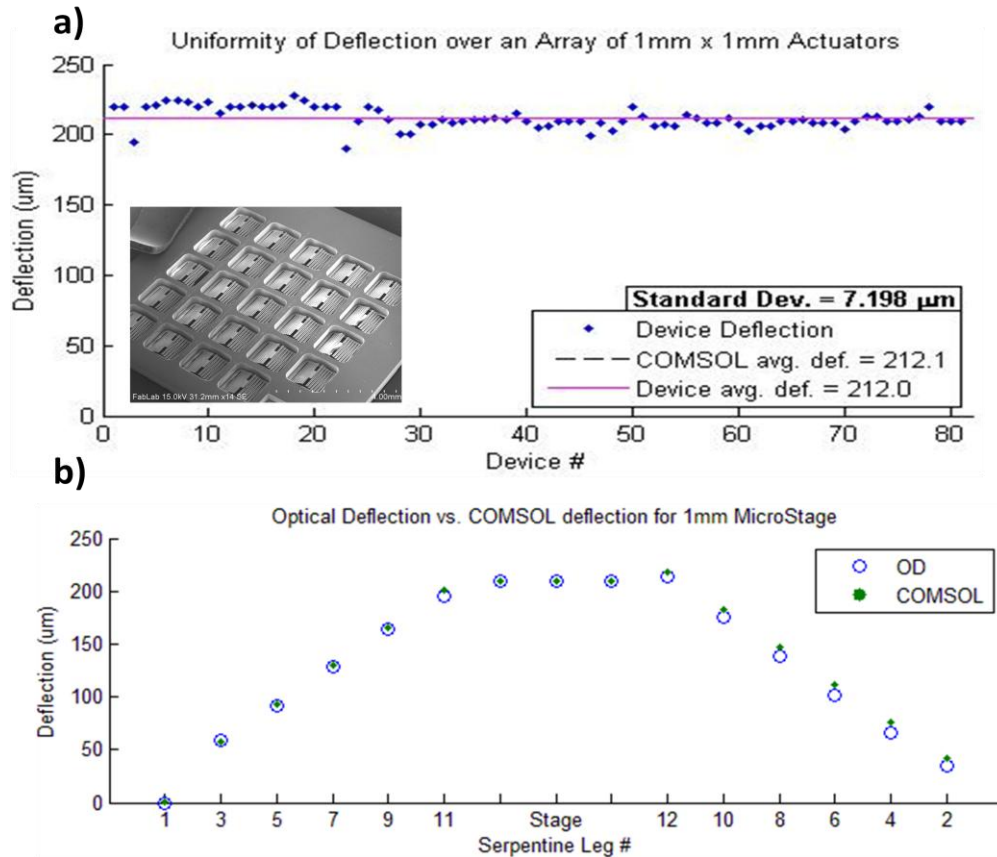


**Figure 34: (a) Uniformity of deflection over an array of eighty four  $1\ \text{mm}$  microstages. An array of twenty four  $1\ \text{mm}$  actuators is shown inset. (b) Agreement between optical defocusing deflection measurements and the COMSOL model for the microstage.**

Though the scope of this research was restricted to actuators with a footprint  $1 \text{ mm}^2$  or less, microstage actuators were fabricated with footprints ranging from  $1 \text{ mm}^2$  to  $2 \text{ mm}^2$  for the sake of academic interest and for adding validity to the model.

**Table 4: Microstage actuators of various footprints and geometries. Measured deflections are compared to analytically and numerically modeled deflections.**

<i>Microstage Dimensions</i>					<i>Model <math>\delta</math></i>		<i>Measured <math>\delta</math></i>		
<i>Footprint</i>	<i>n</i>	<i>w</i>	<i>L<sub>max</sub></i>	<i>L<sub>c</sub></i>	<i>COMSOL</i>	<i>MATLAB</i>	<i>Measured</i>	<i># of Samples</i>	<i>Std Dev</i>
1.0 mm	11	30	1000	308	212	212	212.0	84	7.2
1.2 mm	7	50	1200	370	202	204	203.1	16	1.8
1.3 mm	6	70	1300	402	204	210	211.6	15	9.4
1.4 mm	5	90	1400	433	206	208	185.1	9	4.2
1.5 mm	5	90	1500	464	237	240	267.3	11	6.8
1.6 mm	5	100	1600	495	271	273	293.2	12	7.7
1.8 mm	5	120	1800	557	345	347	359.1	8	6.4
1.9 mm	5	130	1900	588	384	388	391.8	8	6.9
2.0 mm	5	140	2000	619	430	430	425.0	2	21.2

Deflection was measured using optical defocusing (OD), and the results match very well with both the analytic and numeric models, thereby validating them. Moreover, the results demonstrate that Si/SiO<sub>2</sub> zipper microstages can be reliably and predictably fabricated, over large arrays, in a variety of geometries to achieve a specified deflection.

### 3.4.2. Voltage Characterization

A P-doped Si wafer coated with  $1.34 \text{ }\mu\text{m}$  of SiO<sub>2</sub> was used as the electrode. A power supply (Agilent E3612A) was used to ground the electrode and apply voltage to the actuator. Voltage was increased beginning at 0 V and deflection of the center stage was measured as voltage increased, until pull-in was observed. Figure 35 presents the results for two different 1 mm microstages;  $V_{PI}$  was 99.1 V and 101.7 V respectively. This value of  $V_{PI}$  is markedly different than the 46.4 V expected from the analytic

model. As explained above in §2.4.1.1 regarding simple cantilever beams, the model for pull-in voltage does not account for the effects of the rough electrode surface. However, the mechanical bonding scheme used here in conjunction with the surface roughness consistently result in a measured  $V_{PI}$  that is roughly twice the value output by the analytic model. This is consistent with results from the cantilever beams presented in §2.4.1.1, thereby validating the actuation voltage model for microstages.

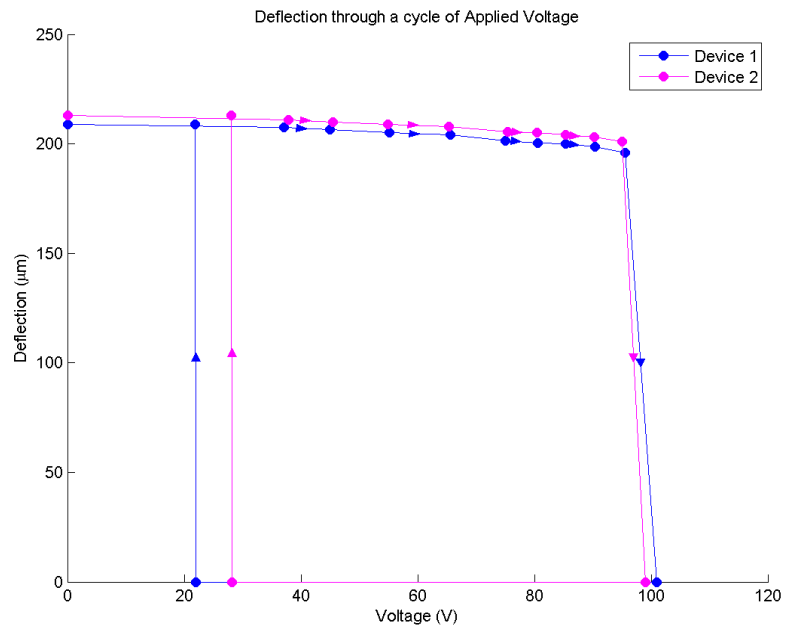


**Figure 35: Voltage-Deflection curves for two different 1 mm actuators. Voltage was ramped from 0 V and deflection of the center stage was measured until pull-in occurred. Voltage was ramped down until the actuators released.**

Note that Figure 35 shows a large hysteresis between the actuation voltage and the release voltage. In contrast to when the beam is deflected, once the beam is in contact with the electrode, there is a smaller uniform gap between the electrode and the beam at all points along the length of the beam. This results in a lower required electrostatic force to maintain actuation. Generally, hysteresis is an undesired effect, but in this case it is quite beneficial. It indicates that once a device is actuated, the voltage can be decreased dramatically but still maintain actuation.

Earlier, stiction had been observed when using an atomically smooth electrode surface. In the result reported above, the electrode was flipped over to the rough, unpolished side (RA 240 nm) of the wafer. After actuation, all microstages within the array released immediately and in unison, thus eliminating stiction, and confirming that undefined charge at the dielectric-dielectric interface is also not an issue. Figure 36(a) shows an array of twenty four 1 mm actuators at 0 V in their natural, deflected position of 212  $\mu\text{m}$ . Figure 36(b) shows the same array at a voltage of 120 V, collapsed entirely at the ground plane. Figure 37(c-d) show the same, though zoomed to a single actuator in the array.

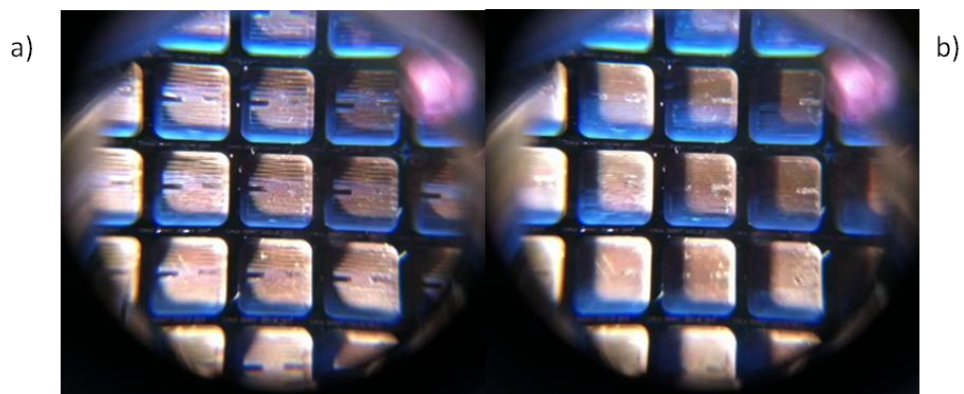


**Figure 36: (a) An array of 24 1mm microstages in their naturally deflected position at 0 V. Light can be seen reflecting off the curvature of the beams. (b) The entire array pulled-in at  $V = 120$  V.**

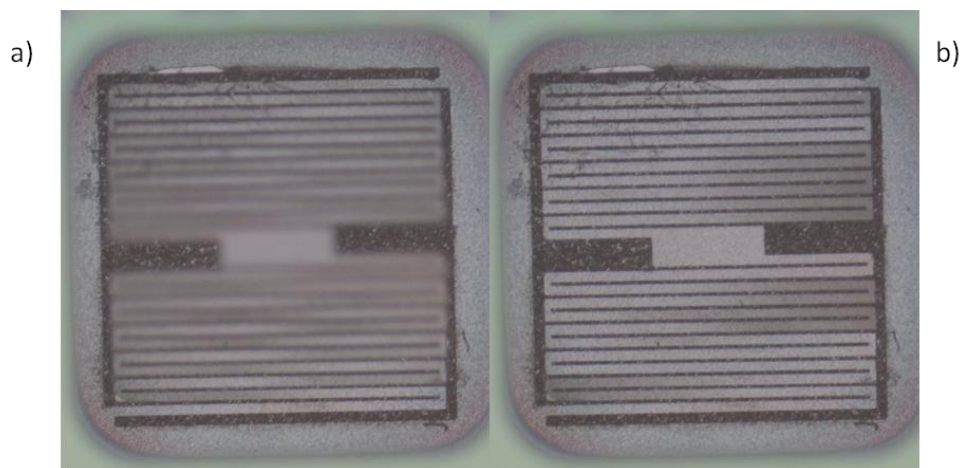


**Figure 37: A single 1mm actuator from the array above at (a) 0 V and (b) 120 (V).**

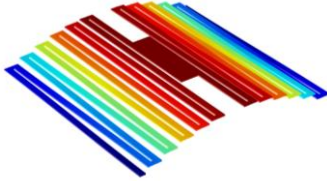
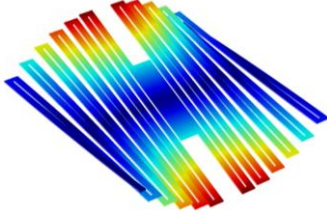
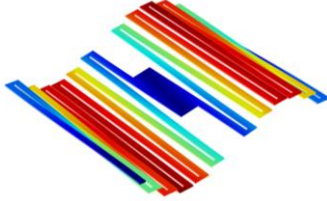
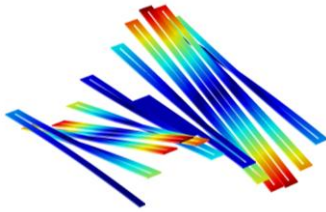


### 3.4.3. Dynamic Characterization

Given that the characterization results for deflection and pull-in voltage served to validate the model, we can confidently use the analytic and numeric models presented in §3.2.2.2 to determine the microstage's dynamic characteristics.

Fundamentally, the microstage consists of two serpentine actuators, coupled in parallel to the stage at the center. Each serpentine can be modeled as a set of clamped-guided beams in series, resulting in an effective spring constant,  $K_{eff}$ , for the entire microstage. Using equation (29),  $K_{eff}$  for the fabricated microstages is 0.168 N/m. Similarly, the effective spring constant based on COMSOL is 0.15 N/m which matches very closely to the analytic value. Additionally, using the definition for blocking force developed in §3.2.2.2, the microstage presented above has a blocking force of 0.035 mN. COMSOL was also used to find the resonant frequencies and corresponding mode shapes (Table 5). The natural frequency is 946.8 Hz, and the switching time,  $\tau$ , is 1.05 ms.

**Table 5: Mode shapes and resonant frequencies for fabricated 1mm actuator.**  
 $L_c = 1000 \mu\text{m}$ ,  $w = 30 \mu\text{m}$ ,  $n = 11$ ,  $h_s = 5.72 \mu\text{m}$ ,  $h_o = 0.52 \mu\text{m}$ ,  $\delta_{stage} = 212.1 \mu\text{m}$ ,  $K_{eff} = 0.155 \text{ N/m}$ .

Mode	Freq. (Hz)	Mode Shape
First Mode	946.8 Hz	
Second Mode	1046.3 Hz	
Third Mode	1883.7 Hz	
Fourth Mode	2109.1 Hz	

#### 3.4.4. Mechanical Durability and Reliability Testing

The arrays of 1 mm actuators were tested for mechanical durability and reliability by cycling through sequences of actuation and release. In conjunction with the IC board described above, a function generator (Agilent 33120A 15 MHz) was used to apply a square wave (5 Hz, 100ms pulse width, 4.9 Vpp) to the TTL input, resulting in 5 actuation and release cycles every second. Within a single array, two different 1 mm

microstage actuators were observed over the span of 55 hours (990,000 actuation cycles) and an image was recorded through a digital microscope (Nikon LV-100) every minute. After 55 hours, both actuators were observed behaving exactly as they had at the beginning of the experiment. There was no performance degradation, and close inspection of the anchor points, where stress is the greatest, showed no signs of deterioration. Moreover, though the actuators were fabricated and packaged in a class 1000 cleanroom, actuation testing, including this 55 hour run was carried out in a nominally clean standard laboratory with varying and uncontrolled levels of ambient conditions. This testifies both to the mechanical robustness and resiliency to environmental conditions of the presented microstage actuators.

It should be noted that the switching time of the microstage actuator as denoted by equation (31) above is approximately 1 ms. However, the electrical time constant of the IC board prevented actuation at a frequency that could verify the mechanical time constant of the microstage.

### 3.5. Design Capabilities of Microstage Zipper Actuators

Having verified both models through the previous actuator design, we can now explore the extreme capabilities of the electrostatic zipper microstage actuator. If we relax the 1 mm x 1 mm footprint constraint, actuators capable of achieving over 1 mm of vertical deflection can be developed. Figure 38 shows a 2 mm x 2 mm actuator ( $h_s=8.95 \mu\text{m}$ ,  $h_o=1.81\mu\text{m}$ ) whose measured center stage deflection is 1243  $\mu\text{m}$  in good agreement with a COMSOL model prediction of 1228  $\mu\text{m}$  and the analytic prediction of 1236  $\mu\text{m}$ . Both calculated from the model, the switching time,  $\tau = 4.7$  ms and the blocking force,  $F_b = 0.085$  mN. Table 6 below presents the extreme

capabilities ( $\delta_{\text{stage}}$ ,  $SR$ ,  $V_{PI}$ ,  $F_b$ ,  $\tau$ ,  $SF$ ) that can be obtained by varying microstage characteristics ( $h_s$ ,  $h_o$ ,  $w$ ,  $n$ ,  $h_{o2}$ ).

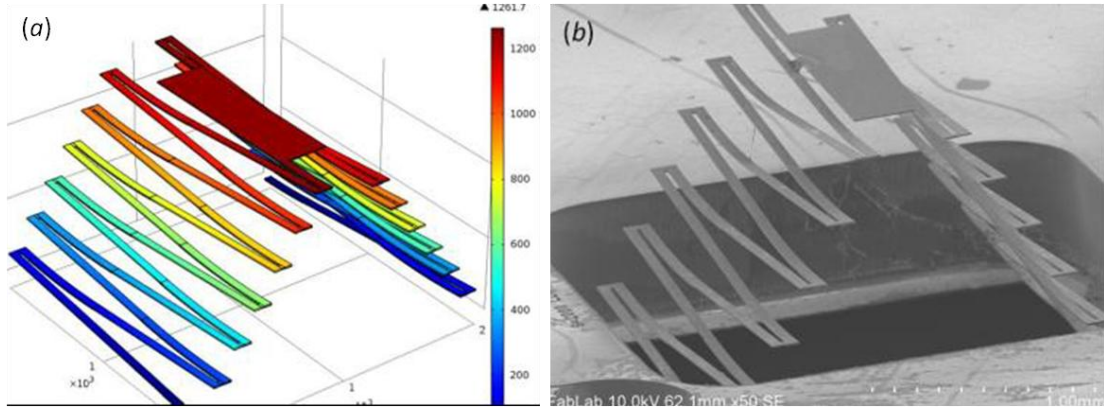


**Figure 38:** (a) A 2mm microstage modeled in COMSOL with deflection of 1228  $\mu\text{m}$ , and (b) a fabricated 2 mm microstage with measured deflection of 1243  $\mu\text{m}$ . For reference, the wafer thickness shown framing the microstage is 525  $\mu\text{m}$ .

**Table 6: Possible design inputs demonstrating the extreme capabilities of the microstage actuator. Cells highlighted in green represent the extreme value, while those in yellow represent the tradeoff in other areas needed to achieve the extreme result.**

Footprint	Actuator Design Inputs					Model Mechanics Output					Model Voltage Output			
	$L_c$ ( $\mu\text{m}$ )	$w$ ( $\mu\text{m}$ )	$h_s$ ( $\mu\text{m}$ )	$h_o$ ( $\mu\text{m}$ )	$n$	$\delta_{\text{stage}}$ ( $\mu\text{m}$ )	Stroke Ratio	$K_{\text{eff}}$ (N/m)	$F_b$ (mN)	$\tau$ (ms)	$h_{o2}$ ( $\mu\text{m}$ )	$V_{PI}$ (V)	$SF$	
#1	308	100	9.90	2.22	4	113	0.11	9.695	1.099	0.19	2.50	218.70	2.00	
#2	308	20	3.00	1.49	14	1891	1.89	0.019	0.036	2.13	2.06	179.96	2.00	
#3	1000	308	20	3.40	0.30	14	458	0.46	0.021	0.010	2.08	0.30	19.90	2.64
#4	308	20	8.70	0.42	14	101	0.10	0.343	0.035	0.82	0.30	19.54	2.69	
#5	308	90	4.00	0.97	4	300	0.30	0.582	0.175	0.50	1.13	98.70	2.00	
#6	500	154	20	3.00	1.49	7	240	0.48	0.301	0.072	0.70	2.06	180.00	2.00
#7	250	154	50	3.50	1.74	3	100	0.20	2.785	0.278	0.26	2.41	210.30	2.01
#8	250	77	10	2.00	0.99	5	66	0.27	0.498	0.033	0.52	1.37	119.60	2.00

Microstages with a 1 mm x 1 mm footprint can be fabricated that can achieve a blocking force of 1.1mN (Device #1), total deflection greater than 1.8 mm for a stroke ratio of 1.89 (Device #2), and pull-in voltage below 20 V (Device #3) at over 450  $\mu\text{m}$  deflection. Device #5 presents a microstage with moderate values across most metrics. Moreover, if the device footprint is reduced to 0.5 mm x 0.5 mm large deflections (Device #6) and high blocking forces (Device #7) can still be achieved.

Lastly, in an area only 0.25 mm x 0.25 mm, deflections over 60  $\mu\text{m}$  can be reached, for a stroke ratio of 2.4.

### 3.5.1. Benchmarking

Recalling the figure of merit presented in §2.5.1, EPPA, the microstage is compared to established out-of-plane actuators that possess a vertical actuation trajectory. EPPA (electromechanical performance per area) measures the mechanical output achieved for every volt required to actuate the zipper, normalized to the area it occupies. In this way, performance of actuators of different shapes, sizes and mechanics can be compared. Recalling equation (22), the switching time of the actuator is not present in determining EPPA. This is because all actuators being considered were electrostatic zipper types, in which the switching time is related to the same parameters that influence the blocking force. Hence, switching time is “built in” to the metric. In this case, where actuators whose switching times are defined by their different methods of actuation (electrothermal transduction, TMFG, comb-drive) are being compared, EPPA must be updated to include the switching time. Therefore, EPPA is now defined as

$$EPPA = \frac{\delta F_b}{\tau A_s V_{PI}}, \quad (33)$$

where the switching time has been added to the denominator.

With this update, the scores of established out-of-plane vertical actuators were found and tabulated in Table 6 along with some of the Si/SiO<sub>2</sub> electrostatic microstage actuators presented above. Again, the EPPA scores were normalized to the lowest score of the group in order to obtain a meaningful relationship between the different flavors of actuators.

**Table 7: EPPA scores for Si/SiO<sub>2</sub> actuators compared to established out-of-plane actuators.**

Actuator type		Electromechanical Output							EPPA	
Source	Type*	$L_c$ ( $\mu m$ )	$w$ ( $\mu m$ )	$A_s$ ( $\mu m$ )	$\delta_{stage}$ ( $\mu m$ )	$F_b$ ( $mN$ )	$\tau$ ( $ms$ )	$V_{PI}$ ( $V$ )	Raw EPPA	Normalized EPPA
#1	ZIP	1000	1000	1000000	113	1.099	0.19	218.7	2.97E-06	78.87
#7	ZIP	500	500	250000	100	0.278	0.26	210.3	2.04E-06	54.45
[23]	TFMG	1000	1000	1000000	200	0.830	0.75	81	2.71E-06	72.14
[5]	ET	2500	2500	6250000	621	0.050	25.00	5.3	3.75E-08	1.00
[9]	CD	1000	2000	2000000	55	0.100	2.50	7	1.57E-07	4.19

\*ZIP = Si/SiO<sub>2</sub> type, ET = Electrothermal, TFMG = Thin Film Metallic Glass, CD = Comb Drive

Using data reported for electrothermal [5] comb drive [9] and TFMG [23] out-of-plane actuators, the EPPA was found and tabulated in Table 7 along with Si/SiO<sub>2</sub> microstage actuators. Compared to both electrothermal transduction, and comb-drive out-of-plane actuators, the Si/SiO<sub>2</sub> zipper microstages achieve nearly 80 times more electromechanical output. Data was normalized to the electrothermal actuator [5], which had the lowest EPPA of the vertical actuators considered. This was due primarily to its slow switching time. Moreover, in calculating EPPA, no explicit consideration was given to the fact that electrothermal transduction consumes continuous power, though this is accounted for to a degree by the inclusion of switching time, since both metrics are directly related to the heating mechanics of actuation employed in electrothermal transduction. Despite high deflections (600  $\mu m$ ) and low actuation voltages (<10 V), their fundamental mechanics make them inefficient, and this is reflected in their EPPA scores. A similar argument is made for electrostatic comb-drive actuators. Though they can require low actuation voltages (<10 V) and switch relatively quickly (2.5 ms), the total deflection (55  $\mu m$ ) and force output (0.1 mN) is minimal considering the area they occupy. Though their EPPA

score is 4 times that of electrothermal transduction vertical actuators, they are still significantly less productive than the Si/SiO<sub>2</sub> zipper microstages developed here, which achieve 20 times more electrothermal output.

On the other hand, TFMG electrostatic actuators also achieved a high relative EPPA score (EPPA=72), with output metrics that compare similarly to Si/SiO<sub>2</sub> zipper microstage actuators. However, as discussed in §1.1.1, TFMG actuators are limited in reliability and repeatable performance by their substantially more complex fabrication process, and dielectric charging issues leading to delays in actuator release. This, though, is precisely the advantage of Si/SiO<sub>2</sub> fabrication of vertical actuators. They provide a simple, straightforward, repeatable process using classic MEMS fabrication techniques, for achieving high electromechanical productivity – large out-of-plane deflections, milli-Newton output forces, sub-millisecond switching times, and moderate to low actuation voltages, unaffected by charging issues, coupled with tremendous flexibility in terms of design optimization.

### 3.6. Summary

Spiral geometries were explored in an effort to develop a geometry capable of out-of-plane actuation through a vertical trajectory. They were unsuccessful due to physio-mechanical constraints stemming from the nature of the Si/SiO<sub>2</sub> bimorph concept. Serpentine microstage actuators comprised Si/SiO<sub>2</sub> zipper bimorphs in series, linked in parallel at a center stage were developed to achieve this goal. The analytic model developed for cantilever beams was expanded to cover microstage actuators as well. Similarly, the numeric model was updated to account for the new microstage geometry. The fabrication process was detailed, with special attention given to the

design of the electrode, its implementation and the effects of the design on device performance, particularly actuation voltage. Fabricated devices were characterized with respect to deflection and actuation voltage, and the results were used to validate the adapted models. Dynamic modeling of the devices was presented and mechanical durability and reliability testing was administered. No performance degradation was observed as the actuator approached 1 million actuation cycles. Having validated the model, the capabilities of the Si/SiO<sub>2</sub> microstage actuators were presented, and the concept was benchmarked against established out-of-plane vertical actuators. Si/SiO<sub>2</sub> microstage actuators performed 20-80 times better than many of their counterparts.



## Chapter 4: Conclusion

This goal of this work was to develop an out-of-plane microactuator, capable of large vertical deflections, high forces, fast switching times, and low voltage requirements. Cantilever beam Si/SiO<sub>2</sub> zipper actuators were developed that outperform their peers in terms of electromechanical productivity. That is, they achieve more overall mechanical output (deflection, force, etc.) per volt, than previously established technologies. Similarly, microstage actuators based on Si/SiO<sub>2</sub> zipper actuators were also developed, whose deflection trajectory is vertical. The microstage is capable of extreme deflections within a controlled footprint, milli-Newton force, sub-millisecond switching times, and low voltages. Like its cantilever counterpart, the microstage achieves more electromechanical productivity than many of the vertical actuators already in existence. The major improvements attained by the cantilever and microstage presented here are due to the fact that they are fabricated from Si/SiO<sub>2</sub> MEMS technology. The use of an SOI and classic MEMS fabrication provides for a simple and well-understood fabrication process that results in repeatable and uniform performance. The use of SiO<sub>2</sub> as a high quality dielectric, and the stressor in the bimorph, results in precise and predictable performance. Together with silicon, large forces and high deflections can be achieved, while keeping actuation voltage moderately low. The marriage of robust materials with a simple fabrication process is the innovation that results in substantially improved vertical actuation on the microscale.

#### 4.1. Contributions

The contributions of this work can be separated into three primary categories:

1. A modeling approach was presented that combined analytic and numeric modeling in a cyclical process that was simultaneously validated and improved upon through the results. This approach synthesizes the accuracy of analytic modeling, based on time-tested mathematical theory, with the power of finite element methods to expand the reach of predictive modeling saving time and substantial cost in the process. It allowed for the presentation of a wide range of results, in the form of cantilever and microstage capabilities, without the time and cost required to fabricate and characterize tens if not hundreds of devices. The iterative process, tuning and improving the model based on results, in conjunction with two very different yet parallel modeling methods, allows for a certain measure of confidence when presenting “results” and the capabilities of the Si/SiO<sub>2</sub> electrostatic actuators.
2. The novel use of creating curved, compliant out-of-plane structures from bulk SOI is a key contribution of this work. Similarly, the ability to fabricate arbitrarily thick beams, limited only by the thickness of the active silicon layer of the SOI, and the capacity to grow thermal oxide, is fundamentally important as well. Moreover, this project is the first to use SiO<sub>2</sub> as both a high quality dielectric, and the bimorph stressor to provide well defined beam curvature and consistent electrostatic actuation. “Without question, thermal oxidation of silicon is the most thoroughly studied and well understood of all the film growth processes” [27]. It is this property that allows for unparalleled

control of film qualities, resulting in robust actuators with uniform and repeatable performance, greater deflection and larger forces than previous designs. This is perhaps the greatest contribution of this work, for it represents the first entirely non-metallic out-of-plane electrostatic zipper actuators, and constitutes a substantial improvement in the field.

3. Not to be understated is the tremendous design flexibility inherent in Si/SiO<sub>2</sub> zipper actuators. Vertical trajectories, cantilever beams, 2 mm deflections in a 1mm<sup>2</sup> area, 1 mN forces, sub-millisecond switching times, less than 20 V actuation volts; the output capability spectrum runs the gamut, due to the unparalleled film control, and unmatched film thicknesses.

## 4.2. Future Work

### 4.2.1. *Design and Model Improvement*

In parallel to the above direction of future work, development of a method for eliminating the secondary dielectric would provide for more accurate modeling, eliminating the complexities it introduces. More importantly, though, it would reduce the required actuation voltage, since  $V_{PI}$  scales with the gap between the electrodes. An attempt, described in §3.3.3.1, was made at achieving precisely this feat, by aligning a patterned silicon electrode to the patterned oxide of the microstages, though it was fraught with challenges. Future development of a fabrication scheme that would pattern the electrode and oxide beams *in situ*, eliminating the need for alignment, would constitute a significant improvement to the overall design and capabilities.

At the same time, improving the accuracy of the model by developing mathematical expressions that more precisely describe the electric field and the ways in which the dielectric layer affect it, would be a meaningful contribution, both to this project, and the community at large. FEM methods such as COMSOL can be used to better understand the effects, and as a springboard from which mathematical development can commence. Modeling a non-periodic surface roughness is somewhat complex, but using simple models, COMSOL can tell us much.

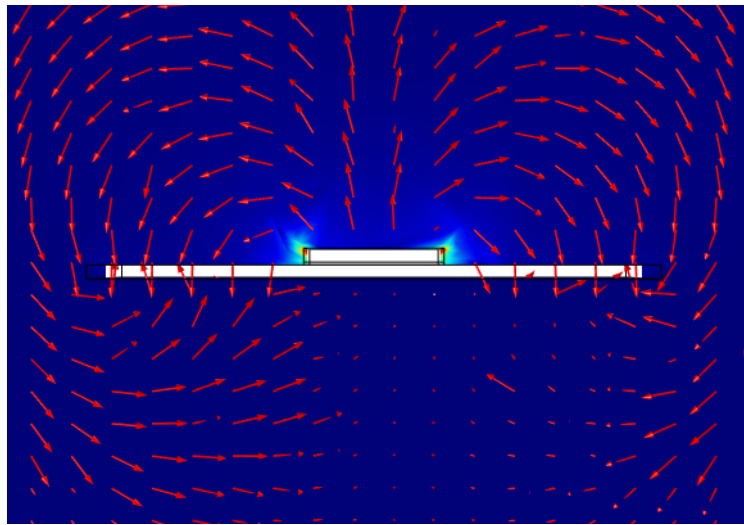


**Figure 39: Electric field created by a voltage applied to actuator beam on unshielded electrode.**

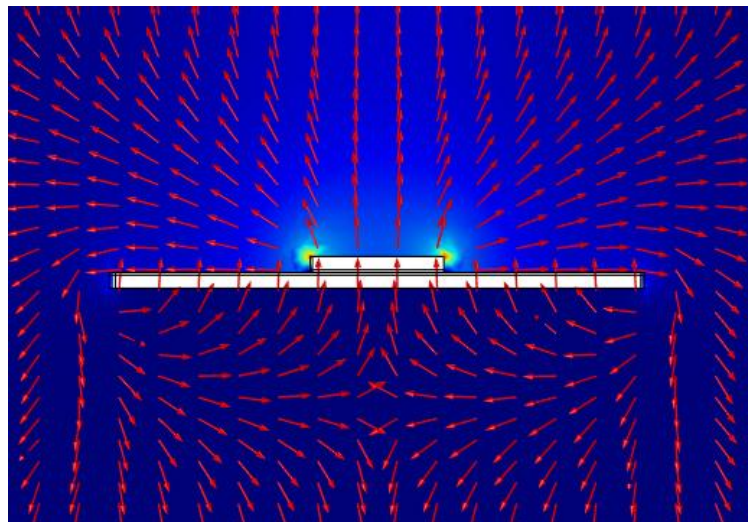


**Figure 40: Electric field created by voltage applied to actuator beam on shielded electrode.**

Figure 39 charts the electric field lines created by applying a voltage to the zipper actuator as it rests on a bare conductive electrode. In contrast, Figure 40 charts the same, but for a zipper actuator on a shielded electrode (coated in a secondary oxide). According to COMSOL, the strength of the “unshielded” electric field is much greater than the strength of the “shielded” electric field. Therefore, the voltage in the shielded scenario would have to be increased significantly in order to achieve the same electrostatic force as the unshielded case. This is part of the reason why adding a secondary dielectric to the zipper actuators necessitated a higher actuation voltage. We already knew this, but modeling of this nature can give real insight into how to improve the mathematical and analytic model as well.

Finally, the current microstage consists of two serpentine flexures in parallel. This was chosen to maximize the length of the beams by allowing them to be as long as the area the device occupies. However, more investigation would be worthwhile to see whether the addition of two more flexures would offer more improvement. To maintain the same area footprint, the current beams would have to be shortened to accommodate the beams of the new flexures. In order to maintain the deflection, the beams could be made thinner to achieve a smaller radius of curvature, or narrower to accommodate more beams per serpentine. The effect of either of these would be to reduce the force output, but the addition of two more flexures in parallel would serve to increase the rigidity and the force output. Future work would study to what extent these changes effect the outputs, and would work on optimization schemes for maintaining, or improving the current designs performance.

#### 4.2.2. Large and Individually Addressable Arrays

Future work will entail the development of an addressable array of actuators through the use of a more complex electrode scheme. Electrostatic actuation is achieved through a difference in voltage bias, but is indifferent to whether the bias is applied to the actuator electrode, or the ground electrode. This is a tremendous advantage in terms of creating large scale arrays of microstage actuators because one could, in theory, fabricate the entire actuator array as one continuous layer, and set that layer to ground, while the electrode layer is biased. This has major ramifications in simplifying the fabrication process in the sense that there is no signal routing to the actuator layer, something which is a challenge in other actuators. Moreover, the packing density of the array is limited only to the footprint of each individual actuator. That is, for a 1 mm x 1 mm actuator, a 10 x 10 grid can be packed in into a space just slightly larger than 10 mm x 10 mm.

Figure 41 shows a 5 x 5 array of 1 mm microstages, each supporting a 300  $\mu\text{m}$  thick silicon pixel. Because of the efficient packing density, there is only a 5  $\mu\text{m}$  gap between each actuator/pixel.

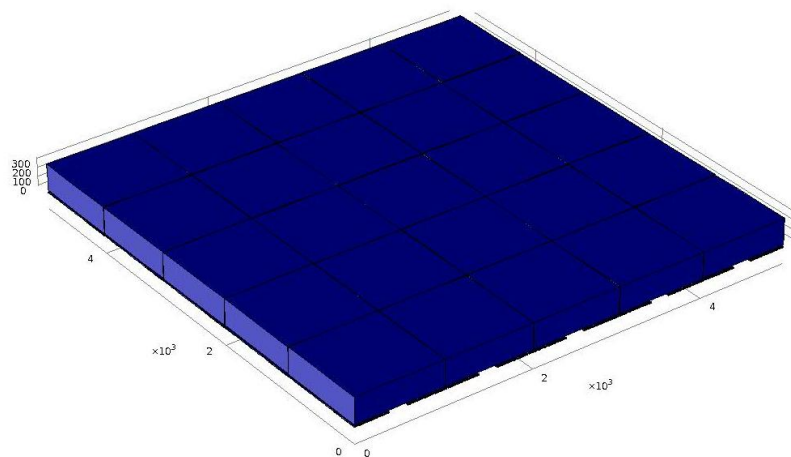


**Figure 41: A 5 x 5 pixel array supported by 1 mm microstages underneath.**

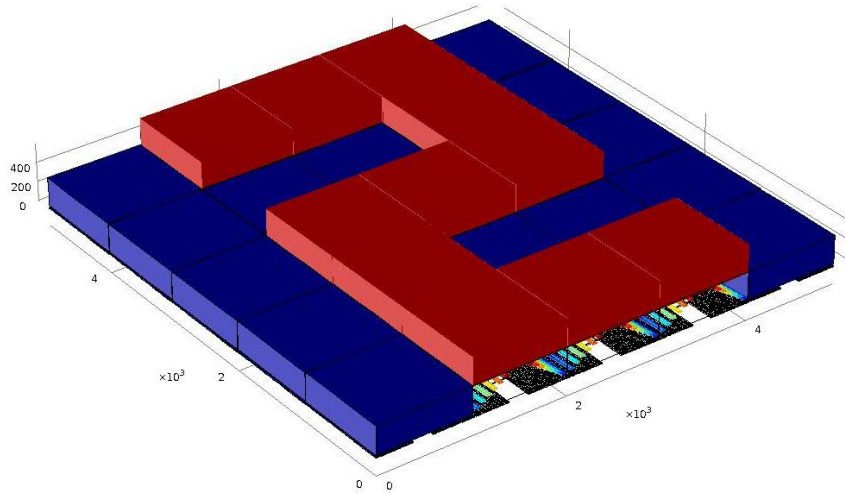


**Figure 42: Individually addressed actuators raise pixels in a defined pattern. The microactuators can be seen underneath the raise pixels.**

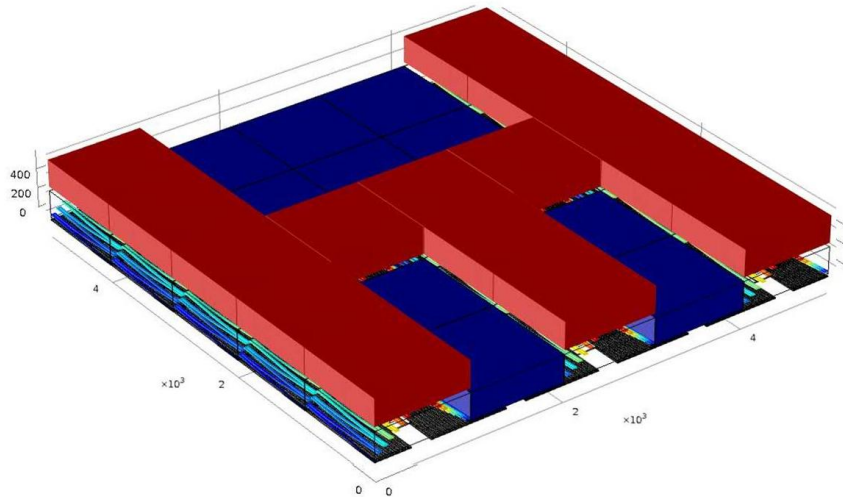


**Figure 43: Antenna-like structure defined by raised pixels.**

Figure 42 and Figure 43 demonstrate the capability of the microstage to precisely control the deflection of an array of pixels to define various geometries, limited only by the size of the array. Individually addressable electrodes would be used to manipulate arrays like these.

#### *4.2.3. Load Bearing Modeling and Testing*

Ultimately, one of the key characteristics of the microstage presented here is the flat center stage to which a load could be fixed. We aim to develop an integrated

fabrication process in which a load can be actuated atop the microstage. Work is already underway with regards to this goal. In parallel, analytic and numerical modeling of the Si/SiO<sub>2</sub> microstage capabilities while actuating a load can be developed.

An application of the microstages is in refreshable, large scale arrays. In particular, software defined microstrip patch antennas, capable of reconfiguring their size and shape to attain any number of different antenna characteristics, would make use of these microstages. Conductive pixels (similar to the silicon blocks in Figure 43, but metalized on top and bottom) would be affixed to the center stage of the microstage, and, when raised, would define the shape of the antenna transmission line. Large arrays would have an exceedingly large number of configurations, thereby making the antenna extremely dynamic.

#### 4.2.4. *Stable Stepwise Displacement*

In many MEMS applications, the binomial nature of electrostatic zipper actuation is desired. The fact that there are no stable equilibrium points is beneficial, especially when used as switches and relays. However, there are also many cases where there is a need to control the deflection resolution to a more precise degree than offered by electrostatic zipper actuators. This is particularly true in the field of microoptics, where microactuators are used to focus light by moving the location of a lens. It would also be true in the future application of MEMS vertical actuators to the field of haptic displays (see §1.1). Computer screens of the future may be composed of pixels that not only transmit images, but can move out of the plane of the screen to transmit



texture and shape as well. For this application, a binomial design isn't sufficient either.

The Si/SiO<sub>2</sub> microstage as presented in this work has two stable states: a) when voltage is not applied, and the actuator rests in its naturally deflected state, and b) when voltage is applied and the actuator collapses to the ground electrode. Yet, the nature of its design makes it easily adaptable to an actuation scheme that would enable stepwise displacement. Each leg in the serpentine flexure is composed of isolated curved segments that are responsible for deflection and actuation (see §1.1.2 and §3.1.2). Though a single ground plane electrode was used for actuation here, an electrode could be easily fabricated in which each segment of the microstage flexure could be individually actuated. Much the same way an electrode is being developed to address individual actuators in an array, a similar electrode could be developed to address individual serpentine legs in a single actuator. Figure 44 shows a COMSOL sequence of images in which 0, 1, 3, 5 and 9 legs of each serpentine have been actuated. For each leg that is actuated, the stage deflects another increment  $\Delta$ , as defined in equation (25), thereby achieving stepwise deflection. For each beam that is actuated, the center stage remains stable and parallel to the ground plane. In the last image of the sequence, deflection measurements were taken in COMSOL at each of the four corners of the microstage and their values were 49.68, 49.65, 49.65, 49.63  $\mu\text{m}$ , demonstrating that the center stage remains parallel at each step.

Thought would have to be given to the geometry of the microstage, and optimization would undoubtedly be necessary. As discussed in §3.3.3.1, alignment between the actuator and electrode layer is not simple. Hence, design of the beam

width, and the spacing between the beams would be a critical design choice – more spacing between beams eases alignment, but occupies more area decreasing the number of serpentine beams that can be fit into a given area, thus decreasing the total deflection. Nonetheless, the microstage is amenable to stable stepwise displacement, through simple reconfiguration of the electrode.

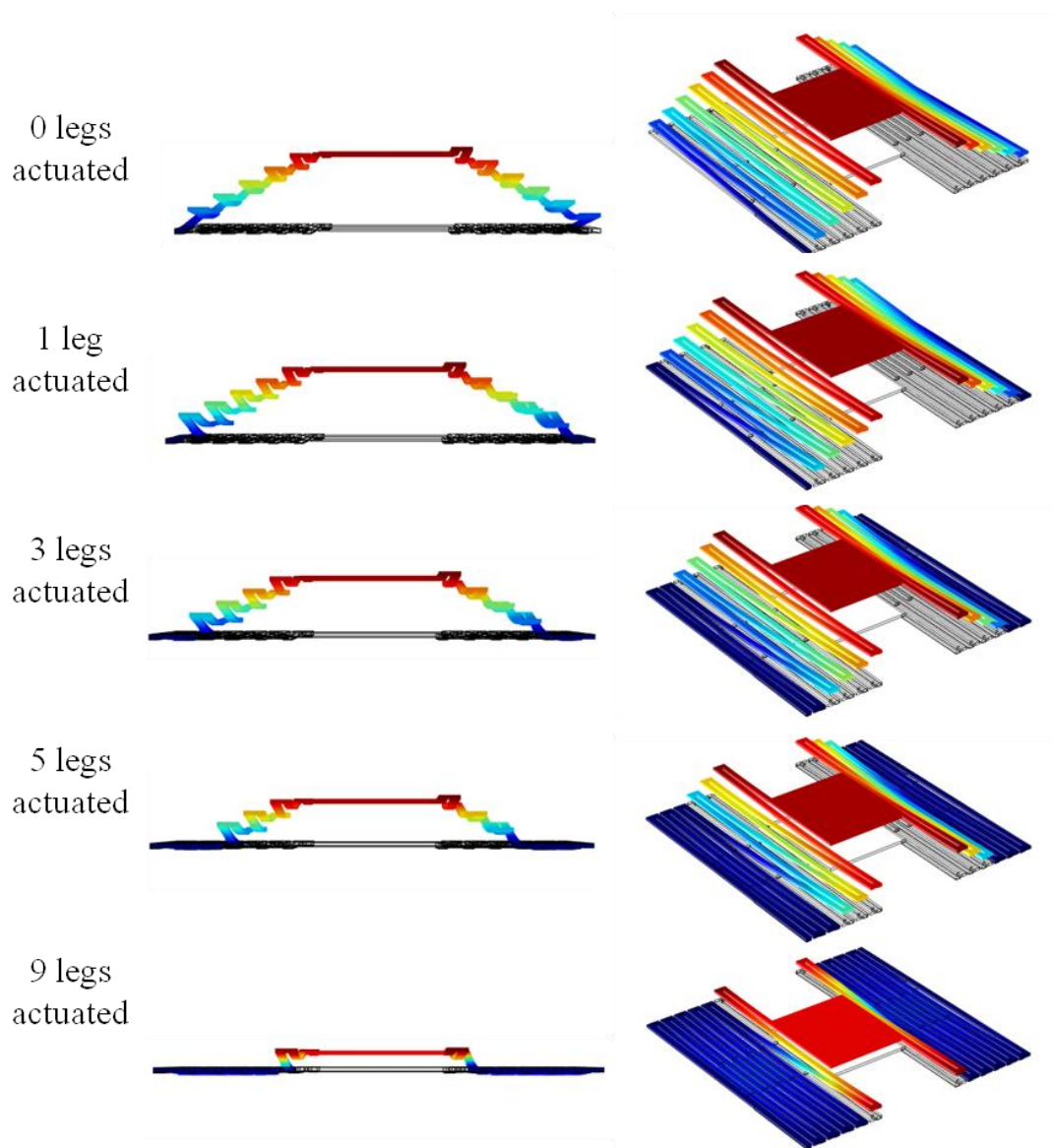


**Figure 44: Stable stepping motion achieved with microstage by individually addressed electrodes for each serpentine beam.**

## Appendix A: Recipes and SOPs

This Appendix contains the entire fabrication process, from start to finish, beginning from the first MEMS processing step to the last packaging step.

Preliminaries:

- The SOI must be conductive, since the frontside silicon will be electrode on the bimorph. A resistivity of less than 10 Ohm-cm is fine.
  - The performance of the actuators is very sensitive to the thickness of each layer. While this process allows for precise control of the layer thicknesses, it is important to always measure every layer, and not assume it has a certain thickness. For example, as soon as an SOI wafer is obtained, measure the thickness of the handle wafer, because it's likely close to, but not exactly the thickness that was ordered.
  - The process used here requires three masking layers. Significant cost was saved by treating each quadrant of the mask as a new layer, and then just rotating the mask as needed. Also, the mask was designed to first pattern the oxide, and then the silicon underneath in self-defining process.
  - In practice, it's a good idea to test each etch process on a dummy wafer beforehand. Even so, once you feel that the process is ready for the SOI, it's a good idea to run a small amount of the process, characterize its effect, and then finish the process with your new data.
1. Wet thermal growth of  $\text{SiO}_2$ 
    - a. It is a diffusion limited process, which means the thicker the oxide layer desired, the longer it will take to grow. There are many online calculators

that help with this calculation. Keep in mind that the oxide is grown *from* the silicon, not deposited on top. Therefore, some of the silicon is consumed in the process, thinning the silicon layer. To be exact, 0.46 x the thickness of the oxide is the amount of silicon consumed. Therefore, it is very important to be aware of how thick the silicon is to begin with.

## FRONTSIDE PATTERNING

### 1. Oxide Patterning

#### a. Photolithography (mask layer 1)

- i. Dehydrate wafer for 1 minute
- ii. Puddle HDMS - spin for 40 sec @ 4000 rpm
- iii. Spin AZ4620 - 30 sec @5500 rpm, draw pour off wafer edge as it ramps its speed up
  1. 5.8 um of PR
- iv. Let sit for 3 min on spindle after it comes to rest. This allows the resist to settle.
- v. Bake 80 sec @ 110C on hotplate (if bubbles form in resist during UV exposure, increase bake time to 90s).
- vi. Rehydrate for 30 min by letting wafer sit on flat surface open to the air.
- vii. Expose 10 sec on EVG @ 15 mw/cm<sup>2</sup>
  1. See AZ4620 exposure calculator, for exposure doage
- viii. Develop 4.5 min in 4:1 DI:AZ400, or 80 second in 3:1 DI: AZ

#### b. RIE to pattern oxide

- i. Recipe: "SiO<sub>2</sub> - Felder"
  1. ICP=300W
  2. DC Bias=170V
  3. Forward Power=50W
  4. Press=4.2mT
  5. Temp=20C
  6. Gases: 10sccm C<sub>4</sub>F<sub>8</sub>, 10sccm He
    - a. PR etch rate = .09um/min, Oxide etch rate = .11um/min
  7. Etch time: 7:00
  8. Profilometer - .59-.6 um step height
  9. Strip PR in NMP, followed by piranha etch
    - a. If microscope shows residual resist inside Si features where it previously was clean under microscope, use an O<sub>2</sub> plasma etch to "descum" the wafer
    - b. O<sub>2</sub> plasma clean in March Jupiter III system
    - c. 3 min, 0.5 Torr O<sub>2</sub>, vacuum 0.2 Torr, RF power 200W
2. Pattern Silicon Beams
  - a. Photolithography (mask layer 2)
    - i. Spin 4620 to 5.8um using regular SOP
  - b. RIE to self-define beams
    - i. 8 min SiO<sub>2</sub>-Felder oxide etch
      1. ICP=300W
      2. DC Bias=170V

3. Forward Power=50W
4. Press=4.2mT
5. Temp=20C
6. Gases: 10sccm C4F8, 10sccm He
7. Etch time: 8:00

c. DRIE to pattern beams

- i. Etched frontside of SOI for 3 min (etch rate of about 3um/min), and measure in profilometer
- ii. Recipe: UMHIGH\_f in "felder" folder
- iii. Etch:Pass = 10:6 sec
- iv. Etch: 130 sccm SF6, 13 sccm O2
- v. Pass: 85 sccm C4F8
- vi. Coil Power: 600W reflectivity both etch and pass  
Platen Power: 17W etch, 0W pass
- vii. Profilometer
  1. Trench depth from oxide to BOX is 6um which is what it should be (5.3um Si + 0.56 um ox)

3. Backside Patterning

a. Photolithography

- i. Spin 4620 to 14 um.
- ii. Dehydrate wafer
- iii. HDMS (only need to do it once - not each run)

- iv. spin @ 1200 rpm with 200rpm/s ramp for 60 sec. Draw pour to edge..
  - v. Wafer Rest - let sit for 3 min
  - vi. Bake @110C for 80 sec
  - vii. EBR – Edge Bead removal is only necessary for the thicker films. If you do not remove an edge bead, it can cause the wafer to stick to the mask in the UV aligner, and can melt and stick to the platen in the RIE.
  - viii. Rehydrate for 20 min
  - ix. Sxpose 22.5 sec in EVG
  - x. Develop in 3:1 Di:AS400K for 60 sec
  - xi. Profilometer - 14 um
- b. RIE
- i. Backside RIE to remove oxide from windows
    - 1. Recipe: "SiO2 - Felder"
    - 2. ICP=300W, DC Bias=1V, Forward Power=50W,  
Press=4.2mT, Temp=20C,  
- Gases: 10sccm C4F8, 10sccm He  
- Etch time: 8:00
    - 3. DO NOT STRIP BACKSIDE PR
- c. DRIE
- i. Spin 2um 1813 on dummy wafer.

1. Spin 4um 1813 on frontside of SOI as well (2 spins back to back). Spun both at 1200rpm for a 2 um film on each, for a total of 6 um PR holding them together. Spun 1813 on SOI frontside to hold devices in place through completion of RIE. If there is not enough PR, the devices will burst through BOX during backside etch before it is complete.
2. Profilometer before DRIE showed trench depth of 12.5-13 um. which means 12-12.5 um PR on the backside to serve as DRIE mask.
3. DRIE for 10 min on UMHI\_NEG to calibrate etch rate
  - a. Profilometer: 50-51 um depth. Approx 3.8 um/min etch rate of Si.
  - b. DRIE for 60 min on UMHI\_NEG - designed to cut grass... changes etch:pass from 10:6 to 10:4... results are a world of a difference.
  - c. DRIE for 30 min on UMHI\_NEG
  - d. DRIE for 10 min - one or two devices has exposed BOX – This is the bullseye effect, the outer regions etch faster since the outermost region has no silicon around it, and therefore a higher gas concentration.
  - e. DRIE for 10 min
  - f. DRIE for 2 min (5 times) on "Iso-SI", new recipe that is isotropic



- g. SEM imaging to see if BOX is gone- method for checking if buried oxide is gone... microscope light sees BOX as transparent, even at 2 um, but SEM shows it as opaque.
  - d. RIE to remove BOX
    - i. Same recipe as frontside oxide.
    - ii. Etch time will have to be adjusted to the BOX thickness
- 4. Preparation for wafer dicing
  - a. Laminate dry film resist over exposed backside windows. A glass wafer, or other transparent film that can be cut into pieces is fine.
  - b. Dice using a microdicing saw. Dice through the thickness of the SOI into the thickness of the carrier wafer below
  - c. Let sit in acetone over night, or until actuator dies begin to float off of carrier wafer on their own accord. If you have to slide or pull off the actuators, you will break them.
- 5. Clean them well, piranha, O2 plasma etc., and actuate!

## Appendix B: EPPA Calculations and Notes

EPPA (Electromechanical productivity per area) is a fabricated figure of merit that quantifies, to an extent, the mechanical production per electrical input normalized to the area. It is used as a means for comparing the performance of different actuators – different shapes, sizes, mechanics among others. It is not perfect, but it offers a baseline from which comparisons can be made.

For cantilever beams, the equation was defined as

$$EPPA = \frac{\delta}{L^2} \times \frac{F_b L}{w} \times \frac{1}{V_{PI}} = \frac{\delta F_b}{L w V_{PI}} = \frac{\delta F_b}{A V_{PI}}. \quad (34)$$

and a brief explanation was given for how the final quantity was derived. Here, I'd like to dedicate some space to outlining how I arrived at each one of those EPPA values, mostly for sake of transparency and academic integrity. In many cases, authors reported numerous values for a metric, such as different values for the actuation voltage. In every case I did my best to choose the values that would benefit the EPPA score for the authors. After all, the goal is compare the Si/SiO<sub>2</sub> zipper actuators to the best that is out there, not to denigrate or disparage the work of others! With that, we shall begin with the zipper actuators in Table 3.

**Devices #1-5:** For the Si/SiO<sub>2</sub> zipper actuators, all values were calculated using the analytic model developed in this work.

**Device #6:** All of the information can be found in Fig. 4 and 5 in [20]. Maximum tip deflection is 30 μm, the maximum force, charted in Fig. 5 is just over 0.025 mN at a voltage of 200 V, the beam is 500 μm in length, and 5 μm in width. Simply put all these values into the above equation.

**Device #7:** Deflection and voltage were taken from Fig. 6, which explicitly state that deflection was  $30.4 \mu\text{m}$  and pull-in voltage was  $7.8 \text{ V}$ . This is a lower value for the voltage than the authors report in the abstract ( $12 \text{ V} - 45.3 \text{ V}$ ). Right before §3.2, the authors disclose the length and width of the beam as  $475 \mu\text{m}$  long and  $90 \mu\text{m}$  wide. The force of the cantilever was calculated using the beam geometries and material properties provided by the authors in the analytic model presented here. Hence the tip force was calculated the same way it was for the Si/SiO<sub>2</sub> zipper actuators.

**Device #8 and #9:** The authors report the dimensions of both these devices in Fig. 3. Device #8 is the hinged rectangle (e) and device #9 is the continuous square (d). Their deflection and voltage values are found in various places throughout the paper, and again in Table I towards the end of the paper. There is no mention of the blocking force, but they are explicit about the thicknesses of each layer (either  $0.1$  or  $0.2 \mu\text{m}$  of hard gold, and  $2.3 \mu\text{m}$  of soft gold), and the stress caused by the different gold thicknesses can be found in Part I of their study. Therefore, the blocking forces could be calculated using the analytic model in this paper as well.

**Device #10:** The deflection ( $306 \mu\text{m}$ ) and pull-in voltage ( $17 \text{ V}$ ) are stated explicitly. As are all the beam dimensions, thicknesses, and stresses. As such blocking force was calculated using the analytic model.

**Scaling:** The raw EPPA values were normalized by the EPPA of device #10, even though both device #8 and #9 had lower EPPA scores. This was because the dimensions of #8 and #9 do not truly fall within the definition of neither a cantilever beam, nor an Eulerian beam. In order to be sure that the benchmark is robust, the

EPPA scores were normalized by the lowest performing actuator whose geometry was that of a beam, or close to it, and that was device #10.

The same methodology was applied in determining EPPA scores for the out-of-plane actuators as well. The only difference was the inclusion of switching time in the calculation. This was important because it gave weight to the nature of the actuation mechanics, and its effects on performance. Thermal actuators are, by nature, slower to react than others, and as such, are less productive. Adding switching time in the calculation accounts for this.

**TFMG:** The authors report a packing density of  $1\text{mm}^2$ , which is exactly what is defined by the area – the area occupied by actuator. Table III towards the end summarizes their work and reports deflection ( $200\ \mu\text{m}$ ), force ( $0.83\ \text{mN}$ ), and voltage ( $81\ \text{V}$ ). In section C, the authors report that the first mode of vibration occurred at  $1.32\ \text{kHz}$ , which corresponds to a switching time of  $0.76\ \text{ms}$ .

**Electrothermal [5]:** Though the authors later report an actuator with greater deflection [6], the focus of that paper is not necessarily the actuator performance, and as such, it did not have enough information to be included in the comparison. In [5], though, the authors report deflection ( $0.62\ \text{mm}$ ), actuation voltage ( $5.3\ \text{V}$ ) and thermal response time ( $25\ \text{ms}$ ) in the abstract. In section 4.1 the authors divulge that their device has a “ $2.5\ \text{mm}$ ” device footprint. The center stage of the actuator is  $0.8\ \text{mm} \times 0.8\ \text{mm}$ . Therefore “ $2.5\ \text{mm}$ ” cannot refer to the area of the footprint, but rather the side length of the footprint of the actuator. The authors do not make mention of the output force, and the design is not congruent with the model presented here. In the

study of microactuators presented in [1], 0.05 mN is the center of the force range of reported electrothermal actuators.

**Comb-Drive:** The abstract reports the deflection (55  $\mu\text{m}$ ) and peak voltage (7 V). The authors have a second publication reporting the same device [35] that reports a resonant frequency of 400 Hz, for a switching time of 2.5 ms. No mention is made in either publication with regard to output force. Like the electrothermal actuator, the force was determined from the range provided in [1] for electrostatic actuators.

## Appendix C: Gallery of Spiral Geometries and other Images

Though the microstage presented in the text was ultimately the chosen geometry for achieving large deflections, many other geometries were modeled before settling on the microstage. Moreover, once the microstage had been conceived, there were some clever and interesting variations of the geometry that were modeled and fabricated. Though they don't add much with regard to the end goal of this work, they are fundamentally attached to this research. I intend this appendix to be somewhat of a "graveyard gallery" where discarded models and concepts can be displayed. Though they did not serve our purpose, perhaps others will find a use for them.

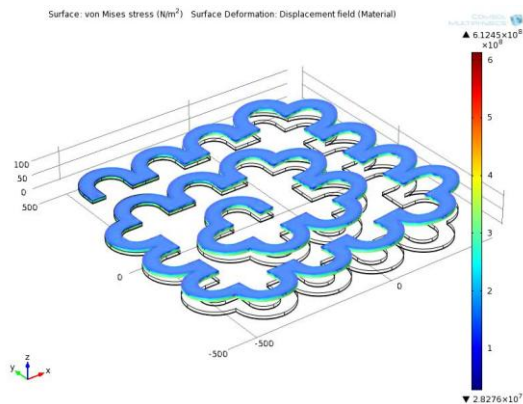


Figure 45: The "Humped Spiral"

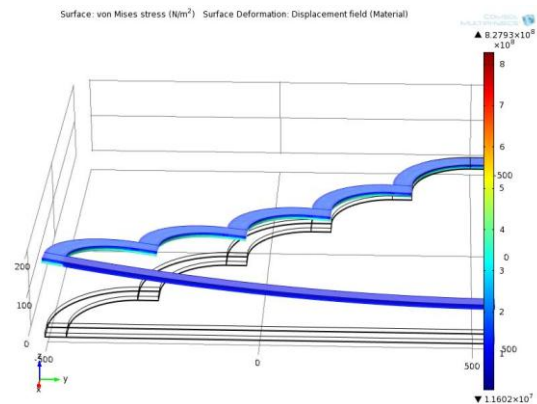


Figure 46: The "Quarter Zig-Zag"

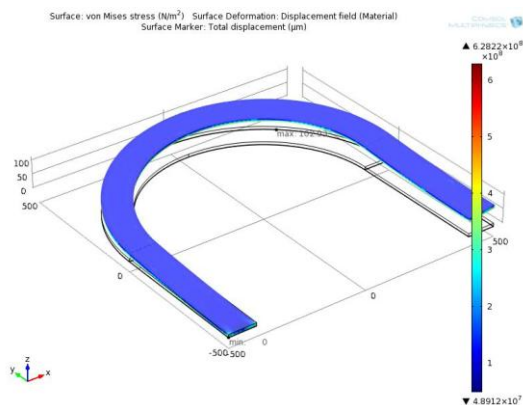


Figure 47: The "Horseshoe"

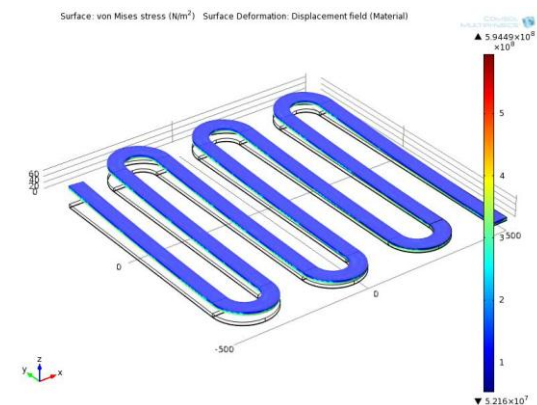


Figure 48: The "Serpentine"

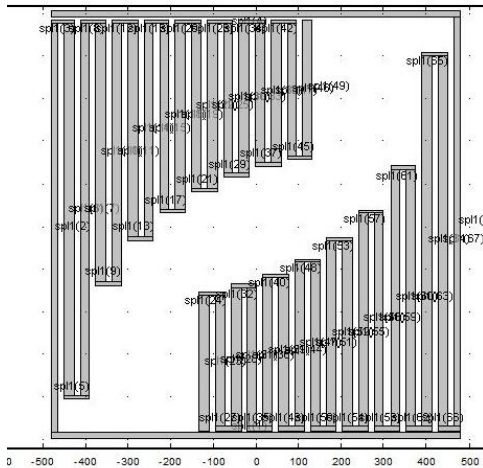


Figure 49: The "Stepper" geometry

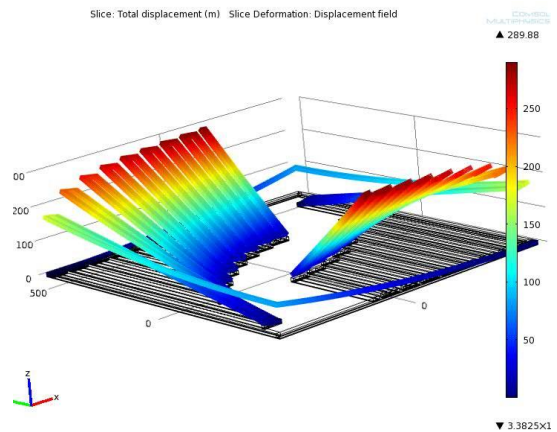
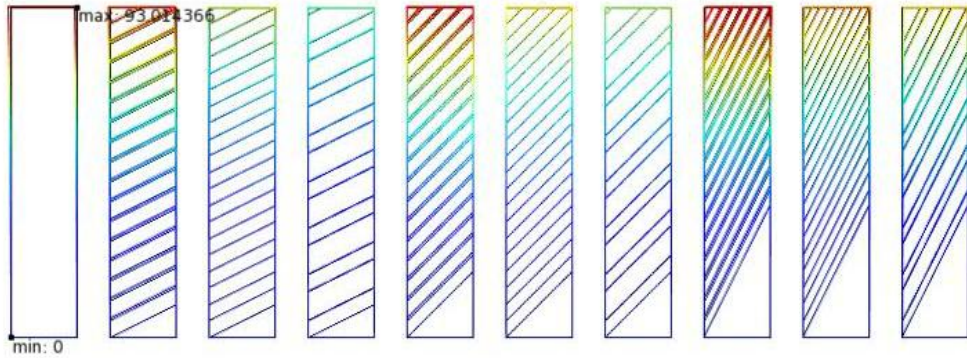


Figure 50: The "Stepper"

The Stepper was the precursor to the microstage. In this geometry, alternating legs were either plain silicon or silicon and oxide bimorph. With each turn in the serpentine, the angle at which the next beam sloped skyward became amplified. Although this would be highly impractical in terms of true vertical actuation, it jumpstarted the idea that the oxide or silicon, for that matter, could be patterned selectively.

The immediate result was an attempt to mimic the TFMG actuators presented in §3.1.1 by engineering a torque into the spiral beam so that it would warp and continue to rise rather than return to the ground, as was the case with the original spiral design. The bending effects of residual stress are amplified along the greatest dimension of the oxide. By patterning angled strips of oxide under the silicon, a warp of the beam could be engineered. Different angles and strip widths, as shown below, were attempted. Though beam warping was visible, it was not sufficient to ameliorate the issue with spiral zipper actuators.



**Figure 51: Attempt to warp the beams by patterning the oxide on a an angle.**

Patterning the silicon to be narrower than the oxide was a concept also explored. A bimorph in which the silicon is narrower than the oxide could achieve greater deflections that a bimorph whose layers had the same width. Square spirals had already been demonstrated the same ailment as true spirals. However, if greater deflections could be achieved by patterning the silicon, and the tips of the square spirals could be constrained at the center, perhaps the combination would result in large deflections.

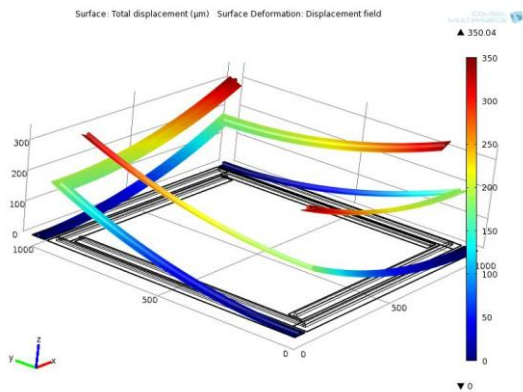


**Figure 52: Narrower silicon than oxide resulted in greater deflections.**

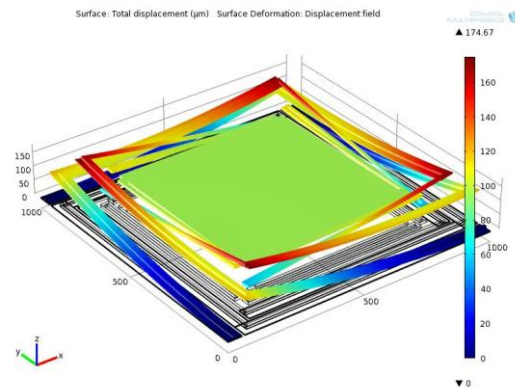


**Figure 53: Narrower silicon than oxide coupled with constrained center tips yielded almost 200 µm of deflection.**

After months of modeling ever more clever geometries, the microstage was born, and the rest of these models were relegated to the junkyard.



## References

- [1] D. J. Bell, T. J. Lu, N. a Fleck, and S. M. Spearing, “MEMS actuators and sensors: observations on their performance and selection for purpose,” *Journal of Micromechanics and Microengineering*, vol. 15, no. 7, pp. S153–S164, Jul. 2005.
- [2] W. Piyawattanametha, H. Toshiyoshi, J. LaCosse, and M. C. Wu, “Surface-Micromachined Confocal Scanning Optical Microscope,” *Tech. Digest: Conference on Lasers and Electro-Optics, 2000. (CLEO 2000).*, pp. 447–448, 2000.
- [3] J. Felder, D. L. DeVoe, E. Lee, and E. Walton, “Software-defined microstrip antennas enabled through large vertical displacement zipper microactuators,” in *2012 Microsystems for Measurement and Instrumentation (MAMNA)*, 2012, pp. 1–4.
- [4] J. Ruvinsky, “Haptic technology simulates the sense of touch -- via computer Tactile interface lets surgeons make ‘incisions’; computer gamers feel their golf drives,” *Stanford Report*, 02-Apr-2003.
- [5] L. Wu and H. Xie, “A large vertical displacement electrothermal bimorph microactuator with very small lateral shift,” *Sensors and Actuators A: Physical*, vol. 145–146, pp. 371–379, Jul. 2008.
- [6] L. Wu and H. Xie, “A Tunable Microlens with 0 . 9 mm Scan Range and Small Lateral Shift,” in *2009 IEEE/LEOS International Conference on Optical MEMS and Nanophotonics*, 2009, no. c, pp. 69–70.
- [7] A. Jain, H. Qu, S. Todd, and G. K. Fedder, “Electrothermal SCS Micromirror with Large-Vertical-Displacement Actuation,” *Computer Engineering*, pp. 228–231, 2004.
- [8] R. Legtenberg, a W. Groeneveld, and M. Elwenspoek, “Comb-drive actuators for large displacements,” *Journal of Micromechanics and Microengineering*, vol. 6, no. 3, pp. 320–329, Sep. 1996.
- [9] S. Kwon, V. Milanovic, and L. P. Lee, “Vertical Microlens Scanner for 3D Imaging,” in *Technical Digest of the 2002 Solid-State Sensor and Actuator Workshop*, 2002, pp. 3–6.
- [10] A. P. Lee, C. F. Mcconaghy, and E. W., “Electrostatic Comb Drive for Vertical Actuation,” in *Micromachining and Microfabrication Conference*, 1997, p. 14.

- [11] J. C. Chiou and Y. J. Lin, "A novel large displacement electrostatic actuator: pre-stress comb-drive actuator," *Journal of Micromechanics and Microengineering*, vol. 15, no. 9, pp. 1641–1648, Sep. 2005.
- [12] A. Selvakumar and K. Najafi, "Vertical comb array microactuators," *Journal of Microelectromechanical Systems*, vol. 12, no. 4, pp. 440–449, Aug. 2003.
- [13] C. Chang, C.-F. Chiang, C.-H. Liu, and C.-H. Liu, "A lobster-sniffing-inspired method for micro-objects manipulation using electrostatic micro-actuators," *Journal of Micromechanics and Microengineering*, vol. 15, no. 4, pp. 812–821, Apr. 2005.
- [14] N. Dhaubanjari, "The Design and Analysis of Optical Scanners for Optical Coherence Tomography," The University of Texas at Arlington, 2006.
- [15] A. K. Chinthakindi and P. A. Kohl, "Electrostatic Actuators with Intrinsic Stress Gradient: II. Performance and Modeling," *Journal of The Electrochemical Society*, vol. 149, no. 8, p. H146, 2002.
- [16] N. Dhaubanjari, S. M. N. Rao, Y. Cai, D. Popa, M. Chiao, and J.-C. Chiao, "A cantilever-type electrostatic zipping actuator," *Proceedings of SPIE*, vol. 6414, p. 641421, 2006.
- [17] M. A. Rosa, D. De Bruyker, A. R. Völkel, E. Peeters, and J. Dunec, "A novel external electrode configuration for the electrostatic actuation of MEMS based devices," *Journal of Micromechanics and Microengineering*, vol. 14, no. 4, pp. 446–451, Apr. 2004.
- [18] M. P. Brenner, J. H. Lang, J. Li, and A. H. Slocum, "Optimum Design of an Electrostatic Zipper Actuator," vol. 2, no. 1, pp. 371–374, 2004.
- [19] J. Li, "Electrostatic Zipping Actuators and Their Application to MEMS Background : Electrostatic Actuators," Massachusetts Institute of Technology, 2004.
- [20] R. Legtenberg, J. Gilbert, S. D. Senturia, and M. Elwenspoek, "Electrostatic curved electrode actuators," *Journal of Microelectromechanical Systems*, vol. 6, no. 3, pp. 257–265, 1997.
- [21] H. Sasaki, M. Shikida, and K. Sato, "A novel type of mechanical power transmission array for switching densely-arrayed actuator systems," in *19th IEEE International Conference on Micro Electro Mechanical Systems, 2006*, 2006, vol. 1, no. January, pp. 790–793.

- [22] S. M. N. Rao, P. Pandojirao-Sunkojirao, N. Dhaubanjari, M. Chiao, and J.-C. Chiao, "An optical scanner based on cantilever-type electrostatic zipping actuators," *Proceedings of SPIE*, vol. 6836, pp. 683617–683617–8, 2007.
- [23] T. Fukushige, S. Hata, and A. Shimokohbe, "A MEMS Conical Spring Actuator Array," *Journal of Microelectromechanical Systems*, vol. 14, no. 2, pp. 243–253, 2005.
- [24] S. Nata and J. Sakhrari, "Thin Film Metallic Glasses as New MEMS Materials," in *18th IEEE International Conference on Micro Electro Mechanical Systems, 2005.*, 2005, pp. 479–482.
- [25] Y. L. Iu, S. H. Ata, K. W. Ada, and A. S. Himokohbe, "Thermal, Mechanical and Electrical Properties of Pd-Based Thin-Film Metallic Glass," *Applied Physics*, vol. 40, no. 9, pp. 5382–5388, 2001.
- [26] Z. Qiu, J. S. Pulskamp, X. Lin, C.-H. Rhee, T. Wang, R. G. Polcawich, and K. Oldham, "Large displacement vertical translational actuator based on piezoelectric thin films," *Journal of Micromechanics and Microengineering*, vol. 20, no. 7, p. 075016, Jul. 2010.
- [27] R. Ghodssi and P. Lin, *MEMS Materials and Processes Handbook*. Springer, 2012, p. 1187.
- [28] D. L. DeVoe and a. P. Pisano, "Modeling and optimal design of piezoelectric cantilever microactuators," *Journal of Microelectromechanical Systems*, vol. 6, no. 3, pp. 266–270, 1997.
- [29] J. M. Gere and S. Timoshenko, *Mechanics of Materials*, Thrd. PWS-Kent Publishing Co., 1990, p. 807.
- [30] L. Meirovitch, *Fundamentals of Vibration*. McGraw-Hill Higher Education, 2001, p. 806.
- [31] W. Zhang, G. Meng, and D. Chen, "Stability, Nonlinearity and Reliability of Electrostatically Actuated MEMS Devices," *Sensors*, vol. 7, pp. 760–796, 2007.
- [32] V. Leus and D. Elata, "Fringing Field Effect in Electrostatic Actuators," Haifa, Israel, 2004.
- [33] R. T. Chen, H. Ngyen, and M. C. Wu, "A low voltage micromachined optical switch by stress-induced bending," in *Twelfth IEEE International Conference on Micro Electro Mechanical Systems*, 1999, no. 31 0, pp. 424–428.

- [34] “Natural Frequencies for Common Systems.” University of Massachusetts Lowell, pp. 1–6.
- [35] S. Kwon, V. Milanovic, and L. P. Lee, “Large-displacement vertical microlens scanner with low driving voltage,” *IEEE Photonics Technology Letters*, vol. 14, no. 11, pp. 1572–1574, Nov. 2002.